Fakultät für Maschinenwesen
Lehrstuhl für Aerodynamik und Strömungsmechanik

Large-Eddy Simulation of Turbulent Cavitating Flows

Christian Peter Egerer

Vollständiger Abdruck der von der Fakultät für Maschinenwesen der Technischen Universität München zur Erlangung des akademischen Grades eines

Doktor-Ingenieurs (Dr.-Ing.)

genehmigten Dissertation.

Vorsitzender:		Univ.-Prof. Dr.-Ing. Oskar J. Haidn
Prüfer der Dissertation:	1.	Univ.-Prof. Dr.-Ing. Nikolaus A. Adams
	2.	Prof. Dr.-Ing. Stefan Hickel, Technische Universität Delft, Niederlande

Die Dissertation wurde am 10.12.2015 bei der Technischen Universität München eingereicht und durch die Fakultät für Maschinenwesen am 09.11.2016 angenommen.

Christian Peter Egerer: *Large-Eddy Simulation of Turbulent Cavitating Flows*, Dissertation, Technische Universität München

ADDRESS:
Prälatenweg 6a, 82398 Polling, Germany

E-MAIL:
christian.egerer@tum.de

The images on the cover (print-version only) visualize the flow of a cavitating mixing layer. The top image shows instantaneous vortical structures colored by the streamwise velocity. Blue and red colors indicate slow and fast flowing fluid, respectively. The bottom image shows corresponding instantaneous vapor structures.

ABSTRACT

The process of local evaporation of liquids due to a drop in static pressure below saturation conditions and its subsequent sudden re-condensation is called *cavitation*. Caviation affects the performance of components and devices in many engineering applications, e.g., liquid fuel injection, hydrodynamic power generation, or ship propulsion. Thus, it is desirable to understand, predict and control cavitation since it can have favorable as well as detrimental consequences. On the one hand, forces resulting from the collapse of vapor structures can be used to clean surfaces. On the other hand, these forces can lead to the destruction of material surfaces (*cavitation erosion*) and ultimately can lead to the failure of components and devices.

Computational Fluid Dynamics can evolve as a design tool for engineering devices involving cavitation if all effects relevant to cavitation dynamics and cavitation erosion are included in the flow model. Previous research projects showed that it is possible to predict cavitation erosion related data by a compressible formulation of the liquid and homogeneous liquid-vapor mixture coupled to a local thermodynamic equilibrium phase change model.

The focus of the present thesis is the inclusion and evaluation of viscous effects like secondary mean flows and the mutual interaction of cavitation and resolved turbulence. The existing inviscid framework is therefore extended to Large-Eddy Simulation of turbulent cavitating flow.

In a first step, we adapt the Adaptive Local Deconvolution Method for cavitating flows and perform validation by comparing numerical and experimental data for the canonical flow of a turbulent mixing layer. The Large-Eddy Simulation results for non-cavitating and cavitating conditions, e.g., velocity statistics and vapor volume fraction data, are in good agreement with experimental data. The prediction capability of the Adaptive Local Deconvolution Method for cavitating flows is demonstrated for a generic throttle flow.

In a second step, a novel discretization scheme for Large-Eddy Simulation of turbulent cavitating flows with a smaller stencil than the Adaptive Local Deconvolution Method is developed and validated. The inviscid framework of the Computational Fluid Dynamics tool CAvitation Technische Universität München is extended by adopting established concepts from numerical methods for high-speed gasdynamic flows as well as from the Adaptive Local Deconvolution Method regarding the implicit modeling strategy of subgrid scale stresses.

ZUSAMMENFASSUNG

Der Prozess der lokalen Verdampfung einer Flüssigkeit in Folge des Abfalls des statischen Drucks unterhalb der Sättigungsbedingungen und das darauffolgende schlagartige Rekondensieren wird als *Kavitation* bezeichnet. Für viele Anwendungen im Maschinenbau, wie z.B. die Kraftstoffeinspritzung, die Wasserkraft oder Schiffsantriebe, ist es von Vorteil, den Kavitationsprozess zu verstehen, vorherzusagen und zu kontrollieren, um seine negativen als auch positiven Auswirkungen zu beherrschen. Einerseits können die aus dem Kollaps von Dampfgebieten entstehenden Kräfte zum Reinigen von Oberflächen oder zum Zerstören von Nierensteinen verwendet werden. Andererseits können diese Kräfte Materialoberflächen schädigen (*Kavitationserosion*) und zum Versagen des betroffenen Bauteils führen.

Die numerische Strömungsmechanik kann zu einem Auslegungswerkzeug für Bauteile werden, falls alle Effekte, die für die Kavitationsdynamik und -erosion von Bedeutung sind, im strömungsmechanischen Modell berücksichtigt sind. Vorangegange Forschungsvorhaben zeigten, dass es möglich ist, Kavitationserosion mit Hilfe einer kompressiblen Beschreibung der Flüssigkeit und des homogenen Dampf-Flüssigkeitsgemisches in Verbindung mit einem Gleichgewichtsphasenmodell vorherzusagen.

Der Schwerpunkt der vorliegenden Arbeit ist die Einbeziehung und Beurteilung von Reibungseinflüssen wie Sekundärströmungen und die gegenseitige Beeinflussung von Kavitation und aufgelöster Turbulenz. Die bisher reibungsfreie Behandlung wird deshalb um die Grobstruktursimulation von turbulenten kavitierenden Strömungen erweitert.

Im ersten Schritt wird die Adaptive Local Deconvolution Method für die Berechnung von kavitierenden Strömungen angepasst und anhand der kanonischen Strömung einer turbulenten Mischungsschicht validiert. Die Ergbenisse für nicht-kavitierende und kavitierende Bedingungen, z.B. Geschwindigkeitsstatistiken und Dampfvolumenwerte, zeigen gute Übereinstimmung mit experimentellen Daten. Die Vorhersageeigenschaften der Adaptive Local Deconvolution Method wird anhand einer generischen Drosselströmung gezeigt.

In einem zweiten Schritt wird ein neues Diskretisierungsschema, das für die Grobstruktursimulation von turbulenten kavitierenden Strömungen geeignet ist, mit einem kleineren Diskretisierungsstern als die Adaptive Local Deconvolution Method entwickelt. Die reibungsfreie Umgebung CAvitation Technische Universität München dient dabei als Grundlage und wird erweitert, indem bewährte Konzepte von numerischen Methoden für Überschallströmungen und von der impliziten Modellierung von Feinstrukturspannungen der Adaptive Local Deconvolution Method übernommen werden.

PUBLICATIONS

Ideas and results of the following publications by the author are included in parts or in an extended version in this thesis:

[27] C. P. Egerer, S. Hickel, S. J. Schmidt and N. A. Adams (2012). Implicit large-eddy simulation of cavitation in a turbulent shear layer. In: *Proceedings of the 8th International Symposium on Cavitation (CAV 2012).* Editors: C.-D. Ohl, E. Klaseboer, S. W. Ohl, S. W. Gong and B. C. Khoo. Singapore, Research Publishing Services. ISBN: 978-981-07-2826-7.

[28] C. P. Egerer, S. Hickel, S. J. Schmidt and N. A. Adams (2012). Turbulence modulation by phase change in a cavitating shear layer. In: *Proceedings of the 9th International ERCOFTAC Symposium on Engineering Turbulence Modelling and Measurements (ETMM9).* Thessaloniki, Greece.

[29] C. P. Egerer, S. Hickel, S. J. Schmidt and N. A. Adams (2014). Large-eddy simulation of turbulent cavitating flow in a micro channel. *Physics of Fluids* 26(8): 085102.

[30] C. P. Egerer, S. J. Schmidt, S. Hickel and N. A. Adams (2016). Efficient implicit LES method for the simulation of turbulent cavitating flows. *Journal of Computational Physics* 316: 453-469.

Furthermore, the author contributed to the following publication while being a Research Assistent at the Institute of Aerodynamics and Fluid Mechanics but the content is not covered in this thesis:

[47] S. Hickel, C. P. Egerer and J. Larsson (2014). Subgrid-scale modeling for implicit large eddy simulation of compressible flows and shock-turbulence interaction. *Physics of Fluids* 26(10): 106101.

Our greatest weakness lies in giving up. The most certain way to succeed is always to try just one more time.

— Thomas A. Edison

ACKNOWLEDGEMENTS

Completing doctoral studies is impossible without support and motivation – both from a professional as well as an emotional point of view.

First and foremost, I would like to thank Prof. Nikolaus Adams for creating a research environment with guidance and support but also as much freedom as possible to pursue one's own ideas. I am also thankfull to Prof. Adams for encouraging me to publish my research work.

Many thanks to Prof. Stefan Hickel, who already supported me throughout my aerospace sciences studies and diploma thesis. Stefan also introduced me to programming and excited my passion for it.

Prof. Haidn accepted the position of chairman for my doctoral examination board and handled all the administrative tasks for which I am thankful.

Thanks to all my former colleagues, who made the daily life as a PhD student a lot more pleasant. In particular, thanks to Steffen, Marcus, Hatsch and Freddy for many interesting discussions – on and off topic – at the institute or in the evenings at Italian or Greek restaurants. Many other enjoyable evenings were spent with Anja, Mark, Matze and Stefan playing beach-volleyball, where I could get my mind off from research and through whom I got to know Margit.

Thank you Margit for not giving up on me, for motivating me while writing up my thesis and for your unconditional love. Sina oled kõige parem, mis minuga juhtunud on!

Last but not least, I am deeply grateful to my family. My parents Irmgard and Peter have always supported me in every aspect of my academic education. They were always there with advice and comforting words when I needed them.

This work was financially supported by the German Research Foundation (Deutsche Forschungsgemeinschaft) under grant AD186/20-1. Computational resources were provided by the Leibniz Supercomputing Centre (LRZ) and the High Performance Computing Centre Stuttgart (HLRS).

CONTENTS

LIST OF FIGURES

LIST OF TABLES

ACRONYMS

1-D	one-dimensional
2-D	two-dimensional
3-D	three-dimensional
ALDM	Adaptive Local Deconvolution Method
CATUM	CAvitation Technische Universität München

CFD	Computational Fluid Dynamics
CFL	Courant-Friedrichs-Lewy
DIS	Diesel Injection System
DNS	Direct Numerical Simulation
EDQNM	Eddy-Damped Quasi-Normal Markovian
EOS	Equation of State
FFT	Fast Fourier Transform
HLLC	Harten-Lax-van Leer-Contact
IAPWS	International Association for the Properties of Water and Steam
JST	Jameson-Schmidt-Turkel
LES	Large-Eddy Simulation
MILES	Monotonically Integrated Large Eddy Simulation
MUSCL	Monotonic Upstream-Centered Scheme for Conservation Laws
PIV	Particle Image Velocimetry
PSD	Power Spectral Density
PREVERO	Experimental and CFD technology for PREVentive reduction of Diesel engine emissions caused by cavitation EROsion
RANS	Reynolds Averaged Navier-Stokes
RK3S3	third-order 3-stage Runge-Kutta method
RK2S4	second-order low-storage 4-stage Runge-Kutta method
SGS	subgrid scale
TKE	Turbulence Kinetic Energy
TVD	Total Variation Diminishing
VOF	Volume-of-Fluid
WENO5	fifth-order Weighted Essentially Non-Oscillatory

1 INTRODUCTION

1.1 BACKGROUND

Cavitation plays an important role in many engineering applications, e.g., liquid fuel injection, hydrodynamic power generation, or ship propulsion. But also medical treatments utilize cavitation, e.g., for removing kidney stones by extracorporeal shock wave lithotripsy. For predicting cavitation dynamics in these kind of applications wave and turbulence dynamics need to be incorporated into numerical solution strategies: on the one hand, shock waves are emitted during sudden re-condensation (collapse) of vapor structures and propagate subsequently through the liquid and liquid-vapor mixture; on the other hand, cavitation and turbulence dynamics can occur on the same range of time and length scales. Thus, numerical methods capable of capturing discontinuities in the flow field and simultaneously being able to resolve broad-band turbulence are required.

The investigations in the present work are related to liquid fuel injection systems. Modern direct Diesel Injection Systems (DISs) exceed injection pressures of 2000 bar in order to meet current and future emission standards set by legislators. For higher injection pressures the primary break-up of a liquid jet is enhanced and thus mixing of fuel and air is faster which in turn increases combustion efficiency. Since typical compression ratios in the combustion chamber are between 15:1 and 22:1, higher injection pressures generally lead to larger pressure differences across injection nozzles and throttle valves. The static pressure in the liquid fuel decreases when the liquid is accelerated within an injection nozzle or throttle valve. When the static pressure in the liquid fuel drops below vapor pressure, evaporation can occur. Even for conditions where the mean static pressure is above vapor pressure, cavitation can still occur due to low pressures in vortex cores, such as corner vortices in channels or turbulent eddies, see the review on vortex cavitation by Arndt [11] for details.

Closing of valves or the advection of a vapor cavity in regions where the static pressure of the surrounding liquid is above the vapor pressure results in the sudden re-condensation or collapse of vapor cavities accompanied by a high acceleration of the surrounding liquid towards the center of the cavities and the formation of strong shock waves [17]. The vigorous collapse of vapor cavities can be beneficial or detrimental. Cavitation, e.g., cleans the injection nozzle from deposits thus preventing performance degradations of the injection system. Since the early experimental work by Reitz and Bracco [82] it is known that cavitation promotes the primary break-up during the atomization process of a liquid jet. While cavitation can have a favorable effect in injection nozzles, it can damage material sur-

faces (*cavitation erosion*) of injection and control valves, eventually leading even to the failure of components [12]. For efficient, reliable and safe operation an accurate prediction of the flow and cavitation dynamics during the design process of modern DISs is a prerequisite.

Early experimental investigations of cavitation in DISs date back to the study by Bergwerk [15], who examined geometric as well as hydrodynamic effects on the cavitating flow in spray holes. More recently, the introduction of X-ray attenuation measurements [107] allows a quantitative evaluation of the vapor content in a cavitating flow. Other experimental techniques include high-speed motion pictures, laser-pulsed light transmission measurements, interferometry, and schlieren imaging [51, 70]. Thereby, it is possible to visualize the instantaneous location of cavitation structures and shock waves due to vapor bubble or cloud collapses and to reconstruct two-dimensional (2-D) density fields. Nevertheless, the extraction of quantitative data for often highly unsteady and three-dimensional (3-D) flow fields from experiments is difficult. Since typical dimensions of real-size geometries are on the order of 10^{-3} m and less standard experimental techniques are not applicable. Many experimental studies thus use enlarged geometries [36].

Consequently, advanced numerical simulation approaches, such as well-resolved Large-Eddy Simulation (LES), where time-dependent 3-D data of the flow field is readily available, can contribute to the understanding of the internal flow in real-size DISs. Ideally, underlying flow dynamics can be identified and controlled in order to design engineering devices free of cavitation erosion issues.

Many numerical studies [9, 39, 41] did not resolve turbulence but employed turbulence models based on Reynolds- or Favre-averaging of the Navier-Stokes equations (RANS). An experimental and RANS study for micro channels was performed by Medrano et al. [71, 72], for example.

Since cavitation and turbulence dynamics can occur on similar time and length scales, the resolution of the most energetic turbulent motion is necessary for accurate numerical predictions. The feasibility of incompressible LES, employing a homogeneous mixture model with finite-rate mass transfer between liquid and vapor and an implicit treatment of subgrid scale (SGS) stresses, has been demonstrated for ship propeller applications by Bensow and Bark [14]. Incompressible LES of the liquid phase, coupled to a Lagrangian bubbly-flow model, employing a dynamic Smagorinsky model have been performed by Shams [99] to study cavitation inception over a cavity. A homogeneous mixture model was also used by Duke et al. [24] and Salvador et al. [88] to perform incompressible LES of generic or real geometries of injection systems. Compressible LES of turbulent cavitating flow in a Venturi nozzle, employing a homogeneous mixture model with an additional transport equation for the vapor mass fraction, was performed by Dittakavi et al. [21]. SGS stresses were approximated by the dynamic Smagorinsky model. The speed of sound of liquid water was, however, artificially decreased in order to reduce the stiffness of the

system of equations thus altering the wave dynamics of the system. Sou et al. [104] perfomed incompressible LES coupled with a one-way bubble tracking method and Rayleigh-Plesset bubble dynamics to reproduce the experimentally investigated flow through a rectangular nozzle and the subsequent liquid jet break-up [105]. Lu et al. [69] use incompressible LES and a Volume-of-Fluid (VOF) approach to predict the cavitating flow on a ship propeller.

The aforementioned numerical methods allow for the prediction of steady and unsteady flow characteristics on the time scale of the convective velocity, but do not incorporate wave-dynamics effects. Pressure loads originating from collapse-induced shock waves are, however, essential for predicting cavitation erosion. The good prediction capabilities of hydrodynamic and wave dynamic effects were demonstrated by density-based, low-Mach-number-consistent numerical methods with explicit time-stepping, solving the inviscid Euler equations coupled with a thermodynamic equilibrium cavitation model [97].

1.2 SCOPE OF THIS THESIS

Since the resolution of all time and length-scales of turbulence and cavitation is not feasable with today's computational resources, it is unavoidable to resort to reduced order models like compressible LES for the numerical simulation of realistic flow devices. Thus, we adopt the two-phase modeling and numerical solution strategy for the time-resolved simulation of hydrodynamics and wave dynamics by Schnerr et al. [97], extended by an SGS model for turbulence, for the simulation of turbulent cavitating flow. In compressible LES of cavitating flows, numerical schemes must be robust against local underresolution. Yet the prediction of turbulent motions requires that the proper SGS energy transfer is provided by the LES method.

The Adaptive Local Deconvolution Method (ALDM) [46, 47] provides a physically motivated, solution-adaptive implicit treatment of SGS stresses. Applying ALDM to cavitating flows requires changes [29, 48] in order to address both issues (numerical robustness and proper SGS energy transfer). Thus, one major goal of this thesis is

- ❏ the validation of ALDM adapted for cavitating flows [29, 48], and
- ❏ the application of ALDM to a generic, yet application-relevant, flow device [29] in order to establish ALDM as a reference Computational Fluid Dynamics (CFD) tool for compressible LES of cavitating flows in the design phase of engineering devices.

The second major goal of this thesis is the extension of the CFD tool CAvitation Technische Universität München (CATUM) [97] for compressible LES of cavitating flows. CATUM was designed as a CFD tool focusing on inertia-driven and compressiblity effects in cavitating flows. For studying such effects it

was shown that an inviscid framework is sufficient [4, 92–95, 97]. Yet, especially in wall-bounded flows, secondary mean flow or turbulence can alter cavitation dynamics or vice versa. By adopting concepts from numerical methods designed for high-speed gasdynamic flows and from physically consistent implicit LES, this thesis

- ❏ proposes a modification of the original reconstruction and flux function of CATUM, and
- ❏ subsequently validates the novel discretization scheme for turbulent cavitating flows.

1.3 OUTLINE

The first part of this thesis briefly introduces cavitation, see Chapter 2, and numerical modeling methodologies for cavitating flows, see Chapter 3.

The second part summarizes ALDM adapted for cavitating flows, see Chapter 4, and validates ALDM by comparing numerical and experimental results of the canonical problem of a turbulent cavitating mixing layer, see Chapter 5. Afterwards, ALDM is applied to predict the turbulent cavitating flow in a generic throttle, see Chapter 6.

The extension of CATUM for compressible LES, see Chapter 7, is covered in the third part of this thesis. Validation of the novel discretizatin scheme and its application to cavitating flows is presented in Chapters 8 and 9, respectively.

Overall conclusions and an outlook will be given in Chapters 10 to 12.

Part 1

SOME FUNDAMENTALS

2 INTRODUCTION TO CAVITATION

This chapter briefly summarizes essential aspects of cavitation without claiming to be comprehensive. For a more detailed introduction on the physics of cavitation the interested reader is refered to the textbooks by Brennen [17] and Franc & Michel [33], or the review paper by Plesset & Prosperetti [80].

The term *cavitation* is associated with a locally confined sudden evaporation if the static pressure in a resting or moving and initially homogeneous liquid drops below a certain pressure threshold. The drop in static pressure can either be caused by a local flow acceleration (*hydrodynamic cavitation*) or, for example, by applying an acoustic field where cavitation can occur at pressure minima of sound waves (*acoustic cavitation*).

Cavitation can be descriminated from boiling by looking at a phase diagram for a one-component fluid, see Fig. 1. The vapor pressure curve $p_{sat}(T)$ separates the liquid from the vapor region and is a function of temperature T only. The boiling process is characterized by a temperature increase at constant pressure, i.e., a horizontal line as indicated in the phase diagram in Fig. 1. Cavitation is associated with the process where the static pressure decreases below vapor pressure, i.e., a vertical path in the phase diagram. The temperature of the surrounding liquid decreases slightly (thermal delay) during the evaporation process since the surrounding liquid needs to provide the latent heat of evaporation.

Note that the vapor pressure curve $p_{sat}(T)$ is only a sharp boundary between the liquid and vapor phase under the assumption of local thermodynamic euqilibrium. Non-equilibrium or meta-stable states may be observed depending on the nuclei content (for example the number and size of small air bubbles) and the time-scale of the flow. For meta-stable states the liquid may sustain even large negative pressures (tensile stresses) and *cavitation inception* is observed for $p < p_{sat}$ (*static delay*). If liquid water, for example, is free of any impurities theoretical tensile stresses on the order of 10^9 Pa are possible until *homogeneous* nucleation is possible [34]. In experiments maximum tensile stresses on the order of 10^7 Pa were observed [22]. On the other hand, if nuclei like small air bubbles, particles or rough walls are present one speaks of *heterogeneous* nucleation and cavitation occurs at $p \approx p_{sat}$. Cavitation inception is, however, a research field on its own and is not considered in this work. Instead, we assume local thermodynamic equilibrium. Thus, cavitation occurs once the static pressure decreases to the local vapor pressure p_{stat}, see Section 3.4 for details.

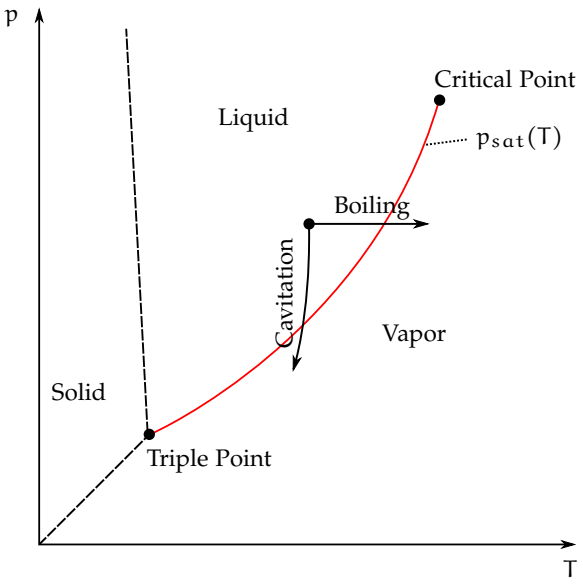

Figure 1: Phase diagram for a one-component fluid.

For cavitating flows the main non-dimensional parameter is the cavitation number

$$\sigma_c = \frac{p_{ref} - p_{sat}(T)}{\Delta p}. \tag{1}$$

It is defined by the ratio of the difference in static pressure at a reference location p_{ref} and the vapor pressure p_{sat} to a characteristic pressure difference Δp of the considered flow or device. Examples for Δp are the pressure difference across a throttle or the dynamic pressure $\Delta p_{dyn} = \rho_{ref} U_{ref}^2/2$, where ρ_{ref} and U_{ref} are reference density and reference velocity of the flow.

Numerical modeling of cavitating flows is especially challenging since many forms of cavitation exist and can occur simultaneously. Cavitation types are:

- *bubble cavitation*: cavitation is observed in the regions of low pressures as a result of the rapid growth of initially present air nuclei. The bubbles are advected by the flow until they collapse in regions of high pressure. Fluid quality, i.e., the concentration of dissolved gas, controls the size and number of vapor bubbles.
- *sheet cavities* are found on hydrofoils of, e.g., ship propellers. In many cases sheet cavities are created periodically, a re-entrant jet forms and large vapor structures detach (shedding process).
- *cloud cavities* comprise many small vapor bubbles originating from the detachment of vapor structures from sheet cavities.
- *super-cavitation* denotes the state when, e.g., the suction side of a hydrofoil is completely covered by vapor.

- *vortex cavitation* occurs in the low pressure cores of vortices. A common type of vortex cavitation is associated with the tip vortex of ship propellers. Furthermore, turbulent eddies can lead to vortex cavitation.

The cavitation process not only includes the evaporation process but also a second step where a sudden re-condensation occurs. The surrounding liquid is accelerated towards the center of vapor cavities where shock waves are emitted in the final stages of vapor bubble collapses. If a vapor bubble collapses close to a solid wall the collapse becomes asymmetric and a liquid micro-jet which is directed towards the wall is generated. Both phenomena have negative and positive effects in cavitating flows. Positive effects include surface cleaning, the removal of kidney stones (extracorporeal shock wave lithotripsy), or the enhancement of liquid jet breakup. Negative effects include degradation of performance of hydraulic machines, noise and vibrations, and cavitation erosion.

3 NUMERICAL MODELING OF CAVITATION AND TURBULENCE

For discussing some concepts in the following, it is convenient to consider an initial-value problem for a generic transport equation with non-linear flux $\mathbf{F}(\varphi)$ and body forces f_B,

$$\partial_t \varphi(\mathbf{x}, t) + \nabla \cdot \mathbf{F}(\varphi, \mathbf{x}, t) = f_B(\mathbf{x}, t), \tag{2}$$

instead of the full system describing the evolution of a fluid flow. The weak or integral form of Eq. (2) is

$$\partial_t \int_\Omega \varphi(\mathbf{x}, t) d\mathcal{V} + \int_{\partial\Omega} \mathbf{F}(\varphi, \mathbf{x}, t) \cdot d\boldsymbol{\mathcal{A}} = \int_\Omega f_B(\mathbf{x}, t) d\mathcal{V}, \tag{3}$$

and describes the evolution of a solution quantity $\varphi(\mathbf{x}, t)$ in a control volume Ω with surface $\partial\Omega$.

3.1 FINITE VOLUME METHOD

For solving the mathematical model governing the evolution of a fluid flow, we consider finite volume methods only. Spatial discretization of the computational domain leads to N disjoint grid cells i. Associating each grid cell i with a control volume Ω_i with volume

$$V_i = \int_{\Omega_i} 1 d\mathcal{V} \tag{4}$$

and surface $\partial\Omega_i$, allows us to describe the evolution of the volume-averaged solution of grid cell i,

$$\overline{\varphi}_i(t) = \frac{1}{V_i} \int_{\Omega_i} \varphi(\mathbf{x}, t) d\mathcal{V}, \tag{5}$$

by the semi-discretized form of Eq. (3)

$$\partial_t \overline{\varphi}_i(t) \approx -\frac{1}{V_i} \sum_j \left(\breve{\mathbf{F}}_j \cdot \mathbf{n}_j \right) A_j + \breve{f}_{B,i}, \tag{6}$$

where

$$\sum_j \left(\breve{\mathbf{F}}_j \cdot \mathbf{n}_j \right) A_j = \int_{\partial\Omega_i} \mathbf{F}(\varphi, \mathbf{x}, t) \cdot d\boldsymbol{\mathcal{A}} \tag{7}$$

approximates the flux across all cell faces j with unit normals $\mathbf{n}_j$ of grid cell i. $\breve{f}_{B,i}$ are the effective body forces, averaged similar to Eq. (5), acting

Table 1: Coefficients for Runge-Kutta methods.

m	RK2S4	RK3S3		
	$c_3^{(m)}$	$c_1^{(m)}$	$c_2^{(m)}$	$c_2^{(m)}$
1	0.11	1	0	1
2	0.2766	3/4	1/4	1/4
3	0.5	1/3	2/3	2/3
4	1.0	–	–	–

on cell i. Note that we already assume in Eq. (6) that the surface integral on the right-hand side of Eq. (7) is approximated by one Gauss point per cell face j only. The task of a spatial discretization scheme is to find a suitable numerical approximation $\check{F}_j$ to the physical flux $F(\varphi, \boldsymbol{x}, t)$, see Chapter 4 and Chapter 7.

For advancing the volume-averaged solution (5) from time t_n to time t_{n+1} we use explicit Runge-Kutta methods. All computations presented in the following are performed either by a second-order low-storage 4-stage Runge-Kutta method (RK2S4) with enhanced stability region [93], or by a Total Variation Diminishing (TVD) third-order 3-stage Runge-Kutta method (RK3S3) [42]. Lumping the right-hand side of Eq. (6) into the operator $\mathcal{L}_i(\overline{\varphi})$ for the spatial discretization, the low-storage RK2S4 method reads

$$\begin{aligned} \overline{\varphi}_i^{(m)} &= \overline{\varphi}_i^n + c_3^{(m)} \Delta t \mathcal{L}_i(\overline{\varphi}_i^{(m-1)}), \\ & \qquad m = 1 \ldots 4, \\ \text{with} \quad \overline{\varphi}_i^{(0)} &= \overline{\varphi}_i^n, \quad \text{and} \quad \overline{\varphi}_i^{(4)} = \overline{\varphi}_i^{n+1}. \end{aligned} \tag{8}$$

The time integration procedure for the RK3S3 method is [42]

$$\begin{aligned} \overline{\varphi}_i^{(m)} &= c_1^{(m)} \overline{\varphi}_i^n + c_2^{(m)} \overline{\varphi}_i^{(m-1)} + c_3^{(m)} \Delta t \widetilde{\mathcal{L}}_i(\overline{\varphi}_i^{(m-1)}), \\ & \qquad m = 1 \ldots 3, \\ \text{with} \quad \overline{\varphi}_i^{(0)} &= \overline{\varphi}_i^n, \quad \text{and} \quad \overline{\varphi}_i^{(3)} = \overline{\varphi}_i^{n+1}. \end{aligned} \tag{9}$$

For each grid cell i we can define a local timestep Δt_i subject to the Courant-Friedrichs-Lewy (CFL) criterium [18]

$$\Delta t_i \leq \mathrm{CFL} \frac{\Delta x_i}{|u_i \pm c_i|}, \tag{10}$$

where Δx_i is a characteristic lenght, u_i is a characteristic velocity, and c_i is the speed of sound. For a stable and time accurate advancement of the solution the global time step size is $\Delta t = \min(\Delta t_i)$. Coefficients for the Runge-Kutta methods are provided in Table 1.

3.2 TWO-PHASE MODELS

Considering again a control volume Ω, each phase $k = l, v$ (l = liquid, v = vapor) of a one-component flow with phase-change can be identified by a phase indicator function $\chi_k(\mathbf{x}, t)$, which is unity if phase k is present at location $\mathbf{x}$ at time t, and is zero otherwise. Thus, we can define a volume average

$$\overline{\varphi}_k = \frac{1}{V} \int_\Omega \varphi_k \chi_k(\mathbf{x}, t) d\mathcal{V}, \tag{11}$$

and a density-weighted, or Favre, average

$$\widetilde{\varphi}_k = \frac{\overline{\rho_k \varphi_k}}{\overline{\rho}_k} = \frac{\int_\Omega \rho_k \varphi_k \chi_k(\mathbf{x}, t) d\mathcal{V}}{\int_\Omega \rho_k \chi_k(\mathbf{x}, t) d\mathcal{V}}, \tag{12}$$

of quantity φ_k of phase k. Setting $\varphi_k \equiv 1$, we obtain the volume fraction of phase k

$$\alpha_k = \frac{1}{V} \int_V \chi_k(\mathbf{x}, t) d\mathcal{V}, \tag{13}$$

with properties $0 \leq \alpha_k \leq 1$, $\sum_k \alpha_k = 1$. A phase-weighted average $\widehat{\varphi}_k$ is thus defined as

$$\alpha_k \widehat{\varphi}_k = \overline{\varphi}_k. \tag{14}$$

Modeling turbulent cavitating flows is challenging due to spatial and temporal scales covering several orders of magnitude, e.g., length scales ranging from cavitation nuclei with radii in the micrometer range to sheet cavities with millimeter or larger extents. If we again associate the control volume Ω with a cell i of the computational grid as in the previous Section 3.1, the volume average in Eq. (11) introduces a length scale l_{num} that is characteristic for the underlying computational grid, e.g., $l_{num} = V_i^{1/3}$. Turbulence and phase interfaces introduce another characteristic length scale l_{phys}. The ratio $\psi = l_{phys}/l_{num}$, allows for classification of different modeling approaches [4].

3.2.1 *Two-Fluid Model*

The two-fluid model is the most general way to describe a two-phase flow subject to the continuum hypothesis. Each phase k is governed by an individual set of transport equations for mass, momentum and total energy, weighted by the respective volume fraction α_k

$$\partial_t(\alpha_k \widehat{\rho}_k) + \nabla \cdot (\alpha_k \widehat{\rho_k \mathbf{u}_k}) = \widehat{\Gamma}_k^\rho, \tag{15a}$$

$$\partial_t(\alpha_k \widehat{\rho_k \mathbf{u}_k}) + \nabla \cdot (\alpha_k \rho_k \widehat{\mathbf{u}_k \mathbf{u}}_k + \widehat{p}_k \mathbf{I} - \widehat{\boldsymbol{\tau}}_k) = \widehat{\boldsymbol{\Gamma}}_k^{\rho u}, \tag{15b}$$

$$\partial_t(\alpha_k \widehat{\rho_k E_k}) + \nabla \cdot [\alpha_k (\widehat{\rho_k E_k \mathbf{u}}_k + \widehat{p_k \mathbf{u}_k} - \widehat{\boldsymbol{\tau}_k \cdot \mathbf{u}_k} + \widehat{\mathbf{q}}_k)] = \widehat{\Gamma}_k^{\rho E}. \tag{15c}$$

Density ρ_k, momentum $\rho_k \mathbf{u}_k$, and total energy $\rho_k E_k = \rho_k(e_k + \mathbf{u}_k^2/2)$ comprise the conservative variables, where $\mathbf{u}_k$, p_k and e_k denote velocity, pressure and specific internal energy, respectively. $\mathbf{I}$ is the identity tensor, and $\boldsymbol{\tau}_k = \mu_k[\nabla \mathbf{u}_k + (\nabla \mathbf{u}_k)^T - 2(\nabla \cdot \mathbf{u}_k)/3]$ is the viscous stress tensor of a Newtonian fluid, where μ_k is the dynamic viscosity. Heat conduction is modeled by Fourier's law, $\mathbf{q}_k = -\lambda_k \nabla T_k$, where λ_k is the thermal conductivity, and T_k is the temperature. The individual transport equations (15) for the two phases are coupled at the liquid-vapor phase interface by exchange terms $\widehat{\Gamma}_k^{\rho}$, $\widehat{\boldsymbol{\Gamma}}_k^{\rho u}$, and $\widehat{\Gamma}_k^{\rho E}$ for mass, momentum and energy, respectively. The Dirac function δ_{lv} defining the liquid-vapor phase interface can be utilized to define the volume-averaged exchange terms

$$\widehat{\Gamma}_k^{\rho\varphi} = \frac{1}{V_i} \int_{\Omega_i} \Gamma_k^{\rho\varphi} \delta_{lv} \mathrm{d}\mathcal{V}, \quad \varphi = [1, u_k, E_k]. \tag{16}$$

Eq. (15) is closed by suitable equations of state for each phase k

$$\widehat{e}_k = \widehat{e}_k(\widehat{s}_k, \widehat{\rho}_k), \tag{17}$$

where $\widehat{s}_k$ is the entropy of phase k. For a complete mathematical description of the thermo-fluid dynamics of two-phase flows, we refer the reader, e.g., to the textbook of Ishii & Hibiki [52].

If we can ensure that $\psi \gg 1$ based on a characteristic scale of phase interfaces, e.g., a bubble radius, and that $\psi = \mathcal{O}(1)$ for the smallest turbulent scales, where l_{phys} is set equal to the Kolmogorov scale, Direct Numerical Simulation (DNS) of phase interfaces and turbulent flow is possible. In this case, details of mass, momentum and energy transfer between both phases, including thermal, mechanical, and phase non-equilibrium effects, are represented by the exchange terms on the right-hand side of Eq. (15). For resolving the phase interface of a single bubble, the computational cell size typically needs to be one or two orders of magnitude smaller than the bubble diameter. Consequently, sharp interface methods [65], even with modern high-performance computing environments, are limited to investigations that involve a rather small number of individual bubbles [64].

3.2.2 *Bubbly Flow Model*

When the vapor phase is fully dispersed, i.e., $\psi \ll 1$, one can resort to Eulerian-Lagrangian or bubbly-flow models. The liquid phase is treated as a continuum while bubbles are treated as dispersed particles in a Lagrangian frame of reference [99]. Newton's second law governs the motion of such bubble particles, and the Rayleigh-Plesset equation, or simplified versions thereof, can be used to evolve the bubble geometry according to the surrounding flow-field properties. Bubbly-flow models are especially well suited for predicting incipient cavitation with inhomogeneous nuclei distributions. Problems are encountered once the local bubble volume fraction in a cell approaches unity, or when the radius of an individual bubble is of the same order as the cell size, i.e., if $\psi \gtrsim 1$. In this

case a special numerical treatment is necessary, e.g., distributing excess bubble volume across multiple cells [39]. To reduce the computational cost associated with tracking a large number of individual bubbles, it is also possible to track bubble clusters, each representing many identical but non-interacting bubbles, resulting in an Eulerian-Lagrangian stochastic cavitation model [9, 39]. Dumond et al. [26] proposed a stochastic-field cavitation model in a fully Eulerian framework, thus avoiding the cost and complexity of Eulerian-Lagrangian techniques while still being able to represent nuclei and bubble size distributions.

3.2.3 *Single-Fluid Model*

By defining a mixture variable as

$$\overline{\varphi} = \sum_k \frac{1}{V_i} \int_{\Omega_i} \varphi_k \chi_k \mathrm{d}\mathcal{V} = \sum_k \alpha_k \widehat{\varphi}_k, \tag{18}$$

we can sum Eq. (15) over both phases and obtain a set of transport equations for a single-fluid representation of a mixture of liquid and vapor

$$\partial_t \overline{\rho} + \nabla \cdot \overline{\rho \mathbf{u}} = \sum_k \widehat{\Gamma}_k^{\rho}, \tag{19a}$$

$$\partial_t \overline{\rho \mathbf{u}} + \nabla \cdot (\overline{\rho \mathbf{u}\mathbf{u}} + \overline{p}\mathbf{I} - \overline{\boldsymbol{\tau}}) = \sum_k \widehat{\boldsymbol{\Gamma}}_k^{\rho u}, \tag{19b}$$

$$\partial_t \overline{\rho E} + \nabla \cdot (\overline{\rho E \mathbf{u}} + \overline{p\mathbf{u}} - \overline{\boldsymbol{\tau} \cdot \mathbf{u}} + \overline{\mathbf{q}}) = \sum_k \widehat{\Gamma}_k^{\rho E}. \tag{19c}$$

For a massless interface, i.e., a sharp discontinuity, and a continuous tangential velocity at the phase interface (no-slip condition), the following conditions for mass, momentum and energy hold at the interface [19]

$$\sum_k \widehat{\Gamma}_k^{\rho} = 0, \tag{20a}$$

$$\sum_k \widehat{\Gamma}_k^{\rho u} = -\nabla_s \sigma + (\nabla_s \cdot \mathbf{n}_s)\sigma \mathbf{n}_s, \tag{20b}$$

$$\sum_k \widehat{\Gamma}_k^{\rho E} = -\nabla_s \cdot (\sigma \mathbf{u}_t), \tag{20c}$$

where $\mathbf{n}_s$ is the unit normal vector of the phase interface, ∇_s is the surface derivative operator, σ is the surface tension, and $\mathbf{u}_t$ is the tangential velocity at the interface. In Eq. (20b) the first term accounts for Marangoni forces while the second term accounts for capillary forces. Note that due to entropy considerations a possible surface heat flux must vanish if the interface is assumed to be massless [19], and work due to surface tension is the only term remaining in jump condition (20c) for the total energy.

For employing a one-fluid model it is generally necessary to capture or track the phase interface. VOF methods [49] solve an additional transport equation for a phase indicator or a volume fraction. Front-tracking

methods [59, 110] track the phase interface in a Lagrangian fashion. Surface tension effects due to the right-hand sides of Eqs. (20b) and (20c) can be included in these methods. With VOF methods, it is possible to reconstruct the phase interface unit normal $\mathbf{n}_s$ from the volume fraction in order to include surface tension effects, see for example Brackbill et al. [16] Alternatively, suitable material properties can be advected [57, 58], and optimized software running on millions of compute cores allows to study vapor cloud collapses with up to 15000 individual bubbles [86].

3.3 TWO-PHASE AND TURBULENCE MODELING FOR LES

The discussion on modeling two-phase flows so far implied – with the exception of the bubbly flow model, see Section 3.2.2 – that the smallest scales (phase interfaces and turbulent eddies) are resolved, i.e., $\psi \gg 1$ is satisfied in all cases.

In LES, however, we reduce the degrees of freedom by deliberately choosing a grid that is too coarse to resolve small scales. It is then assumed that small scales are of universal nature and that their effect on the resolved scales can be modeled. This scale-separation can be formally achieved by introducing a linear low-pass filter operation which leads to SGS residuals. Projection of the filtered flow field onto the numerical grid introduces another filter step. The numerical grid of a finite volume method and the associated volume averages defined by Eq. (11), for example, correspond to a top-hat filter step. The filter step associated with the grid projection can be partially reversed by reconstruction or deconvolution of the flow field from cell averages (*soft deconvolution problem*). Non-represented scales cannot be recovered which constitutes the so-called *hard deconvolution problem*. For a comprehensive introduction to filtering and the mathematics of incompressible and compressible LES we refer the interested reader to the textbooks of Sagaut [87] and Garnier et al. [35], respectively.

One approach for modeling the effect of unresolved scales on resolved scales is to approximate the unclosed SGS residuals by the resolved ones (*explicit* SGS models). Explicit SGS models rely on the assumption that truncation errors introduced by discretization schemes are small. Even centered schemes, which are formally non-dissipative for linear transport equations, can have truncation errors on the order of the contribution from subgrid scales and can thus outweigh the effect of the explicit SGS model [61].

Alternatively, one can scrutinize the truncation error of a discretization scheme in order to model the effect of unresolved scales (*implicit* LES). The textbook edited by Grinstein et al. [44] contains different approaches to implicit LES. An advantage of implicit LES is that no additional terms need to be computed and the unaltered equations governing the fluid flow are solved with the possibility of better computational performance. One common approach for implicit SGS are so-called Monotonically Integrated Large Eddy Simulations (MILESs) where existing discretization schemes

are used. Since only mathematical constraints are often considered in the design of discretization schemes it is not guaranteed that the truncation error provides the correct energy transfer between resolved and unresolved scales. The approaches followed in this work, see Chapter 4 and Chapter 7, set themselves apart from classical MILES approaches in the sense that physical reasoning is put into the design of the truncation error. Suitable numerical flux functions which contain free parameters are then used to design the truncation error so that it is physically consistent with turbulence theory.

For isothermal multiphase flow without phase change and with VOF methods in mind, Labourasse et al. [62] discuss various aspects related to volume-averaging or filtering the single-fluid representation of multiphase flow (19) and the resulting subgrid terms. For example, subgrid capillary forces result from filtering the surface-tension-related terms in the momentum jump condition (20b). Nevertheless, they show in a-priori-studies that the subgrid term resulting from filtering the non-linear term $\rho \mathbf{u}\mathbf{u}$ in the momentum equation still provides the dominant SGS contribution. A priori tests demonstrate that conventional eddy-viscosity SGS models, e.g., the Smagorinsky model, cannot predict the correct behavior of subgrid scales in two-phase flows, especially in the vicinity of phase interfaces. Vincent et al. [111] performed an a priori analysis of the relative importance of subgrid terms for a phase separation problem of oil in water. They conclude that an increase of surface tension subgrid contributions and the decrease of interfacial area are the dominant effects of filtering. Recently, Aniszewski et al. [10] proposed a closure of the subgrid surface tension term by means of approximate deconvolution [106]. Note, however, that all these studies were performed with VOF methods for isothermal flows without phase change in mind. For cavitating flow, such studies are unknown to the author.

In addition to heavily distorted phase interfaces that cannot be resolved on the underlying grid cavitating flows comprise a wide range of cavitation structures or topologies, such as isolated vapor bubbles, sheet cavities, cavitation clouds with several thousand individual vapor bubbles, or cavitating vortices [33]. With today's computational resources and with industrial applications in mind, it is infeasible to resolve such cavitation structures. Thus, it is desirable that the employed cavitation model is valid across the entire range of ψ. As a consequence, we consider a fully homogenized fluid in Section 3.4 and do not attempt to reconstruct phase interfaces.

3.4 THERMODYNAMIC EQUILIBRIUM CAVITATION MODEL

For the considered cases in this work we solve the governing equations (19) for the homogeneous mixture of liquid and vapor in local thermodynamic equilibrium, see Section 3.4, by a finite volume method, see Section 3.1.

Neglecting forces due to variable surface tension and due to curvature of phase interfaces, the right-hand sides of Eqs. (20b) and (20c) vanish and we obtain mechanical equilibrium at phase interfaces, i.e., $\overline{p} = \widehat{p}_v = \widehat{p}_l$.

Thus, the governing equations (19) reduce to the common Navier-Stokes equations that read in integral form

$$\partial_t \int_\Omega \mathbf{U} \mathrm{d}V + \int_{\partial\Omega} [\mathbf{C}(\mathbf{U}) + \mathbf{D}(\mathbf{U})] \, \mathrm{d}A = 0, \tag{21}$$

where $\mathbf{U} = [\rho, \rho\mathbf{u}, \rho E]$ is the vector of conserved variables. For later convenience the total physical flux is split into its inviscid part

$$\mathbf{C}(\mathbf{U}) = (\mathbf{n} \cdot \mathbf{u}) \begin{bmatrix} \rho \\ \rho\mathbf{u} \\ \rho E + p \end{bmatrix} + p \begin{bmatrix} 0 \\ \mathbf{n} \\ 0 \end{bmatrix}, \tag{22}$$

and its viscous part

$$\mathbf{D}(\mathbf{U}) = - \begin{bmatrix} 0 \\ \mathbf{n} \cdot \boldsymbol{\tau} \\ \mathbf{n} \cdot (\mathbf{u} \cdot \boldsymbol{\tau} - \mathbf{q}) \end{bmatrix}. \tag{23}$$

Phase change due to evaporation and condensation can be considered by an additional transport equation for one of the volume fractions α_k. E.g., for vapor volume fraction α_v we obtain the following transport equation

$$\partial_t (\alpha_v \widehat{\rho}_v) + \nabla \cdot (\alpha_v \widehat{\rho}_v \widetilde{\mathbf{u}}) = \widehat{\Gamma}_v^\rho. \tag{24}$$

The mass jump condition (20a) ensures conservation of mass since $\widehat{\Gamma}_v^\rho = -\widehat{\Gamma}_l^\rho$. The mass exchange term $\widehat{\Gamma}_l^\rho$ needs to be modeled, for example by means of finite-rate mass transfer models, which are often derived from bubble dynamics according to the Rayleigh-Plesset equation [96, 103]. A common feature of all mass transfer models are empirical parameters that need to be calibrated. Tseng & Wang [109] find, for example, that evaporation and condensation coefficients are strongly case dependent and additionally depend on the turbulence closure.

A straightforward approach to model $\widehat{\Gamma}_v^\rho$ and to close Eq. (24) is to introduce a relaxation time τ

$$\widehat{\Gamma}_v^\rho = -\frac{\widehat{\rho}_v (\alpha_v - \alpha_{v,eq})}{\tau}, \tag{25}$$

where $\alpha_{v,eq}$ denotes the local equilibrium vapor volume fraction. τ is generally unknown and cannot be easily derived. However, the limits $\tau \to \infty$ and $\tau \to 0$ can be considered without any further modeling assumptions. For $\tau \to \infty$, the flow is called frozen and the initial composition of the flow remains unchanged for all times. On the other hand, if $\tau \to 0$, the flow is assumed to be in local thermodynamic and phase equilibrium, i.e., $\overline{T} = \widehat{T}_v = \widehat{T}_l$ and $\overline{g} = \widehat{g}_v = \widehat{g}_l$, where g_k denotes the Gibbs free energy. Therefore, we obtain $\alpha_v = \alpha_{v,eq}$ at each point in space and time.

Adopting the local thermodynamic and phase equilibrium assumption leads to a parameter-free thermodynamic equilibrium cavitation model. In this case, we can compute the vapor volume fraction immediately from the mixture density $\overline{\rho}$ and saturation densities of liquid and vapor, $\rho_{l,sat}$ and $\rho_{v,sat}$ at the equilibrium temperature $\overline{T}$ without solving Eq. (24) explicitly

$$\alpha_v = \alpha_{v,eq} = \begin{cases} 0 & \text{, if } \overline{\rho} \geq \rho_{l,sat}(\overline{T}) \\ \dfrac{\rho_{l,sat}(\overline{T}) - \overline{\rho}}{\rho_{l,sat}(\overline{T}) - \rho_{v,sat}(\overline{T})} & \text{, else} \end{cases} . \tag{26}$$

$\overline{T}$ is computed from the definition of the mixture internal energy $\widetilde{e}$

$$\widetilde{e} = \frac{1}{\overline{\rho}} \sum_k \alpha_k \widehat{\rho}_k \widehat{e}_k \tag{27}$$

and the constitutive equations for the liquid and vapor phase, which can be represented either by closed-form equations of state [90] or by tabulated data [25]. For thermodynamic closures used in this work see Section 3.5.

For viscous calculations, we need to define material properties of the mixture. We follow Beattie and Whalley [13] and assume that the effective dynamic viscosity of the liquid-vapor mixture satisfies a quadratic law with a maximum in the two-phase region

$$\overline{\mu}(\overline{\rho}, \overline{T}) = \alpha_l \left(1 + \frac{5}{2}\alpha_v\right) \mu_l(\rho_l, \overline{T}) + \alpha_v \mu_v(\rho_v, \overline{T}). \tag{28}$$

The factor $(1 + 5\alpha_v/2)$ in the first term on the right-hand side of Eq. (28) accounts for fully immersed small vapor bubbles which are assumed to behave like a large number of small rigid particles in a liquid, as derived by Einstein [31] for a suspension. Strictly speaking, Einstein's derivation is only valid for small α_v. Due to blending with the liquid volume fraction, $\alpha_l = 1 - \alpha_v$, the effect decreases with increasing vapor volume fraction α_v. The maximum mixture viscosity is at $\alpha_v \approx 0.3$ since $\mu_v \ll \mu_l$. The employed mixture dynamic viscosity can also be considered as an heuristic approach to include subgrid effects of non-resolved vapor bubbles. The thermal conductivity of the liquid-vapor mixture is approximated by

$$\overline{k}(\overline{\rho}, \overline{T}) = \alpha_l k_l(\rho_l, \overline{T}) + \alpha_v k_v(\rho_v, \overline{T}). \tag{29}$$

Cavitation originates from local expansion waves which are isentropic processes. From thermodynamic considerations, we cannot obtain pure vapor, i.e., $\alpha = 1$, if cavitation is considered only and boiling processes are excluded. Besides a temperature decrease due to expansion, cavitation additionally leads to a local sub-cooling of the fluid since the surrounding liquid needs to provide the latent heat of evaporation. If expansion waves are sufficiently strong, sub-cooling could lead to temperatures below the triple line and icing. The thermodynamic closures which we will employ in the following, are, however, not valid for temperatures below

the triple line. Furthermore, the thermodynamic closures for water do not include the anomalous behavior of water density at a temperature of approximately 277 K. Therefore, we limit density to values above a certain threshold ρ_{min}. This limit is chosen as $\rho_{min} = 5$ kg/m^3 for ALDM and $\rho_{min} = 1$ kg/m^3 for CATUM which corresponds to maximum vapor volume fractions of $\alpha_{max} \approx 99.5$ % and $\alpha_{max} \approx 99.9$ %, respectively.

3.5 THERMODYNAMIC CLOSURES

3.5.1 *Water*

We adopt the thermodynamic closure of Saurel *et al.* [90], who use a modified Tait equation of state in pure liquid regions

$$\overline{p}(\overline{\rho}, \overline{T}) = \left(p_{sat}(\overline{T}) + B\right)\left(\frac{\overline{\rho}}{\rho_{l,sat}(\overline{T})}\right)^N - B \tag{30}$$

where $p_{sat}(\overline{T})$ and $\rho_{l,sat}(\overline{T})$ are the temperature-dependent saturation pressure and saturation density of liquid water. $B = 3.06 \times 10^8$ Pa and $N = 7.1$ are fitted constants. An efficient equation for the specific internal energy of pure liquid is given by [90]

$$e_l(T) = c_{v,l}(\overline{T} - T_0) + e_{l,0} \tag{31}$$

with constant specific heat at constant volume $c_{v,l}$ and reference energy $e_{l,0}$ at reference temperature T_0. For water $c_{v,l} = 4.18$ kJ/kg K and $e_{l,0} = 0.617$ kJ/kg K at $T_0 = 273.15$ K.

Within the thermodynamic equilibrium cavitation model, Section 3.4, a unique $(\overline{p}, \overline{T})$ state defines the saturated liquid-vapor mixture with $\overline{p} = p_{sat}(\overline{T}) = p_v = p_l$ and $\overline{T} = T_{sat} = T_v = T_l$. The temperature-dependent saturation pressure, and saturated liquid and vapor densities are approximated by [91]

$$p_{sat}(\overline{T}) = p_c \exp\left[\left(\frac{T_c}{\overline{T}}\right)\sum_{i=1}^{6} a_i \theta^{m_i}\right], \tag{32a}$$

$$\rho_{l,sat}(\overline{T}) = \rho_c \left(1 + \sum_{i=1}^{6} b_i \theta^{n_i}\right), \tag{32b}$$

$$\rho_{v,sat}(\overline{T}) = \rho_c \exp\left(\sum_{i=1}^{6} c_i \theta^{o_i}\right). \tag{32c}$$

with $\theta = 1 - \overline{T}/T_c$. The subscript "c" denotes temperature, pressure and density at the critical point. For water $\rho_c = 332$ kg/m^3, $p_c = 22.64 \times 10^5$ Pa and $T_c = 647.14$ K. Coefficients a_i, b_i, and c_i and exponents m_i, n_i, and o_i for water are given in Table 2. The saturation temperature is determined

Table 2: Coefficients and exponents for equations (32) defining the saturation pressure and densities of water [91].

i	a_i	m_i	b_i	n_i	c_i	o_i
1	−7.85823	1.	1.99206	1/3	−2.02957	2/6
2	1.83991	1.5	1.10123	2/3	−2.68781	4/6
3	−11.7811	3.	−0.512506	5/3	−5.38107	8/6
4	22.6705	3.5	−1.75263	16/3	−17.3151	18/6
5	−15.9393	4.	−45.4485	43/3	−44.6384	37/6
6	1.77516	7.5	-6.75615×10^5	110/3	−64.3486	71/6

from the following equation for the specific internal energy of the liquid-vapor mixture [90]

$$\overline{e}(T) = \frac{1}{\overline{\rho}}\left\{\left[\alpha\rho_{v,sat}(\overline{T})c_{v,v} + (1-\alpha)\rho_{l,sat}(\overline{T})c_{v,l}\right](\overline{T}-T_0)+ \alpha\rho_{v,sat}(\overline{T})L_{v,0}\right\} + e_{l,0}. \quad (33)$$

By solving Eq. (32) in conjunction with Eq. (33) we obtain the mixture temperature, $\overline{T}$.

The density and temperature dependency of the dynamic viscosities and heat conductivities for pure liquid and vapor needed for Eqs. (28) and (29) are computed from polynomials defined by the International Association for the Properties of Water and Steam (IAPWS) neglecting critical enhancement [2, 3].

3.5.2 *Barotropic Model for Water*

A simplified model for water can be derived if we assume that pressure is a function of density only (barotropic assumption). The modified Tait equation (30) reduces to an isentropic constitutive equation for a reference temperature T_{ref}

$$\overline{p}(\overline{\rho})|_{s=const.} = (p_{sat}(T_{ref}) + B)\left(\frac{\overline{\rho}}{\rho_{l,sat}(T_{ref})}\right)^N - B, \quad (34)$$

where $B = 3.06\times10^8$ Pa, and $N = 7.1$ are fitted constants. In two-phase regions, the equilibrium pressure is deduced by following an isentropic path in the phase diagram, i.e., for $\overline{\rho} < \rho_{l,sat}(T_{ref})$

$$\overline{p}(\overline{\rho})|_{s=const.} = p_{sat}(T_{ref}) + C\left(\frac{1}{\rho_{l,sat}(T_{ref})} - \frac{1}{\overline{\rho}}\right). \quad (35)$$

For a reference temperature $T_{ref} = 293.15$ K we use $C = 1468.54$ Pa kg/m^3 and $p_{sat}(T_{ref}) = 2340$ Pa, $\rho_{l,sat}(T_{ref}) = 998.1618$ kg/m^3, and $\rho_{v,sat}(T_{ref}) =$

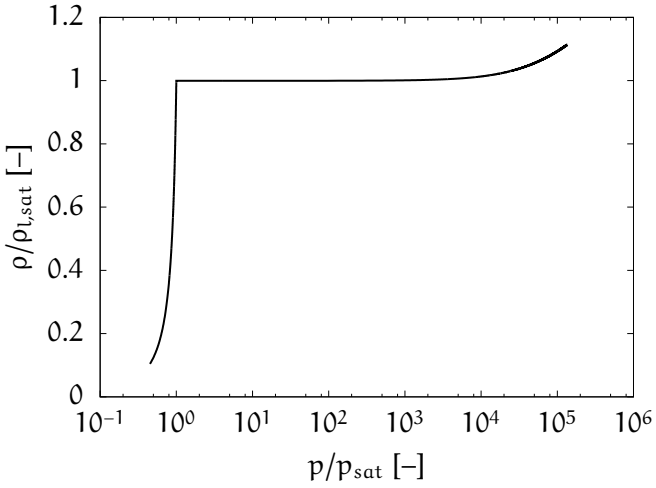

Figure 2: Isentropic relationship between pressure and density for the Diesel-like test fluid Shell V-oil 1404 (ISO 4113) at T_{ref} = 293.15 K. *Reprinted with permission from Egerer et al. [29]. Copyright 2014, AIP Publishing LLC.*

0.01731 kg/m^3 for the saturation pressure and densities of water. The speed of sound for liquid water and the liquid-vapor mixture is the equilibrium speed of sound.

The dynamic viscosities for liquid water and water vapor are assumed to be constant and equal to their saturation values at the reference temperature T_{ref}. For T_{ref} = 293.15 K we use $\mu_{l,sat}(T_{ref}) = 1.002 \times 10^{-3}$ Pa s and $\mu_{v,sat}(T_{ref}) = 9.727 \times 10^{-6}$ Pa s.

Since pressure is a function of density only, the solution of the energy equation (19c) is not necessary in this case.

3.5.3 *Barotropic Model for a Diesel-like Test Fluid*

The isentropic equation of state, $\overline{p} = \overline{p}(\overline{\rho})|_{\overline{s}=const.}$, for a barotropic model of a typical Diesel-like test fluid (Shell V-oil 1404, ISO 4113) at reference temperature T_{ref} = 293.15 K is used in tabulated form and plotted in Fig. 2. The table also contains values of the vapor volume fraction $\alpha = \alpha_v$ at a given density. The speed of sound in the liquid and in the mixture is the equilibrium speed of sound, $c_{eq} = \sqrt{\partial\overline{p}/\partial\overline{\rho}}|_{\overline{s}=const.}$. Linear interpolation is used between two subsequent table values. For thermodynamic states outside of the table, linear extrapolation is employed. Characteristic properties of the test fluid are given in Table 3. Since pressure is a function of density only, the solution of the energy equation (19c) is also not necessary in this case.

3.6 MODEL SUMMARY

We employ a single-fluid approach for modeling turbulent cavitating flows with the following underlying assumptions:

Table 3: Characteristic properties of the Diesel-like test fluid Shell V-oil 1404 (ISO 4113) at T_{ref} = 293.15 K. *Reprinted with permission from Egerer et al. [29]. Copyright 2014, AIP Publishing LLC.*

Property	p_{sat}	$\rho_{l,sat}$	$\rho_{v,sat}$	c_l	$\mu_{l,sat}$	$\mu_{v,sat}$
Unit	Pa	kg/m^3	kg/m^3	m/s	mPa s	µPa s
Value	2218	820	0.12	1363	3.1	0.1

- ❏ phase change, i.e., evaporation and condensation, is in thermodynamic and phase equilibrium resulting in single-valued temperature and Gibbs free energy for the liquid-vapor mixture, i.e., $\overline{T} = \widehat{T}_v = \widehat{T}_l$ and $\overline{g} = \widehat{g}_v = \widehat{g}_l$;
- ❏ mechanical equilibrium, i.e., $\overline{p} = \widehat{p}_v = \widehat{p}_l$ is assumed at phase interfaces; surface tension effects are neglected;
- ❏ fluid quality (i.e., nuclei content) is not explicitly modeled, it is assumed that a sufficient amount of nucleation sites are present;
- ❏ effects of non-condensable gas are not considered.

These assumptions are well justified for the types of application in mind, as discussed in Section 3.4. They result in a parameter-free thermodynamic equilibrium cavitation model which is mathematically consistent for any length-scale ratio ψ. The mixture evolution equations are formally the same as for single-phase flow facilitating the use of standard LES methods. Modeling of two-phase flows using the thermodynamic equilibrium cavitation model presented in Section 3.4 has proven to be able to accurately describe cavitating flows. The model has been successfully applied for the prediction of inertia driven sheet and cloud cavitation of twisted and non-twisted hydrofoils [95, 97], and the prediction of cavitation including shock-wave dynamics in bore holes of injection nozzles [98]. The fully compressible treatment of the liquid and liquid-vapor mixture reproduces the formation and propagation of shock waves due to the collapse of vapor structures, which is essential for the prediction and quantitative analysis of surface erosion [74]. Conceptual extension from an inviscid framework to compressible LES has been demonstrated by Hickel et al. [48] Further validation for applying this modeling methodology for LES of turbulent cavitating flows will be presented in Chapter 5.

Part II

REFERENCE LARGE-EDDY SIMULATION METHOD FOR FLOWS WITH CAVITATION

Major parts are based on the author's journal article [29] and are reprinted with permission from Egerer et al. (2014) "Large-eddy simulation of turbulent cavitating flow in a micro channel", *Physics of Fluids* 26(8): 085102. Copyright 2014, AIP Publishing LLC.

4 THE ADAPTIVE LOCAL DECONVOLUTION METHOD FOR CAVITATING FLOWS

A framework for implicitly modeling SGS stresses that is consistent with turbulence theory is provided by the Adaptive Local Deconvolution Method (ALDM). It was first developed for incompressible flows [46] and later extended to compressible flows [47]. Further modifications to compressible ALDM [47] are necessary to obtain a robust scheme with respect to large density gradients and large variations of the speed of sound [48] in cavitating flows.

ALDM is designed for Cartesian grids and operates on the inviscid part of the governing equations (19), which, e.g., read for the j-th coordinate direction

$$\nabla\cdot\overline{\mathbf{C}}=\nabla\cdot\begin{bmatrix}\overline{C}^{\rho}\\ \overline{C}_j^{\rho u_j}\\ \overline{C}^{\rho E}\end{bmatrix}=\nabla\cdot\begin{bmatrix}\overline{\rho\mathbf{u}}\\ \overline{\rho u_j\mathbf{u}}+\overline{p}\delta_{ij}\\ \overline{\rho E\mathbf{u}}+\overline{p\mathbf{u}}\end{bmatrix}=\int\limits_{\partial\Omega}\begin{bmatrix}\rho\mathbf{u}\\ \rho u_j\mathbf{u}+p\delta_{ij}\\ (\rho E+p)\mathbf{u}\end{bmatrix}\cdot\mathbf{n}\,dS, \tag{36}$$

where $\mathbf{n}$ is the unit normal of the cell-surface increment dS and δ_{ij} is the Kronecker delta.

In general, ALDM reconstructs the primitive variables $\varphi=[\rho,u_i,\rho e,p]$ at cell faces from their cell averages by combining Harten-type deconvolution polynomials,

$$\breve{g}^{\mp}_{k,r}(x_{j\pm1/2})=\sum_{l=0}^{k-1}c^{\mp}_{k,r,l}(x_j)\overline{\varphi}(x_{j-r+l}), \tag{37}$$

up to order three non-linearly and solution-adaptively

$$\breve{\varphi}^{\pm}=\sum_{k=1}^{3}\sum_{r=0}^{k-1}\omega^{\pm}_{k,r}(\gamma_{k,r},\overline{\varphi})\breve{g}^{\pm}_{k,r}. \tag{38}$$

The coefficients $c^{\mp}_{k,r,l}(x_j)$ are grid-dependent [46]. Note that "+" and "−" superscripts are used to distinguish between values associated with the right or left side of the considered cell face. By dynamically weighting different orders of accuracy $\breve{g}^{\mp}_{k,r}(x_{j\pm1/2})$ in the reconstruction procedure (38) solution-adaptivity is obtained. Free parameters γ_{kr} in the weights

$$\omega^{\mp}_{k,r}(\gamma_{k,r},\overline{\varphi})=\frac{\gamma^{\lambda}_{k,r}\beta_{k,r}(\overline{\varphi}_j)}{\sum_{s=0}^{k-1}\gamma^{\lambda}_{k,s}\beta_{k,s}(\overline{\varphi}_j)}, \tag{39}$$

where

$$\beta_{k,r}(\overline{\varphi},x_i)=\left(\varepsilon_\beta+\sum_{l=-r}^{k-r-2}(\overline{\varphi}_{i+m+1}-\overline{\varphi}_{i+m})^2\right)^{-2} \tag{40}$$

with $\varepsilon_\beta = 10^{-99}$, are used to control the truncation error of ALDM.

A suitable numerical flux function comprising the physical inviscid flux and a secondary regularization term R is used. The generic form of the ALDM numerical flux function is

$$\check{C} = C\left(\frac{\check{\varphi}^+ + \check{\varphi}^-}{2}\right) - R\left(\varepsilon, \check{\varphi}^\pm, \overline{\varphi}\right). \tag{41}$$

The free parameters $\{\gamma_{k,r}, \varepsilon\}$ are adopted from the single-phase version of ALDM since SGS effects in isothermal two-phase turbulence are dominated by momentum fluctuations as discussed in section 3.4. For single-phase turbulence, a physically consistent implicit SGS model is obtained by optimizing $\{\gamma_{k,r}, \varepsilon\}$ so that the effective spectral numerical viscosity matches the eddy viscosity from the Eddy-Damped Quasi-Normal Markovian (EDQNM) theory in the low Mach number limit [46].

Following the methodology described above, we define the numerical approximation of the mass density, the j-th component of the momentum, and the total energy flux for the i-th coordinate direction of the Cartesian grid as

$$\check{C}_i^\rho = \check{u}_i^* \check{\rho} - \varepsilon^\rho \left|\check{u}_i^+ - \check{u}_i^-\right| \left(\check{\rho}^+ - \check{\rho}^-\right), \tag{42a}$$

$$\check{C}_i^{\rho u_j} = \check{C}_i^\rho \frac{\check{u}_j^+ + \check{u}_j^-}{2} - \varepsilon^{\rho u} \check{\rho} \left|\check{u}_j^+ - \check{u}_j^-\right| \left(\check{u}_j^+ - \check{u}_j^-\right) + \delta_{ij} \check{p}^*, \tag{42b}$$

and

$$\begin{aligned} \check{C}_i^{\rho E} = {} & \check{u}_i^* \left[\check{\rho} e + \check{p}^*\right] + \frac{\check{u}_j^+ + \check{u}_j^-}{2} \cdot \left(\check{C}_i^{\rho u_j} - \frac{\check{u}_j^+ + \check{u}_j^-}{4} \check{C}_i^\rho\right) \\ & - \varepsilon^{\rho E} \left|\check{u}_i^+ - \check{u}_i^-\right| \left(\check{\rho} e^+ - \check{\rho} e^-\right). \end{aligned} \tag{42c}$$

Reconstruction of the transport-velocity, $\check{u}_i^*$, in Eq. (42) follows the argument of Harten et al. [45] leading to

$$\check{u}_i^* = \frac{\check{u}_i^- + \check{u}_i^+}{2} - \frac{\check{p}^+ - \check{p}^-}{2\check{\rho}\overline{c}}, \tag{43}$$

where $\check{c}$ is the maximum speed of sound of the cells adjacent to the considered cell face.

Low-Mach-number consistency is achieved by computing the cell face pressure in Eq. (42), $\check{p}^*$, from the arithmetic mean of the right- and left-side reconstructed values

$$\check{p}^* = \frac{\check{p}^+ + \check{p}^-}{2}. \tag{44}$$

The free parameters take the values $\varepsilon^{\rho u} = 0.125$ and $\varepsilon^\rho = \varepsilon^{\rho E} = 0.615$, and are directly adopted from the compressible single-phase version of ALDM.

The contribution to the flux from viscous stresses and heat conduction is discretized by a linear second-order centered scheme. For ALDM time

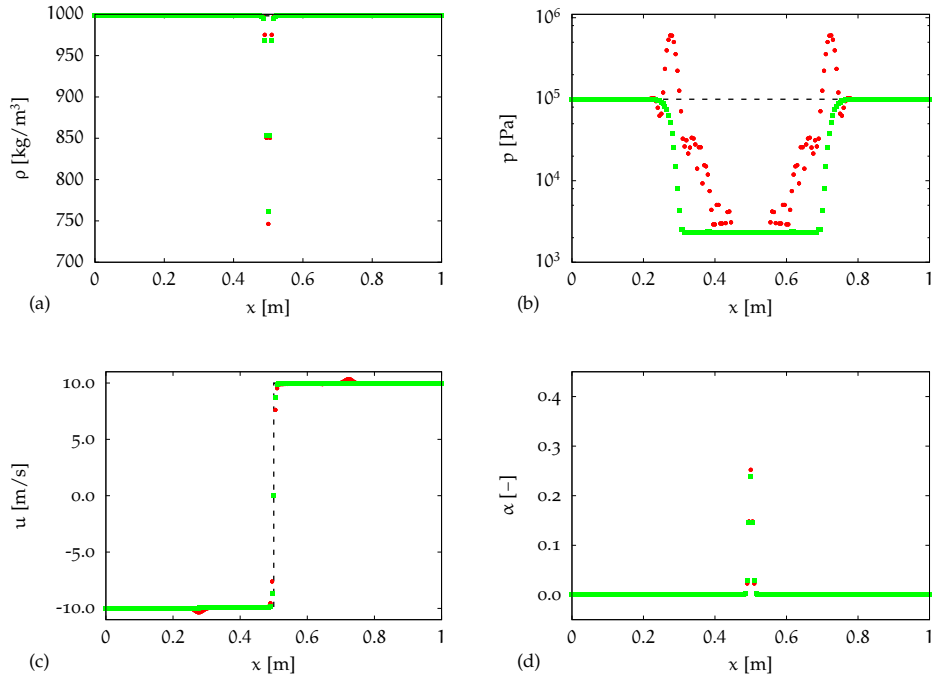

Figure 3: Comparison between compressible ALDM (•) and ALDM adapted for cavitating flows (▪) for a 1-D double expansion in water at time $t = 0.15 \times 10^{-3}$ s. - - - - initial condition.

integration is performed by the TVD explicit RK3S3 method [42], see Section 3.1.

A simple 1-D test shows, however, that the original compressible formulation of ALDM [47] is numerically not stable and produces large pressure oscillations at phase interfaces as can be seen in the results for a double expansion in water, see Fig. 3b. For the initial conditions and set-up we refer the reader to Section 8.1.3. Results are shown at time $t = 0.15 \times 10^{-3}$ s. Furthermore, we observe spurious velocities at the positions where the pressure drops to vapor pressure due to the expansion, see Fig. 3c.

A robust version of ALDM suitable for cavitating flows is obtained by employing an upwind reconstruction of the transported density and internal energy density at cell faces

$$\varphi^U = [\rho^U, (\rho e)^U] = \frac{1}{2}\left[(1 + \operatorname{sgn}(\breve{u}_i^*))\overline{\varphi}^- + (1 - \operatorname{sgn}(\breve{u}_i^*))\overline{\varphi}^+\right] \tag{45}$$

instead of using the solution-adaptive deconvolution (38). The ALDM flux for cavitating flows then reads

$$\breve{C}_i^\rho = \breve{u}_i^* \rho^U - \varepsilon^\rho \left|\breve{u}_i^+ - \breve{u}_i^-\right| (\breve{\rho}^+ - \breve{\rho}^-), \tag{46a}$$

$$\breve{C}_i^{\rho u_j} = \breve{C}_i^\rho \frac{\breve{u}_j^+ + \breve{u}_j^-}{2} - \varepsilon^{\rho u} \rho^U \left|\breve{u}_j^+ - \breve{u}_j^-\right| \left(\breve{u}_j^+ - \breve{u}_j^-\right) + \delta_{ij} \breve{p}^*, \tag{46b}$$

and

$$\begin{aligned}\check{C}_i^{\rho E} = \check{u}_i^* \left[(\rho e)^U + \check{p}^*\right] + \frac{\check{u}_j^+ + \check{u}_j^-}{2} \cdot \left(\check{C}_i^{\rho u_j} - \frac{\check{u}_j^+ + \check{u}_j^-}{4} \check{C}_i^{\rho}\right) \\ - \varepsilon^{\rho E} |\check{u}_i^+ - \check{u}_i^-| \, (\rho\check{e}^+ - \rho\check{e}^-).\end{aligned} \tag{46c}$$

The transport velocity (43) is slightly modified as

$$\check{u}_i^* = \frac{\check{u}_i^- + \check{u}_i^+}{2} - \frac{\check{p}^+ - \check{p}^-}{\check{\rho}^+ \left(S_R - \check{u}_i^+\right) - \check{\rho}^- \left(S_L - \check{u}_i^-\right)}, \tag{47}$$

where $S_R = \max(\check{u}_i^+, \check{u}_i^-) + c_l$, and $S_L = \min(\check{u}_i^+, \check{u}_i^-) + c_l$ denote estimates of the fastest right and left going wave speeds and c_l is the speed of sound of the liquid phase. The interface pressure $\check{p}^*$ remains unchanged.

The results for the 1-D double expansion in water show that ALDM adapted for cavitating flows is free of spurious oscillations, see Fig. 3.

5 VALIDATION OF ALDM: TURBULENT CAVITATING MIXING LAYER

For validation of ALDM adopted for cavitating flows, see Chapter 4, we consider the canonical problem of a turbulent cavitating mixing layer.

O'Hern studied cavitation inception experimentally in a mixing layer created by a sharp-edged plate [75] and finds that cavitation inception strongly depends on the air content of the liquid water and that cavitation first occurs in the streamwise secondary vortices. While O'Hern [75] only investigated the mixing layer by flash photographies and high-speed motion pictures, Iyer & Ceccio [53] additionally performed Particle Image Velocimetry (PIV) on a similar setup to measure the influence of cavitation on the flow field downstream of the cavitating mixing layer. They find that the mean flow is not altered by cavitation. Streamwise fluctuations are enhanced whereas cross-stream fluctuations decrease.

We use the more recent experiment by Aeschlimann et al. [6–8] for validation. For this case the cavitation number (1) is defined as

$$\sigma_c = \frac{2(p_\infty - p_{sat})}{\rho_\infty (\Delta U)^2}. \tag{48}$$

Aeschlimann et al. [6–8] create the mixing layer by a splitter plate, separating a high speed and a low speed flow. The velocity difference $\Delta U = U_2 - U_1$, $U_2 > U_1 > 0$, of the two separated flows and the convective velocity $U_c = (U_1 + U_2)/2$ were kept constant while the pressure p_∞ in the inlet section was controlled by a vacuum pump in order to define different cavitation numbers. The turbulent boundary layers of the splitter plate are not further specified. Aeschlimann et al. provide velocity statistics by means of PIV [6] and quantitative data of the vapor volume fraction by means of X-ray attenuation measurements [7]. They find that the self-similar behavior of the mixing layer is preserved and confirm the findings of Iyer & Ceccio [53] that the mean velocity field and the Reynolds shear stress is not altered by cavitation. Their finding of enhanced streamwise velocity fluctuations is also in agreement with the study of Iyer & Ceccio [53] but they find that the cross-stream velocity fluctuations are also enhanced contrary to the study of Iyer & Ceccio [53].

Incompressible DNS of cavitating mixing layers at very small Reynolds numbers were performed by Okabayashi & Kajishima [76]. Their findings are in agreement with Iyer & Ceccio [53] in terms of the modulation of the Reynolds stresses by cavitation.

Table 4: Simulation parameters of the spatially evolving cavitating mixing layer matching the cavitation and Reynolds number of the experiment by Aeschlimann et al. [6, 7]. *Reprinted with permission from Egerer et al. [29]. Copyright 2014, AIP Publishing LLC.*

σ_c	[–]	$1 \mathrel{\hat{=}} \infty$	0.167	0.1
ΔU	[m/s]		100.0	
U_c	[m/s]		75.0	
ρ_∞	[kg/m^3]	1000.44	998.54	998.39
p_∞	[$\times 10^5$ Pa]	50.046	8.362	5.015
T_∞	[K]		293.15	
$\delta_{\theta,0}$	[$\times 10^{-4}$ m]		0.5	
$\delta_{\omega,0}$	[$\times 10^{-4}$ m]		2.0	
$Re_{\delta_{\omega,0}}$	[–]		20000.	

5.1 COMPUTATIONAL SETUP

We investigate three cases of the experiment by Aeschlimann et al. [6–8], see Table 4. The cavitation number in the numerical simulations is controlled by adjusting the ambient pressure, p_∞, according to Table 4 while keeping the velocity difference ΔU and the convective velocity U_c constant to resemble the experimental setup. The Reynolds number

$$Re_{\delta_\omega} = \frac{\rho_\infty \Delta U \delta_\omega}{\mu_\infty}, \tag{49}$$

based on the vorticity thickness

$$\delta_\omega(x) = \frac{\Delta U}{\partial \langle u \rangle / \partial y|_{max}} \tag{50}$$

at the beginning of the self-similar region is approximately $Re_{\delta_{\omega,ss0}} = 1.5 \times 10^5$ in the experiment. We choose the initial mixing layer vorticity thickness $\delta_{\omega,0}$ in the LES so that Re_{δ_ω} of the LES and the experiment are approximately equal at the beginning of the self-similar region.

The computational domain, see Fig. 4, comprises an analysis region of size $L_x = 300\delta_{\omega,0}$, $L_y = 120\delta_{\omega,0}$, and $L_z = 75\delta_{\omega,0}$ in streamwise, cross-stream, and spanwise direction, respectively. The analysis region is embedded in a larger domain of size $L_{x,o} = 450\delta_{\omega,0}$ and $L_{y,o} = 240\delta_{\omega,0}$, that is utilized to reduce the influence of the cross-stream and outlet boundary conditions. Since the domain is periodic in spanwise direction, $L_{z,o} = L_z$.

Results presented below have been computed on a *coarse*, *medium*, and *fine* Cartesian grid. The coarse grid is shown in Fig. 5. The streamwise and spanwise grid spacing Δx and Δz are equidistant in the analysis region for all grid resolutions, see Figs. 5a and 5b. The medium grid was obtained from the coarse grid by halfing the grid spacing in these directions, while the fine grid was obtained by taking 2/3 of the medium grid spacing.

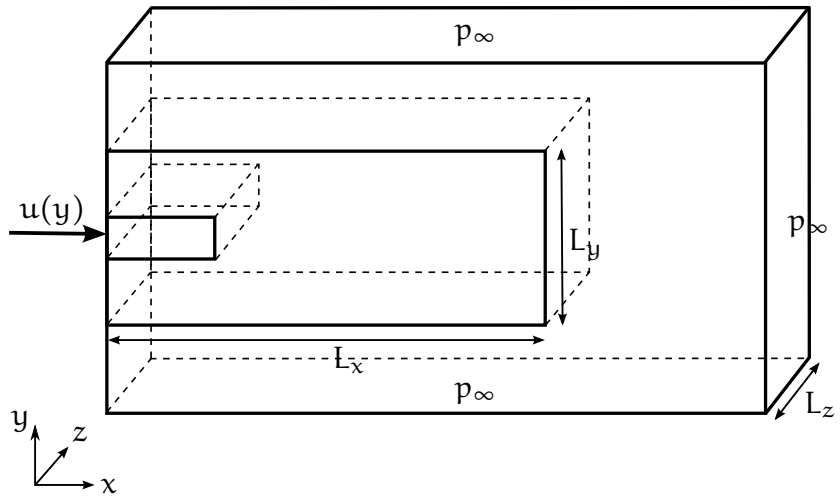

Figure 4: Sketch of the computational domain for the cavitating mixing layer. *Reprinted with permission from Egerer et al. [29]. Copyright 2014, AIP Publishing LLC.*

Table 5: Grid parameters for the cavitating mixing layer.

grid	*coarse*	*medium*	*fine*
$\Delta x/\delta_{\omega,0}$	2.344	1.172	0.586
$\Delta y/\delta_{\omega,0}$	2.5	1.250	0.625
$\Delta z/\delta_{\omega,0}$	2.344	1.172	0.586
N_{cells} [$\times 10^6$]	1.92	14.97	50.51

For the cross-stream direction the grid was refined towards the mixing layer interface in a zone of size $L_{x,i} = 75\delta_{\omega,0}$, $L_{y,i} = 30\delta_{\omega,0}$, and $L_{z,i} = L_z$ at the inlet of the computational domain, see Fig. 4 and Figs. 5a and 5c. On the coarse grid, two refinement steps exist with $\Delta y/2$ and $\Delta y/4$ with respect to the equidistant Δy in the remainder of the analysis region. For the medium and fine grid only one refinement step with $\Delta y/2$ was used.

The grid spacings in the analysis region in terms of the initial vorticity thickness $\delta_{\omega,0}$ and the total number of cells, N_{cells}, are provided in Table 5.

The inlet boundary condition for the mean streamwise velocity component is a hyberbolic tangent profile, and zero mean velocity in cross-stream and spanwise direction

$$\mathbf{u}(x = 0, y, z) = \left(U_c + \frac{\Delta U}{2}\tanh\left(-\frac{2y}{\delta_{\omega,0}}\right)\right)\begin{bmatrix}1\\0\\0\end{bmatrix}. \tag{51}$$

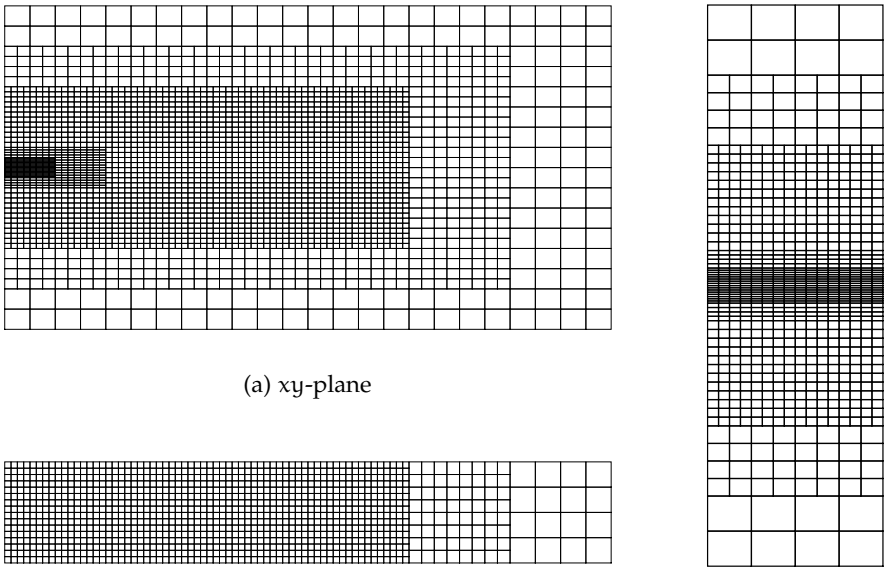

(a) xy-plane

(b) xz-plane

(c) yz-plane

Figure 5: Computational grid for the spatially evolving cavitating mixing layer LES. Every 4th grid line in stream- and spanwise directions, and every 3rd grid line in cross-stream direction is shown for the *coarse* grid.

The cell-averaged velocity components at the inlet boundary are applied by integrating profile (51) over the cross-stream cell height Δy, i.e.,

$$\overline{\mathbf{u}}(x = 0) = \frac{1}{\Delta y} \int_{-\Delta y/2}^{+\Delta y/2} \mathbf{u}(y) dy. \tag{52}$$

We superimpose 3-D time-dependent random velocity fluctuations with maximum amplitudes of $0.1\Delta U$ to trigger transition. The velocity fluctuations are restricted to the initial mixing layer thickness by an exponential function, i.e.,

$$\mathbf{u}'(x = 0, y, z, t) = 0.1\Delta U \begin{bmatrix} u_r(y, z, t) \\ v_r(y, z, t) \\ w_r(y, z, t) \end{bmatrix} \exp\left(-\frac{y^2}{2\delta_{\omega,0}}\right), \tag{53}$$

where u_r, v_r, $w_r \in [-1, 1]$ are space- and time-dependent random numbers. The pressure is extrapolated linearly from the exterior. For simulations with the full thermodynamic model we addionally prescribe the density at the inlet according to the values given in Table 4. For barotropic simulations the density at the inlet is computed from the extrapolated pressure.

At the cross-stream and outlet boundaries, we impose the static pressure p_∞ according to Table 4. If $\alpha > 0$ at the cross-stream or outlet boundary, we employ an outflow boundary condition where all quantities are extrapolated; otherwise, vapor structures would collapse immediately and would cause artificial pressure waves travelling upstream.

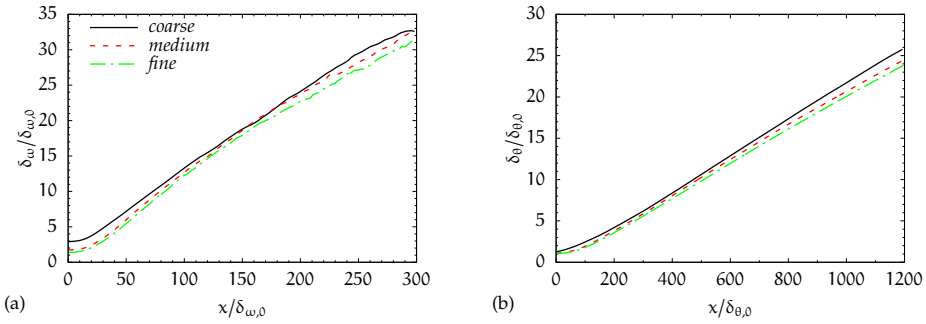

Figure 6: Grid convergence of (a) the vorticity thickness, and (b) the momentum thickness for the cavitating mixing layer with $\sigma_c = 0.167$.

The computational domain on the coarse grid is initialized with the mean velocity profile and random fluctuations according to Eqs. (51) and (53) and a constant pressure and density according to the values specified in Table 4. For the medium and fine grids the flow field is initialized by interpolating the solution from the next coarser grid.

Results of the mixing layer LES presented in the following have been averaged in time and spanwise direction. Time-averaging has been performed for each grid level over 20 flow-through times of the analysis region, $t_{ft} = L_x/U_c$, after letting the flow field develop for $10t_{ft}$. Reynolds-averages are denoted by angled brackets, $\langle\circ\rangle$, while Favre-averages are defined according to Eq. (12) and denoted by a tilde, $\widetilde{\circ}$.

5.2 GRID CONVERGENCE

We demonstrate grid convergence for the cavitating mixing layer with $\sigma_c = 0.167$ by comparing first and second order statistics for the three grid resolutions specified in Table 5. In Fig. 6 we show the spatial evolution of the vorticity thickness $\delta_\omega(x)$, see Eq. (50), and the momentum thickness

$$\delta_\theta(x) = \frac{1}{\rho_\infty(\Delta U)^2}\int_{-\infty}^{\infty}\langle\rho\rangle\left(\frac{1}{2}\Delta U - \widetilde{u} + U_c\right)\left(\frac{1}{2}\Delta U + \widetilde{u} - U_c\right)dy. \tag{54}$$

Both quantities converge clearly for the medium and fine grids. Note the influence of the approximation error of the velocity gradient due to finite grid resolution used to compute the vorticity thickness at the inlet ($x = 0$). Since the momentum thickness is an integral quantity, all grids match the specified momentum thickness $\delta_{\theta,0}$ of the mean inflow velocity profile (51).

The same conclusion can be drawn for the maximum values of the cross-stream mean vapor volume fraction profiles, see Fig. 7a, and the integrated vapor volume fraction, see Fig. 7b, along the streamwise axis. Note that the discontinuities, e.g., at $x/\delta_{\omega,0} \approx 220$, are due to the change in grid resolution, cf. Fig. 5.

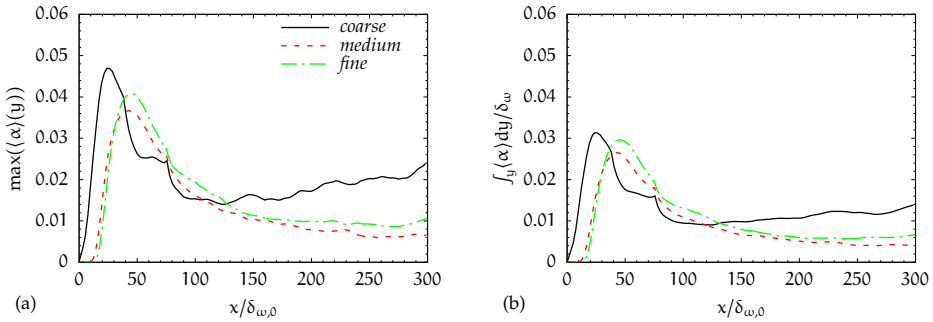

Figure 7: Grid convergence of the vapor volume fraction for the mixing layer with $\sigma_c = 0.167$: (a) maximum vapor volume fraction, and (b) normalized integrated vapor volume fraction.

For the streamwise evolution of extremal values of the non-zero Reynolds stress tensor components we observe negligible differences between the medium and fine grids, see Fig. 8. Note that discontinuities are due to the grid refinement steps and are especially observable on the coarse grid.

For completeness, we show cross-stream profiles of the mean streamwise velocity and the mean vapor volume fraction in the self-similar region at $x/\delta_{\omega,0} \approx 230$ in Fig. 9. The most notable difference can be seen in the mean vapor volume profiles. Here, the vapor content reduces by a factor of two between the coarse and medium grids. For the cross-stream profiles of the Reynolds stresses we observe only small differences between the three grids, see Fig. 10.

To sum up, the results presented for a cavitating mixing layer at $\sigma_c = 0.167$ show that statistical quantities are converged on the medium and fine grids. Further analysis will thus be conducted with results obtained on the fine grid.

5.3 TEMPERATURE EFFECTS

Fig. 11 shows instantaneous contours and iso-surfaces of the temperature difference, $\Delta T = T - T_\infty$, in the cavitating mixing layer with $\sigma_c = 0.167$. Viscous heating leads to a small temperature increase up to $\Delta T \approx +0.3$ K. Since the latent heat of evaporation needs to be provided by the surrounding liquid, we also observe small areas with an instantaneous temperature decrease below T_∞ although the effect of viscous heating is dominant. We conclude from Fig. 11 that effects due to heat conduction are negligible as a consequence of the small temperature differences. Changes of transport properties, e.g., dynamic viscosities, are thus also small. This finding justifies the application of a barotropic Equation of State (EOS) as well as constant dynamic viscosities for the pure vapor and liquid phases.

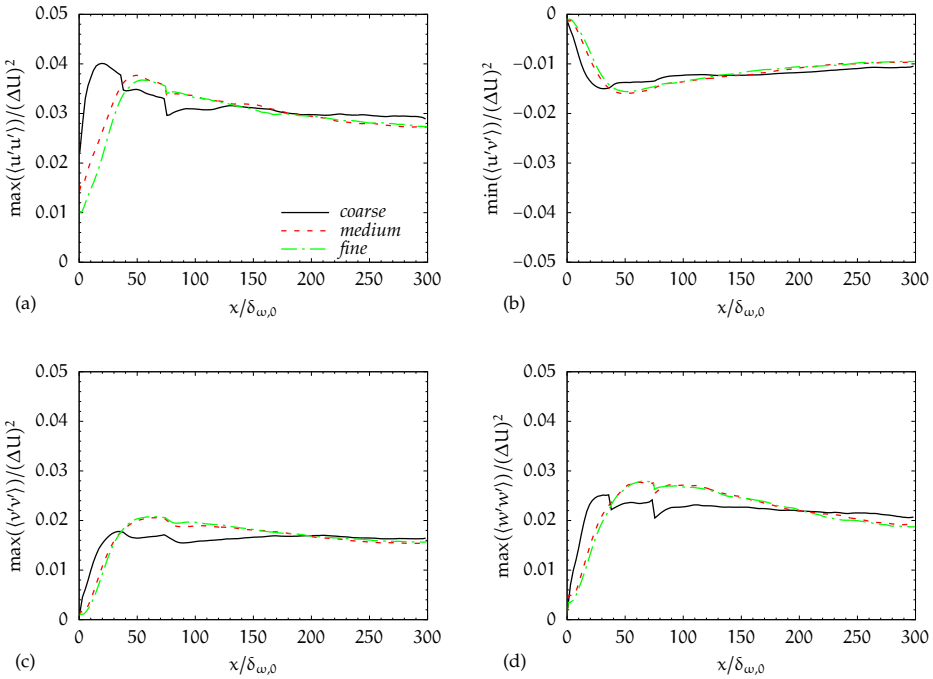

Figure 8: Grid convergence of Reynolds stresses for the mixing layer with $\sigma_c = 0.167$: (a) streamwise Reynolds stress, (b) Reynolds shear stress, (c) cross-stream Reynolds stress, and (d) spanwise Reynolds stress.

5.4 EFFECT OF CAVITATION NUMBER

5.4.1 *Flow Field*

Fig. 12 shows instantaneous 3-D visualizations of the three mixing layer cases. We observe the classical break-up mechanism for the non-cavitating mixing layer case with $\sigma_c = 1$. First, spanwise Kelvin-Helmholtz-type instabilities develop followed by secondary streamwise instabilities. After this transition process the mixing layer reaches a fully turbulent state for $x/\delta_{\omega,0} \gtrsim 50$, cf. Fig. 12a. For $\sigma_c = 1$ no vapor structures are present since this is the non-cavitating case, cf. Fig. 12d. The topology of the break-up process and the evolution of the velocity field do not change for the cavitating cases, see Figs. 12b and 12c. Further confirmation of this finding will be provided in the next Section 5.4.2.

Evaporation primarily occurs in the cores of the spanwise Kelvin-Helmholtz-type vortices but also in the streamwise secondary vortices, see Figs. 12e and 12f. For decreasing cavitation number areas with $\alpha > 0.1$ increase.

We compare predicted instantaneous cavitation structures between experiment [8] and LES in Fig. 13. Note, however, that the experimental images do not contain a scale, so that a qualitative comparison in terms of extent and spacing of cavitation structures is possible only. For $\sigma_c = 0.167$ similarities in cavitation structures can be observed between $x/\delta_{\omega,0} =$

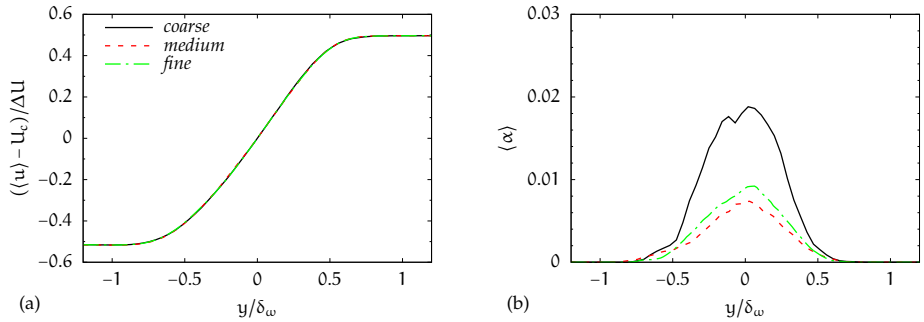

Figure 9: Grid convergence of cross-stream mean profiles for the mixing layer with $\sigma_c = 0.167$: (a) mean streamwise velocity, and (b) mean vapor volume fraction.

[100, 250] and its experimental counterpart. For further downstream positions vapor structures disintegrate and more slender vapor structures are observed at $x/\delta_{\omega,0} \approx 250$. By decreasing the cavitation number, see results for $\sigma_c = 0.1$ in Fig. 13, the large rollers related to pairing processes in the mixing layer become more occupied by vapor structures which is reproduced by the LES.

5.4.2 *Comparison of Statistical Quantities*

Fig. 14a compares the normalized streamwise evolution of the vorticity thickness between experiment [6] and LES. Normalization is performed with the vorticity thickness, $\delta_{\omega,ss}$, at the beginning of the self-similar region, x_{ss}, and the ratio of velocity difference to convective velocity, $\Delta U/U_c$. The shaded area in this and all subsequent plots marks the transition region which will not be considered in the following. The transition region cannot be expected to match since precisely defined inflow data are not provided by the experiment. The experimental data show that the growth of a mixing layer is nearly independent of the cavitation number which is reproduced by the LES. Slight differences between LES and experiment may be related to experimental difficulties in obtaining δ_ω and x_{ss} precisely. A quantitative comparison of normalized growth rates, $U_c\dot{\delta}_\omega/\Delta U$, is provided in Table 6.

Aeschlimann et al. [7] also provide data for the vapor volume fraction, $\alpha = \alpha_v$, by means of X-ray measurements, so that a quantitative comparison with LES results is possible despite uncertainties about the experimental calibration. For $\sigma_c = 0.167$, the LES reproduces clearly the maximum mean vapor volume fraction, Fig. 14b, and the cross-stream integrated mean vapor volume fraction normalized by the vorticity thickness, Fig. 14c. For $\sigma_c = 0.1$ the experimental data show a decrease in the maximum mean vapor volume fraction. The LES reproduces this trend for the evolution of the maximum mean vapor volume fraction. However, the LES predicts values that are about 30 % larger than in the experiment.

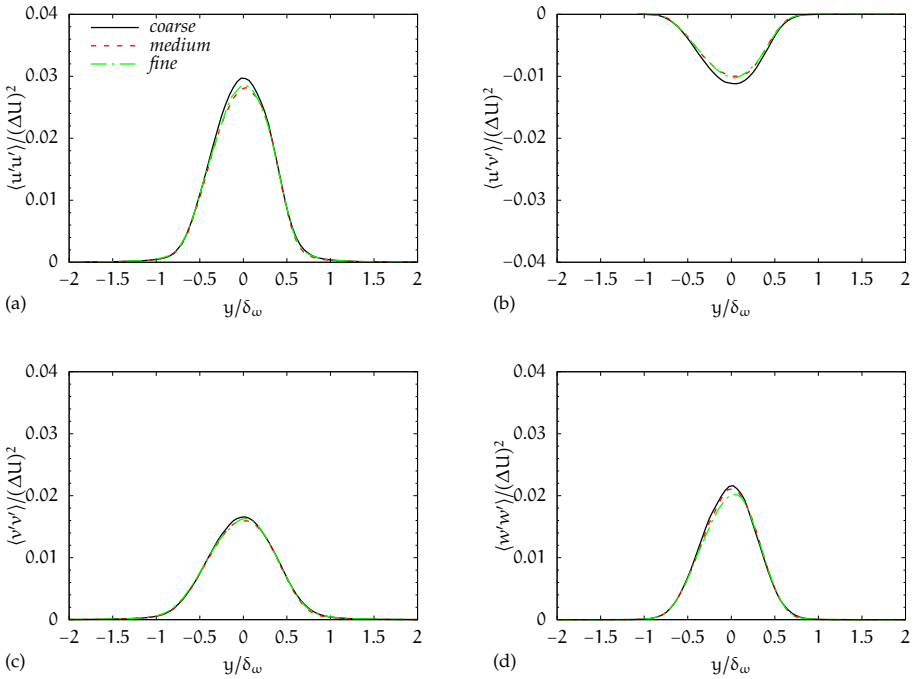

Figure 10: Grid convergence of cross-stream Reynolds stress profiles for the mixing layer with $\sigma_c = 0.167$: (a) streamwise Reynolds stress, (b) Reynolds shear stress, (c) cross-stream Reynolds stress, and (d) spanwise Reynolds stress.

Furthermore, a plateau is predicted in the LES for downstream positions $(x - x_{ss})\Delta U/(\delta_{\omega,ss} U_c) > 15$. The normalized integrated vapor volume fraction decreases significantly in the self-similar region for $\sigma_c = 0.1$ in the experiment, whereas it is approximately constant in the LES. Aeschlimann et al. [6, 7] did not provide pressure measurements along the test section but provide only the cavitation number at the end of the splitter plate. According to our experience with comparing simulation data for cavitating flows with experiments, it is well possible that the discrepancies for $\sigma_c = 0.1$ are caused by a streamwise increase of the local cavitation number leading to recondensation, e.g., due to adverse pressure gradients in the experiment. In the LES the streamwise cavitation number is constant due to the applied pressure boundary condition. For small cavitation numbers, spatial variations in the cavitation number are expected to have a larger influence since $p_\infty - p_{sat}$ is smaller.

Figs. 14d to 14f compare the streamwise evolution of Reynolds stresses with the experiment. The LES reproduces the overall trend of the experiment for the streamwise Reynolds stress, Fig. 14d, and for the Reynolds shear stress, Fig. 14e. An increase of the cross-stream Reynolds stress component for decreasing cavitation number as measured in the experiment is not reproduced by the LES, Fig. 14f. Quantitative comparison of Reynolds stresses in the self-similar region is provided in Table 6. We would like to note, however, that a quantitative comparison is difficult since measure-

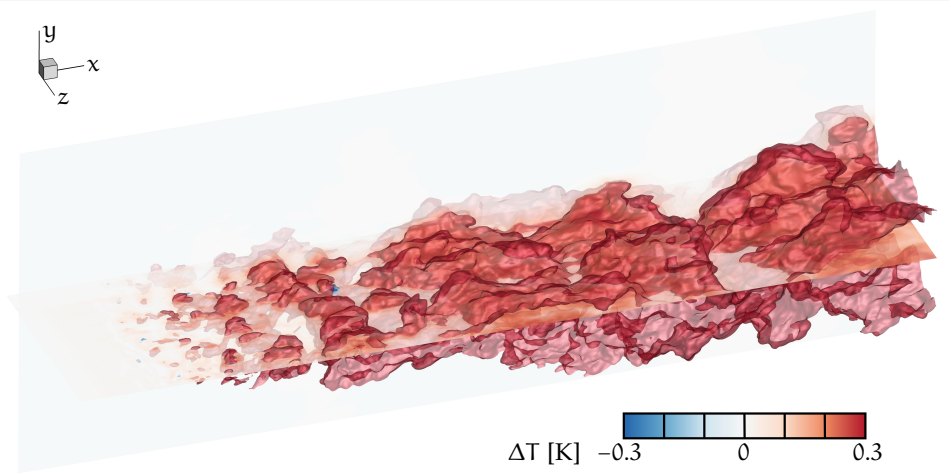

Figure 11: Instantaneous temperature difference $\Delta T = T - T_\infty$ in the mixing layer with $\sigma_c = 0.167$. The figure shows contours of ΔT on xy- and xz-planes and iso-surfaces with $\Delta T = \pm 0.1$ K (blue/red).

Table 6: Quantitative comparison of mixing layer properties between LES and experiment by Aeschlimann et al. [6, 7]. Reynolds stresses are compared at the normalized streamwise coordinate $(x - x_{ss})\Delta U/(\delta_{\omega,ss} U_c) \approx 10$.

σ_c	$\frac{U_c \dot{\delta}_\omega}{\Delta U}$		$\frac{\sqrt{\langle u'u' \rangle}}{\Delta U}$		$\frac{\sqrt{\langle v'v' \rangle}}{\Delta U}$		$\frac{\sqrt{\lvert\langle u'v' \rangle\rvert}}{\Delta U}$	
	LES	exp.	LES	exp.	LES	exp.	LES	exp.
∞	0.08	0.09	0.171	0.162	0.133	0.121	0.105	0.092
0.167	0.08	0.11	0.174	0.168	0.132	0.136	0.106	0.088
0.1	0.08	0.11	0.179	0.187	0.124	0.148	0.109	0.085

ments by PIV of fluctuating quantities in two-phase regions are subject to large uncertainties.

The normalized mean streamwise velocity profiles collapse in the self-similar region for different cavitation numbers, see Fig. 15a, and LES and experiment are in excellent agreement. Cross-stream profiles of the vapor volume fraction normalized with their respective maximum vapor volume fraction also are in good agreement with the experiment, Fig. 15b.

Overall, the comparison of our numerical approach for turbulent cavitating flows shows reasonable quantitative agreement with experimental data for the cavitating mixing layer. They also indicate that more comprehensive comparisons require much more detailed experimental information then is currently available.

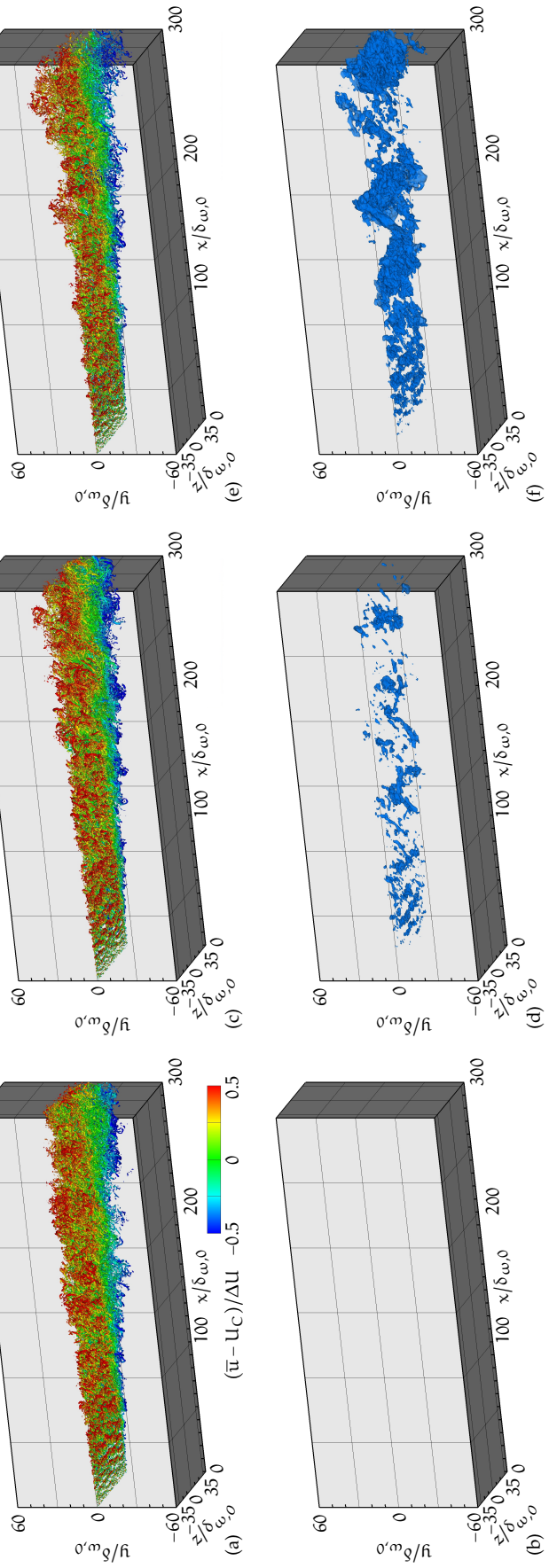

Figure 12: Instantaneous 3-D visualizations of coherent vortical and vapor structures in cavitating mixing layers. Vortical structures are identified by iso-surfaces of the λ_2 criterion [56] with normalized value $\lambda_2/(\Delta U/\delta_{\omega,0})^2 = -2000$ and are colored by the normalized streamwise velocity; vapor structures are visualized by iso-surfaces of the vapor volume fraction with $\alpha = 10$ %. (a,b) $\sigma_c = 1$, (c,d) $\sigma_c = 0.167$, and (e,f) $\sigma_c = 0.1$.

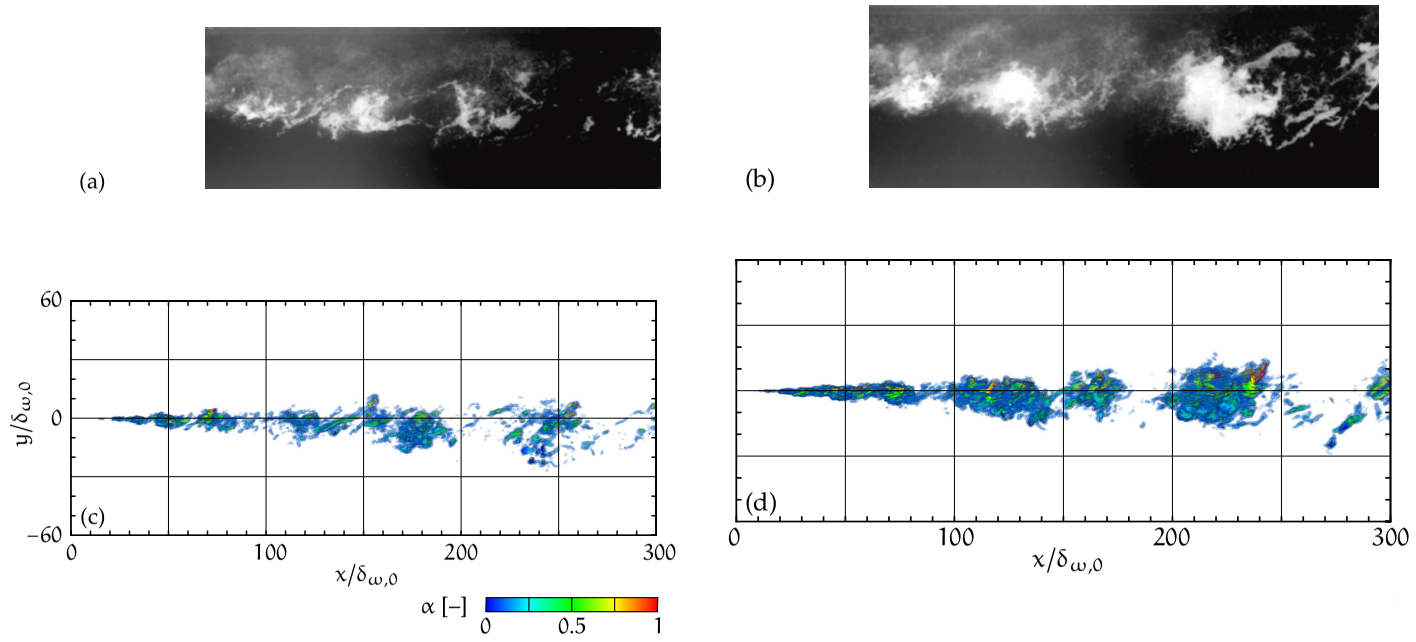

Figure 13: Qualitative comparison between experimental high-speed photographies [8] and instantaneous sideview of vapor volume fraction iso-contours from LES. Three levels of iso-contours are shown, $\alpha = [0.01, 0.1, 0.5]$, with decreasing level of transparency. (a,b) experiment, (c,d) LES; (a,c) $\sigma_c = 0.167$, (b,d) $\sigma_c = 0.1$. Note that the dimensions of the experimental images are unknown. Figures (a) and (b) are reproduced from Fig. 7(b,c) in *V. Aeschlimann, S. Prothin, S. Barre, H. Djeridi. High speed visualizations of the cavitating vortices of 2D mixing layer. European Journal of Mechanics - B/Fluids 2012; 31:171-180.*

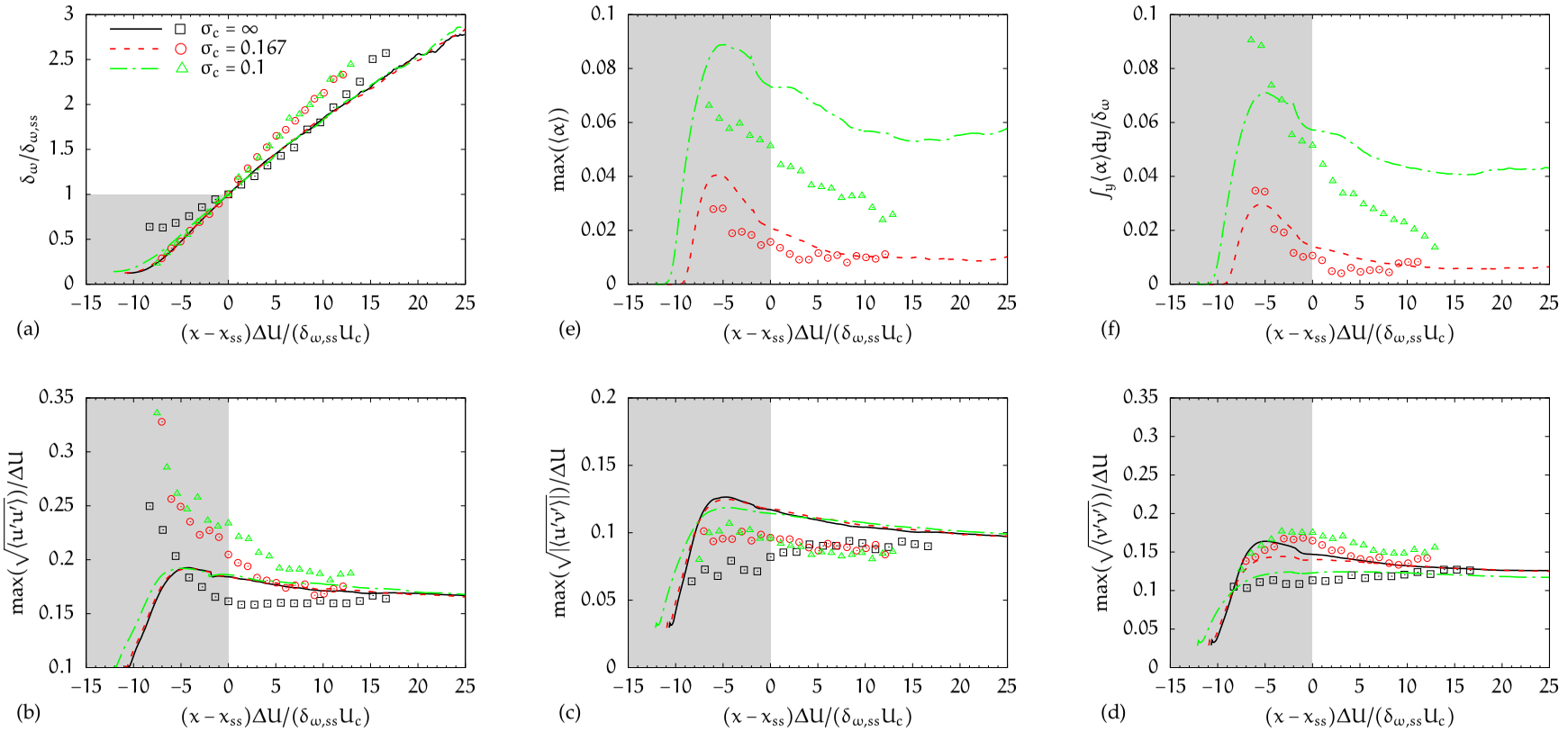

Figure 14: Comparison between LES (lines) and experiment [6, 7] (symbols). (a) Streamwise evolution of vorticity thickness; streamwise evolution of maximum cross-stream values of (b) streamwise Reynolds stress, (c) Reynolds shear-stress, (d) cross-stream Reynolds stress, (e) mean vapor volume fraction, and (f) integrated mean vapor volume fraction normalized by the vorticity thickness. $\delta_{\omega,ss}$ denotes the vorticity thickness at the begin of the self-similar region, x_{ss}. The streamwise coordinate has additionally been scaled by the ratio $\Delta U/U_c$. *Reprinted with permission from Egerer et al. [29]. Copyright 2014, AIP Publishing LLC.*

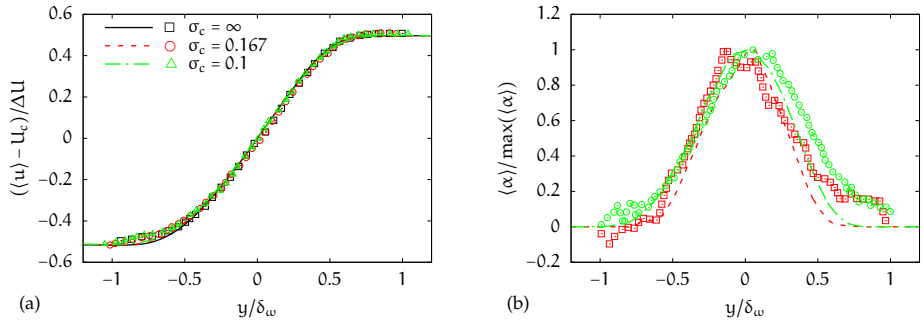

Figure 15: Comparison between LES (lines) and experiment [6, 7] (symbols) of (a) normalized velocity profiles and (b) normalized vapor volume fraction profiles in the self-similar region.

5.4.3 *Turbulence Kinetic Energy Transport Equation*

The transport equation for the resolved Turbulence Kinetic Energy (TKE), $k = \widetilde{u_i'' u_i''}/2$, reads

$$\begin{aligned} \partial_t(\overline{\rho} k) + \frac{\partial}{\partial x_k}(\overline{\rho}\widetilde{u}_k k) = \\ \overline{\rho}\left(P_{TKE} - \varepsilon_{TKE} - \varepsilon_{TKE}^{SGS}\right) - \frac{\partial T_{k,TKE}}{\partial x_k} + \Phi_{TKE} + \Pi_{TKE}, \end{aligned} \tag{55}$$

where

$$P_{TKE} = -\widetilde{u_i'' u_k''}\frac{\partial \widetilde{u}_i}{\partial x_k} \tag{56a}$$

is the turbulent production,

$$\begin{aligned} T_{k,TKE} &= T_{k,TKE}^t + T_{k,TKE}^p + T_{k,TKE}^\tau \\ &= \frac{1}{2}\overline{\rho u_i'' u_i'' u_k''} + \overline{u_k' p'} - \overline{u_i' \tau_{ik}'} \end{aligned} \tag{56b}$$

is the turbulent, pressure, and viscous transport,

$$\Phi_{TKE} = -\overline{u_i''}\left(\frac{\partial \overline{p}}{\partial x_i} - \frac{\partial \overline{\tau_{ik}}}{\partial x_k}\right) \tag{56c}$$

is the exchange due to variable inertia,

$$\Pi_{TKE} = \overline{p'\frac{\partial u_k'}{\partial x_k}} \tag{56d}$$

is the pressure dilatation, and

$$\varepsilon_{TKE} = \overline{\frac{1}{\rho}\tau_{ij}'\frac{\partial u_i'}{\partial x_j}} \tag{56e}$$

is the resolved dissipation. Contributions from SGSs are lumped together in ε^{SGS}_{TKE}.

For validation purposes we first compare TKE budgets of the single-phase, i.e., non-cavitaing case with the incompressible DNS data by Rogers & Moser [85] and the quasi-incompressible DNS data by Pantano & Sarkar [78], see Fig. 16. We generally find that extremal values in the spatially evolving mixing layer LES are larger in the high-speed stream ($y/\delta_\theta > 0$) than in the low-speed stream. Peak production, $P_{TKE}|_{max}$, is in good agreement with the DNS data of Rogers & Moser[85], while Pantano & Sarkar [78] find approx. 10 % larger values in their DNS. The values for the turbulent and pressure transport agree well between LES and DNS. While the turbulent transport, $-\partial_k T^t_{k,TKE}$, redistributes TKE from the center towards the outside of the mixing layer, the pressure transport, $-\partial_k T^p_{TKE}$, acts reversely but at a smaller rate. Exchange due to variable inertia, Φ_{TKE}, and the pressure-strain correlation, Π_{TKE}, are zero and are thus not shown in Fig. 16. The LES-grid is too coarse to resolve viscous dissipation, ε_{TKE}, so that the SGS model needs to provide the correct energy transfer. Since the mixing layer is statistically stationary, we can evaluate the contribution of the SGS model by summing all terms of the TKE transport equation. The result for ε^{SGS}_{TKE} is in excellent agreement with the viscous dissipation of the DNS, $\varepsilon_{TKE}|_{DNS}$, towards the center of the mixing layer. This shows that ALDM provides a physically correct energy transfer for this flow. We also note that some TKE is injected by the SGS model at the boundaries of the mixing layer (backscatter), say $y/\delta_\theta \approx \pm 3$.

Finally, note that for a statistically stationary and spatially evolving mixing layer, the time (local) derivative of TKE in Eq. (55) vanishes. On the other hand, for temporally evolving mixing layers, as in case of the DNS, mean convection is zero, i.e., the second term on the right-hand side of Eq. (55). Mean convection in the spatially evolving case actually corresponds to the time derivative in the temporally evolving case. As can be seen in Fig. 16b mean convection of the present non-cavitating LES is in excellent agreement with the time derivative of the incompressible DNS [85]. Pantano & Sarkar [78] do not provide data for the time derivative. The fact that mean convection is close to zero at the center of the mixing layer ($x/\delta_\theta = 0$) is another indicator for a self-similar state of the mixing layer.

Differences in TKE budgets between the non-cavitating and cavitating cases are negligible, see Fig. 17, with the exception of the pressure-dilatation correlation (56d), see Fig. 17a. For the non-cavitating case Π_{TKE} is close to zero and takes larger negative values for decreasing cavitation number. In general, Π_{TKE} may take either sign. Since it is negative for the considered cases, Π_{TKE} provides an additional path for transferring TKE to mean internal energy. Note, however, that it does not change mean entropy and is thus a reversible transfer mechanism between TKE and mean internal energy [67]. The relative importance of Π_{TKE} compared to production P_{TKE} is a natural measure of compressibility. Thus higher rates of Π_{TKE} for

decreasing cavitation numbers are not surprising since two-phase regions increase the compressibility of the fluid.

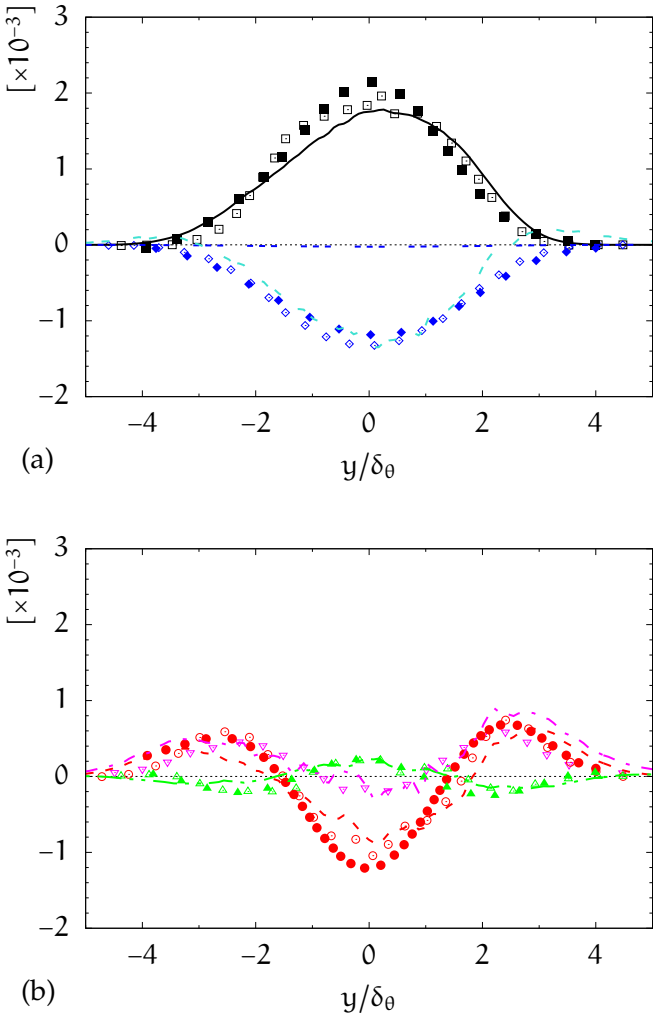

Figure 16: TKE budgets in single-phase mixing layers: comparison between non-cavitating LES (lines), incompressible DNS [85] (open symbols), and quasi-incompressible DNS [78] (filled symbols). Profiles are normalized by $(\Delta U)^3/\delta_\theta$. ——, ▫, ▪ P_{TKE}; - - - -, ○, ● $-\partial_k T^t_{k,TKE}/\overline{\rho}$; — ·· —, △, ▲ $-\partial_k T^p_{k,TKE}/\overline{\rho}$; --- ---, ◇, ◆ $-\varepsilon_{TKE}$; -- -- $-\varepsilon^{SGS}_{TKE}$. — · — $\partial_k(\overline{\rho}\widetilde{u}_k k)/\overline{\rho}$; ▽ $\partial_t k$. Note that Φ_{TKE} and Π_{TKE} are zero and not shown.

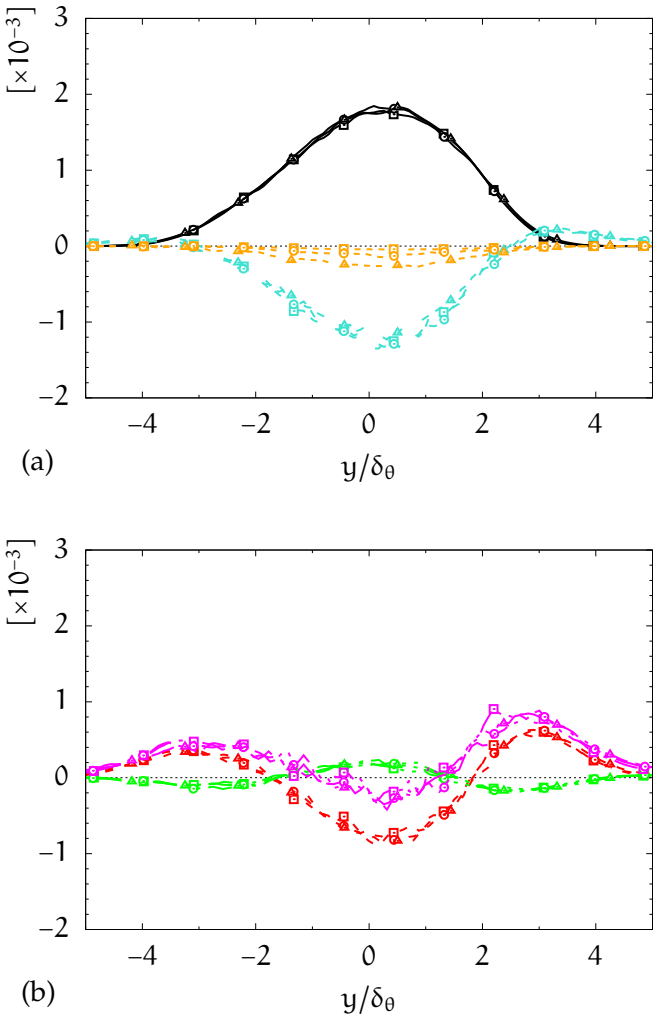

Figure 17: TKE budgets in cavitating mixing layers: comparison between mixing layer LES at different cavitation numbers. Profiles are normalized by $(\Delta U)^3/\delta_\theta$. Symbols indicate different cavitation numbers: ▫ $\sigma_c = \infty$; ∘ $\sigma_c = 0.167$; ▵ $\sigma_c = 0.1$. Line styles/colors indicate the various terms of the TKE transport equation (55): —— P_{TKE}; - - - - $-\partial_k T^t_{k,TKE}/\overline{\rho}$; — · · — $-\partial_k T^p_{k,TKE}/\overline{\rho}$; – – – – $-\varepsilon^{SGS}_{TKE}$. — · — $\partial_k(\overline{\rho}\widetilde{u}_k k)/\overline{\rho}$; - - - - - - $\Pi_{TKE}/\overline{\rho}$. Note that Φ_{TKE} and ε_{TKE} are zero and not shown.

6 APPLICATION: GENERIC MICRO CHANNEL FLOW

6.1 COMPUTATIONAL SETUP

We consider a planar throttle geometry as sketched in Fig. 18. It was designed and investigated within the European Union Research Project Experimental and CFD technology for PREVentive reduction of Diesel engine emissions caused by cavitation EROsion (PREVERO) [1]. The throttle length is $l = 1 \times 10^{-3}$ m, constant height and width are $h = W = 0.3 \times 10^{-3}$ m. It has an inlet lip with radius $R_1 = 0.04 \times 10^{-3}$ m and a sharp outlet edge. The height of the pre- and post-chamber of the throttle is $H = 3 \times 10^{-3}$ m resulting in a geometric contraction of $H/h = 10$. All dimensions specifying the computational domain are summarized in Table 7. The origin of the reference coordinate system is placed at the center of the throttle inflow plane, Fig. 18b. In the following, x denotes the streamwise, y the transverse, and z the spanwise directions.

We consider the continuous and quasi-stationary flow through the planar throttle geometry at two different operating conditions, which can be discriminated by their back pressure p_{out} as given in Table 8. Start-up processes are not considered. At operating point A (OPA), the flow is close to choking conditions; at operating point B (OPB), the flow is choked. The Reynolds number in the throttle is approximately $15 - 20 \times 10^3$ based on the height h and mean bulk velocities in the throttle.

Since the exact velocity profile in the throttle pre-chamber is unknown from the experiment, we prescribe a doubly parabolic laminar velocity profile in x-direction with bulk velocity U_B according to the operating point as inflow boundary condition at $x = -8.5 \times 10^{-3}$ m:

$$u(y,z) = \frac{9}{4} U_B \left[1 - \left(\frac{y}{H}\right)^2\right]\left[1 - \left(\frac{z}{h}\right)^2\right]. \tag{57}$$

The y- and z-velocity components are both set to zero. Since the inflow boundary is far enough upstream of the throttle, we believe that the exact shape of the inflow velocity profile has a small influence on the flow field in the throttle. The static pressure is linearly extrapolated at the inlet boundary and the density is set accordingly. At the outlet at $x =$

Table 7: Geometric dimensions of the generic throttle. *Reprinted with permission from Egerer et al. [29]. Copyright 2014, AIP Publishing LLC.*

Geometric dimension	L	l	H	h, W, R_2	R_1
Value [$\times 10^{-3}$ m]	18.0	1.0	3.0	0.3	0.04

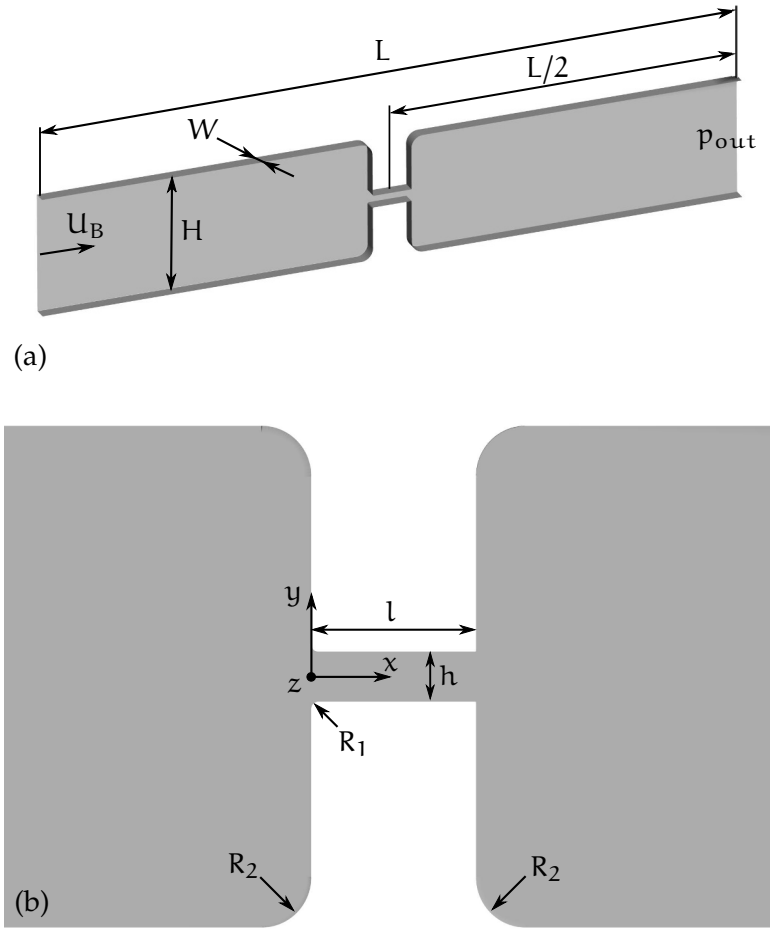

Figure 18: Geometry of the generic throttle: (a) 3-D view of the whole computational domain, (b) planar view of the throttle region with center of origin. *Reprinted with permission from Egerer et al. [29]. Copyright 2014, AIP Publishing LLC.*

Table 8: Specification of operating points A & B for the generic throttle. *Reprinted with permission from Egerer et al. [29]. Copyright 2014, AIP Publishing LLC.*

OP	$\dot{m}$ [kg/s]	U_B [m/s]	$p_{in,exp}$ [Pa]	p_{out} [Pa]	T_{ref} [K]
A	0.01450	19.310	300×10^5	115×10^5	293.15
B	0.01508	20.078		55×10^5	293.15

9.5×10^{-3} m, we set the static pressure equal to $p(y,z) = (p_{out} + p_{cd}(y,z))/2$, where p_{cd} denotes the static pressure in the last cell layer of the computational domain, in order to impose the static pressure p_{out} according to the operating point in the mean. Imposing the aforementioned arithmetic mean of static pressures reduces reflections at the outlet boundary, but still imposes p_{out} according to the operating point asymptotically. All other quantities are extrapolated linearly from the interior at the outlet boundary. A no-slip boundary condition for the velocity is employed at all walls. Initially, the velocity is set to zero in the entire computational domain. The density is initialized with $\rho = \rho(p_{out})$.

We solve the governing equations (21) on Cartesian grids. In order to account for complex geometries, we employ a second-order conservative immersed interface method [73], which has been extended to compressible flows [43, 48]. The grid is refined towards the throttle walls with a refinement ratio of 2:1 between grid blocks of different resolution. Quantities at grid block interfaces with different resolution are exchanged by a conservative interpolation procedure.

Overall computational cost is reduced by employing grid sequencing. Initially, we let the flow field develop on a coarse grid, which is sequentially refined afterwards. On intermediate grids, we advance the solution in time until a steady or periodic signal is observed for the global vapor volume fraction and the integrated mass flow across the inlet and outlet of the computational domain is equal. Fig. 19 shows the fine grid comprising roughly 30 million cells. The cell height in wall-normal direction is approx. 0.73×10^{-6} m at the lower and upper throttle walls ($y = \pm 0.5h$) and approx. 1.17×10^{-6} m at the side walls ($z = \pm 0.5W$) of the throttle. The grid is additionally refined at the intake lip of the throttle in order to account for large flow gradients in this region, cf. Figs. 19b and 19c. At walls, a maximum edge ratio of 4:1 is allowed between wall-tangential and wall-normal directions. Note that the second-order immersed interface method leads to a smooth (piecewise linear) boundary representation in cells cut by the throttle geometry unlike the zeroth-order representation used for plotting Fig. 19, where cells with negative wall distance are simply blanked.

Fig. 20 shows the wall-normal resolution in terms of wall units $h_\perp^+ = h_\perp/\delta_\mu$ for the first cell layer at the wall for both operating points. Angled brackets, $\langle\cdot\rangle$, denote Reynolds-averaged quantities. $\langle\rho_W\rangle$, $\langle\mu_W\rangle$, and $h_\perp$ denote the average density, the average dynamic viscosity, and the wall-normal cell height of the first cell at the wall, respectively. The friction velocity is $u_\tau = \sqrt{\langle\tau_W\rangle/\langle\rho_W\rangle}$ with $\langle\tau_W\rangle$ being the time-averaged wall shear stress. The viscous lengthscale is $\delta_\mu = \langle\mu_W\rangle/\langle\rho_W\rangle u_\tau$. Values of $h_\perp^+ < 5$ within the entire throttle indicate that the first off-wall grid points lie well within the viscous sublayer and justify the use of no-slip boundary conditions without employing wall-modeling. Values of $h_\parallel^+ \approx 12$ based on cell sizes in the respective wall-tangential coordinate directions result from the maximum cell aspect ratio of 4 at the wall.

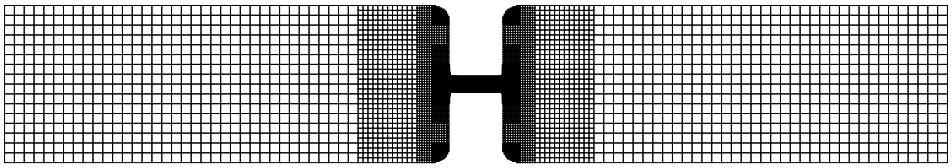

(a) Grid of the entire computational domain on a xy plane at $z = 0$.

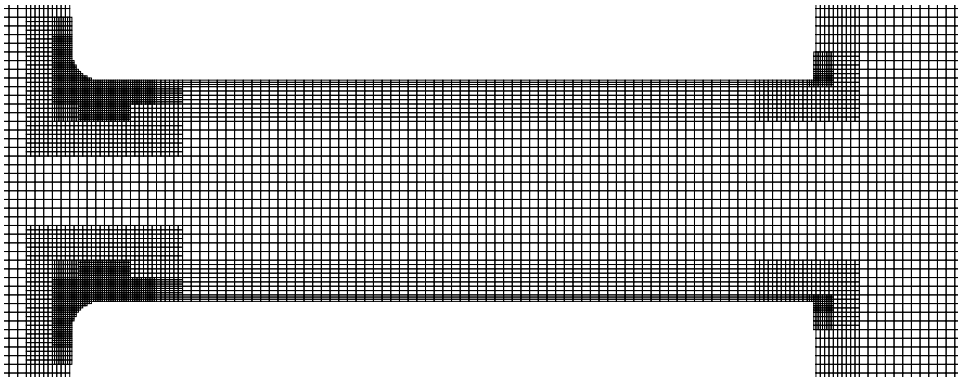

(b) Detail of the grid inside the throttle on a xy plane at $z = 0$.

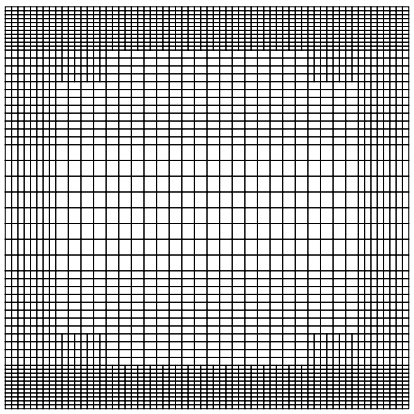

(c) Grid on a yz cross-section at $x/l = 0.1$.

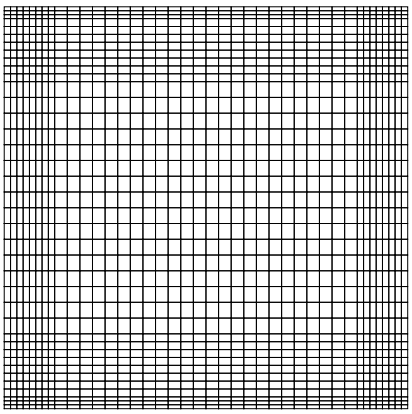

(d) Grid on a yz cross-section at $x/l = 0.5$.

Figure 19: Computational grid. Every fourth grid line of the fine grid is shown only. Cells at the immersed boundary with a negative wall distance (i.e. within the structure) are blanked. *Reprinted with permission from Egerer et al. [29]. Copyright 2014, AIP Publishing LLC.*

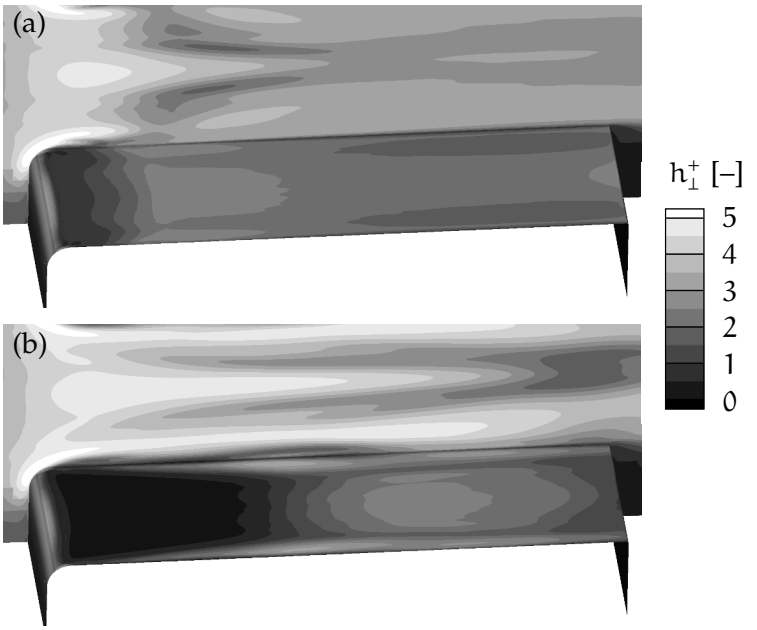

Figure 20: LES wall resolution of the first cell layer in terms of wall units $h_\perp^+$: (a) OPA, (b) OPB of the generic throttle. *Reprinted with permission from Egerer et al. [29]. Copyright 2014, AIP Publishing LLC.*

The large speed of sound of the liquid phase and the small cell sizes necessary to resolve the boundary layer lead to time-step sizes of $\tau \approx 0.14 \times 10^{-9}$ s with CFL= 0.75. On the fine grid, statistics such as mean values and Reynolds stresses are computed by sampling the flow field every ten time steps. About 4.3 million time steps are necessary to cover the analysis time interval of 0.6×10^{-3} s, which corresponds to more than 100 flow-through times of the throttle.

6.2 RESULTS AND DISCUSSION

6.2.1 *Comparison with experimental data*

Experimental set-up and measurement procedures are described in detail by Iben et al. [51]. A heat exchanger maintains the fuel at a constant temperature $T \approx T_{ref}$ during the experiments. In the experiment the pump provides a static pressure of $p_{in,exp} = 300 \times 10^5$ Pa upstream of the throttle, see Table 8. The operating point is set by adjusting the outlet pressure p_{out}. In the LES, however, we specify a volume flow rate with a bulk velocity U_B calculated from the measured mass flow rate and pressure. Consequently, the upstream pressure in the LES is not fixed *a priori* but part of the result. We find that the mean upstream pressure is approx. 6.5 % larger than the experimental value for both operating points, see Fig. 21a. Thus, the numerical simulations predict that pressure losses across the throttle due to cavitation and friction are slightly larger than in the experiment.

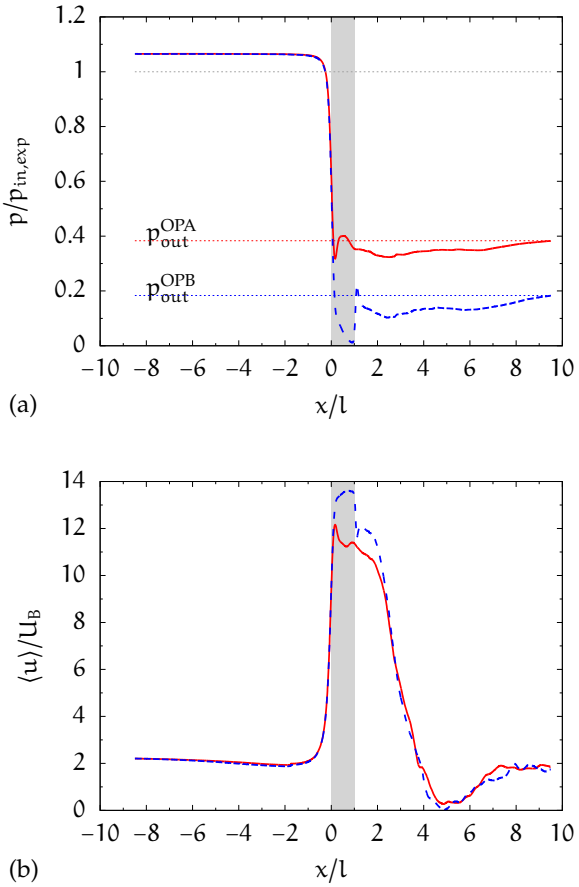

Figure 21: Comparison of (a) mean static pressure and (b) mean streamwise velocity along symmetry line, $(y, z) = (0, 0)$, of the generic micro channel: —— OPA, - - - - OPB. The gray-shaded area marks the throttle region. The upstream pressure and the downstream pressures of the experiment are marked by horizontal dotted lines.

For OPA the static pressure decreases and reaches a minimum shortly after the throttle inlet. For OPB the fluid expands further until the end of the throttle. The expansion is terminated in both cases by a sharp jump to the outlet pressure level. For OPB the jump is attached to the exit plane of the throttle being characteristic for the chocked-flow conditions. A slight subsequent expansion is obverved for both cases followed by a gradual adjustment of the pressure to outlet conditions.

The mean streamwise velocity on the symmetry line shows a similar evolution for both operating points up to the throttle inlet, see Fig. 21b. At the inlet of the computational domain $\langle u \rangle / U_B = 2.25$ due to the parabolic inflow profile (57). The geometrical contraction ratio is 10 but the actual acceleration is larger due to the additional restriction of the cross-sectional area in the throttle as a result of cavitation. Differences between the operating points are restricted to the throttle itself and one throttle length downstream of the throttle, i.e., $0 < x < 2$ in Fig. 21b.

Experimental cavitation visualizations by means of light transmission measurements of the investigated planar throttle for comparison with our LES are provided by Robert Bosch GmbH [54]. The employed Nd:YAG laser allows for an exposure time of 5 ns. This short exposure time gives almost instantaneous depth-averaged visualizations of cavitation structures and corresponds to averaging about 36 time steps in the LES. Cavitation structures and throttle geometry are visible as black areas in the light transmission images. However, no quantitative information about the vapor volume fraction can be drawn from the experiments, as the dependence of the transmitted light on the cavitation density is not known, and also no experimental calibration was attempted. Other flow features, such as turbulent structures, shear layers, or shock waves, can also be seen from the light transmission measurements due to the vignetting of their refracted light. Higher light intensities associated with these flow features allow for their discrimination from cavitation structures. A total of 100 experimental light transmission images, one taken every second, have been recorded for each operating point.

For comparison of our numerical results with the experimental images, the instantaneous vapor volume fraction field and the magnitude of the density gradient have been depth-averaged, i.e., integrated in z-direction. Since the measured intensity of the transmitted light drops to zero upon passing through a vapor region, a logarithmic scale is chosen in the numerical pictures for a better comparison of the depth-averaged vapor volume fraction $\langle\alpha\rangle_z$.

Although the continuous flow through the planar throttle is considered and is statistically stationary, the observed cavitation process inside of the throttle is highly instationary. Therefore, Fig. 22 sets three instantaneous samples of cavitation patterns observed experimentally, Figs. 22a to 22c, and three best-match time instants of cavitation structures predicted numerically, Figs. 22d to 22f(d-f), side by side for OPA. Additionally, Figs. 22g to 22i show the corresponding distribution of the depth-averaged density-gradient magnitude, $\langle|\nabla\rho|\rangle_z$. It is important to note that the state depicted in Figs. 22a and 22d is prevalent. The majority of the total of 100 experimental light transmission images shows cavitation regions at the lower and upper walls limited to approximately 20-30 % of the throttle length. Some light transmission images, such as Fig. 22b, show cavitation patterns, where a vapor cavity in a spanwise vortex has detached from the main cavitation region close to the throttle intake on the lower and/or upper throttle wall. The state observed in Fig. 22c, where a sheet-like cavity at the lower and upper throttle wall, and a vortex-like streamwise cavity above the lower sheet is visible, is found in four experimental images; less than 20 % show sheet-like cavities on the lower and upper throttle wall only.

Good agreement between experimentally observed and numerically predicted cavitation structures is found for the first state observed in the experiment, Fig. 22a, where Fig. 22d shows the numerical counterpart. The

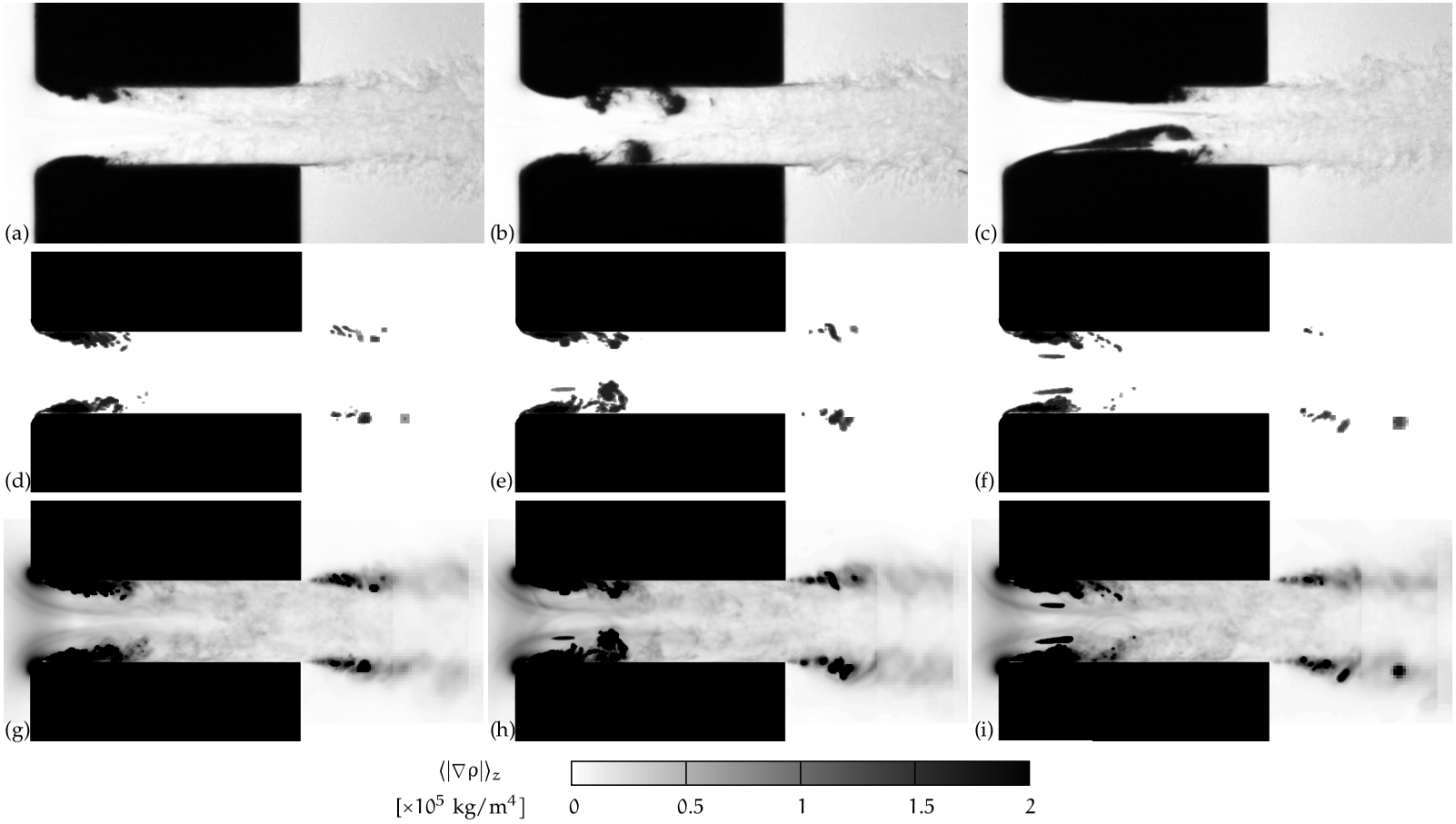

Figure 22: Comparison between experiment and LES for OPA of the generic throttle: (a-c) instantaneous experimental light transmission images; (d-f) depth-averaged vapor volume fraction $\langle\alpha\rangle_z$ (logarithmic scale with $10^{-6} \leq \langle\alpha\rangle_z \leq 0.1$), and (g-i) depth-averaged magnitude of the density gradient, $\langle|\nabla\rho|\rangle_z$, of the LES. *Reprinted with permission from Egerer et al. [29]. Copyright 2014, AIP Publishing LLC.*

streamwise extent of the cavity is especially well predicted in the LES. The same applies to the topology of the interface region between vapor and liquid. Detached spanwise cavitating vortices can also be seen in the simulations, Figs. 22b and 22e. It appears, though, that these vapor structures collapse somewhat earlier than in the experiments. The rarely observed third state in the experiment does, however, not occur during the analysis interval of the present LES. Best match is observed for a time instant when the simulation shows thin streamwise-oriented cavitation patterns above the cavity at the intake close to the wall, compare Figs. 22c and 22f. Moreover, the experiment shows intermittently a pronounced antisymmetry which is not captured by the LES. We believe that pressure pulses associated to the hydraulic environment of the experiment, or experimental variations from the nominal mass flux may cause these rare events in the experiment.

Aside from vapor structures experimental light transmission images visualize projected density fluctuations. Information about the spanwise distribution cannot be recovered. Fig. 23 shows an instantaneous snapshot of the computed magnitude of the density gradient, $|\nabla\rho|$, in two planes, one 1 % above the side wall with respect to the throttle width W, Fig. 23a, and one in the center plane at 50 % W, Fig. 23b. By comparing the two planes, one can conclude that the experimentally observed density fluctuations, Figs. 22a to 22c, in fact originate from side-wall turbulence since small-scale density fluctuations are only observed in the plane close to the side wall in the simulations, Fig. 23a. Shock waves arising from the collapse of vapor cavities propagate through the liquid and are visible in the central plane, Fig. 23b. Additionally, shear layer instabilities are observed in the central plane near the intake of the throttle. Experimental evidence of propagating shock waves and shear layer instabilities for such type of flows are given by Mauger et al. [70]. Furthermore, the comparison between the experimental images of Fig. 22 with Fig. 23a shows that the transition process is well captured by the LES. Both, experiment and LES, exhibit a wedge-like region starting at the intake lip of the throttle and attached to the lower and upper wall where small-scale density fluctuations are present. The two wedge-like regions grow towards the center of the throttle and merge at roughly 75 % of the throttle length in agreement with the experiment.

A comparison between experiment and LES for OPB is presented in Fig. 24. For this case it is sufficient to compare two experimental light transmission images with the numerical result as OPB exhibits less intense large-scale time variations than OPA. The experiment, Figs. 24a and 24b, is characterized by sheet-like cavities at the lower and upper wall of the throttle and by vortex cavitation occurring within the shear layer of the jet exiting the throttle. Intermittently, streamwise aligned vortical vapor cavities are visible in the experiment, as can be seen in Fig. 24a. The sheet-like vapor cavity as well as the vortex cavitation in the shear layer is also observed from the depth-averaged vapor volume fraction of the LES,

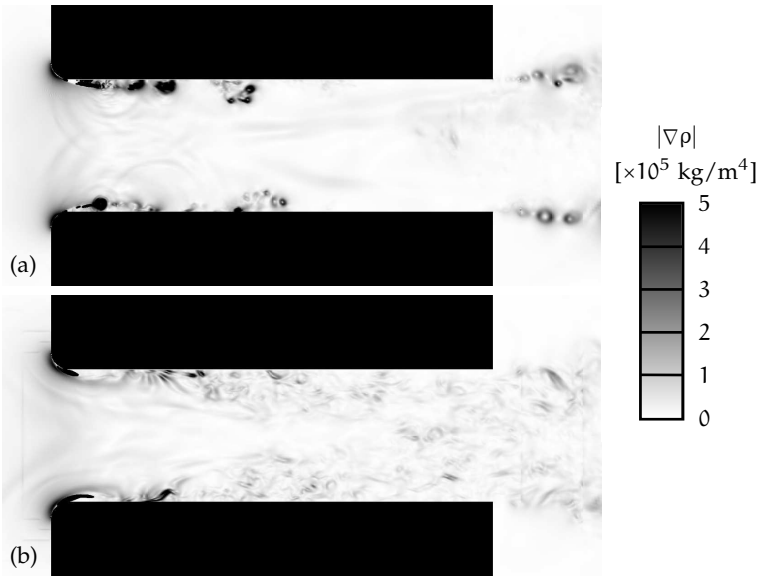

Figure 23: Instantaneous field of the LES result for the magnitude of the density gradient, $|\nabla\rho|$, in two different xy-planes for OPA of the generic throttle: (a) plane 1 % above the sidewall with respect to the throttle width W, (b) center plane between the two sidewalls. *Reprinted with permission from Egerer et al. [29]. Copyright 2014, AIP Publishing LLC.*

see Fig. 24c. The streamwise aligned vortical vapor cavities are, however, stationary in the LES and essentially symmetric to the central xz-plane. The LES reproduces the change of cavitation-structure topology of the experiment when the back pressure is reduced. Internal structures of the vapor cavities are revealed in Fig. 25, which depicts the depth-averaged magnitude of the density gradient for a single time instant at OPB. In the region between the lower and upper sheet cavity no small-scale density fluctuations are present in the experiment, which agrees with the LES.

By averaging the experimental light transmission images, a *cavitation probability* can be estimated, see Figs. 26a and 26b. We compare the cavitation probability qualitatively with the time- and depth-averaged vapor volume fraction, $\langle\langle\alpha\rangle\rangle_z$, of the LES, Figs. 26c and 26d. Although the quantitative relation between transmitted light intensity and vapor volume fraction is unknown in the experiment, it is assumed that the transmitted light intensity drops to zero as soon as 3 % vapor is in the line of sight [54]. Therefore we marked this area with a white line in the numerical images. The comparison for OPA, Figs. 26a and 26c, confirms that the LES recovers important experimental observations: the time-averaged cavitation region is limited to the first half of the throttle with the core region being restricted to the first 20-30 % of the throttle length. The cavitation probability corroborates that the first state depicted in Fig. 22a is prevalent for OPA. Differences in the vapor-region length stem from the intermittently observed third state, cf. Fig. 22c. For OPB, Figs. 26b and 26d, differences between experiment and LES arise from the cavitating vortices in the center of the throttle, as discussed before. The agreement between experimen-

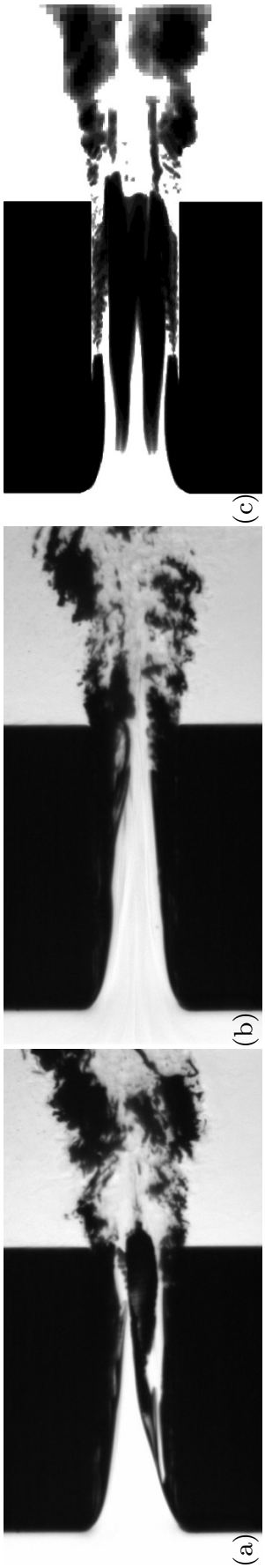

Figure 24: Comparison between experiment and LES for OPB of the generic throttle: (a,b) instantaneous experimental light transmission images; (c) contours of depth-averaged vapor volume fraction $\langle \alpha \rangle_z$ predicted numerically (logarithmic scale). *Reprinted with permission from Egerer et al. [29]. Copyright 2014, AIP Publishing LLC.*

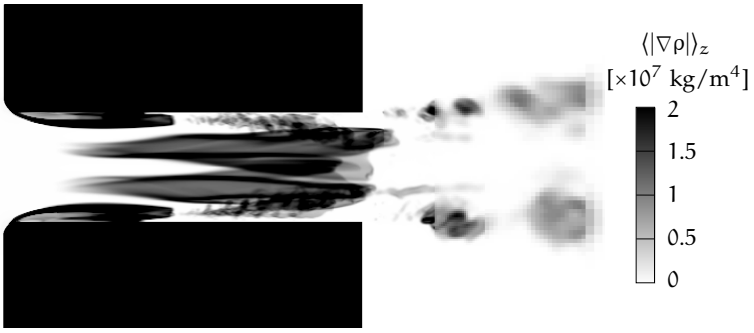

Figure 25: Instantaneous magnitude of the depth-averaged density gradient, $\langle|\nabla\rho|\rangle_z$, for OPB of the generic throttle. *Reprinted with permission from Egerer et al. [29]. Copyright 2014, AIP Publishing LLC.*

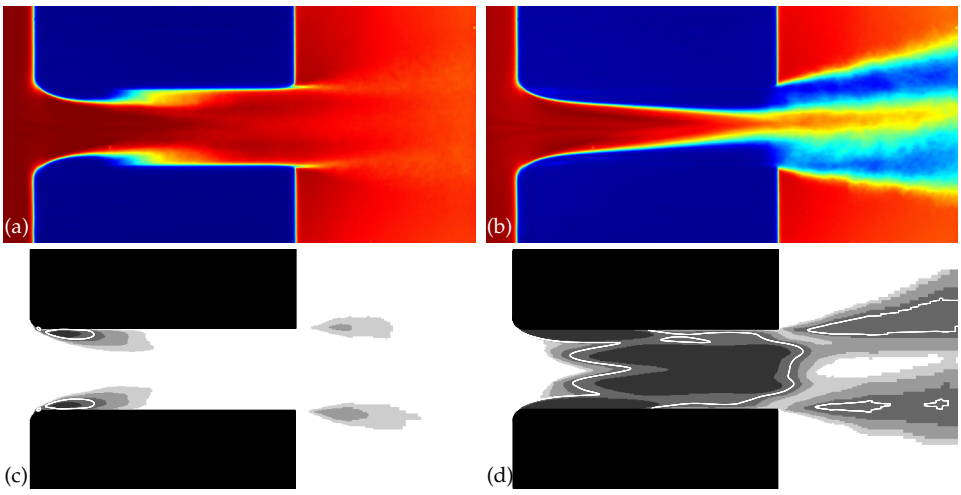

Figure 26: Experimentally derived *cavitation probability* by averaging all light transmission images for (a) OPA and (b) OPB. Time- and depth-averaged vapor volume fraction resulting from the LES for OPA (c) and OPB (d) of the generic throttle. White regions (green/yellow) delimit dark (blue) areas with an assumed vapor volume content larger than 3 % from liquid regions (red) in the experiment. Gray scale of numerical images is logarithmic with $\langle\langle\alpha\rangle\rangle_z = \{10^{-4}, 10^{-3}, 10^{-2}, 10^{-1}\}$; white lines delimit regions with $\langle\langle\alpha\rangle\rangle_z > 0.03$. *Reprinted with permission from Egerer et al. [29]. Copyright 2014, AIP Publishing LLC.*

tally and numerically observed cavitation in the shear layer of the throttle jet is very well.

Despite experimental uncertainties, we have demonstrated that the LES reproduces essential features of the experiment. Thus, the LES data field will be analyzed in more detail with respect to cavitation and flow dynamics at both operating points in the following.

6.2.2 *Coherent vortical and vapor structures*

Generally speaking, the flow topology inside of the throttle is characterized by an interaction between coherent vortical structures and different cavitation mechanisms (e.g. vortex cavitation, or inertia dominated sheet cavitation). The relative significance of the two mechanisms discriminates the two investigated operating points.

Fig. 27 shows coherent vortical structures identified by the λ_2 criterion [56] colored by the instantaneous streamwise velocity. For both operating points corner vortices originating from the boundary layer in the pre-chamber of the throttle as well as additionally created Görtler-type vortices due to the convex bend [89] are pulled into the throttle, see Fig. 27a. Due to the acceleration of the flow, the resulting streamwise velocity gradient stretches these vortices and the streamwise vorticity increases. The generation of these vortices can be explained by considering two streamlines at different wall-normal positions. Due to the boundary layer the average streamwise velocity of the streamline closer to the wall is smaller compared to the streamline further away from the wall. Thus, the centrifugal force on the streamline further away from the wall due to the convex bend is larger and forces this streamline closer to the wall. As a result of continuity, fluid closer to the wall needs to be pushed away from the wall. This effect results in the observed streamwise vortices.

At OPA the flow separates at the rounded intake lip of the throttle and creates an unsteady recirculation zone downstream, cf. Fig. 27b. The detached shear layer between the incoming downstream-directed flow and the recirculating upstream-directed flow develops Kelvin-Helmholtz instabilities and produces spanwise vortices. These vortices become unstable and streamwise oriented secondary vortices develop. Further downstream of the throttle intake, small-scale coherent structures, predominantly aligned in streamwise direction, are visible near the throttle walls. OPB, Fig. 27c, exhibits no such coherent structures in the first half of the throttle and near its walls.

Fig. 28 shows the mean streamwise vorticity, $\langle \omega_x \rangle$, in a cross-section at $x/l = 0.6$: we find two pairs of counter-rotating primary vortices, Γ_A, residing near the center and occupying large parts of the throttle cross-section for both operating points. Two secondary vortex pairs, Γ_B, are positioned closer to the sidewalls. The primary and secondary vortex pairs, Γ_A and Γ_B, exhibit larger diameters for OPB than for OPA. Both, Γ_A and Γ_B, originate from the boundary layer of the throttle pre-chamber as was

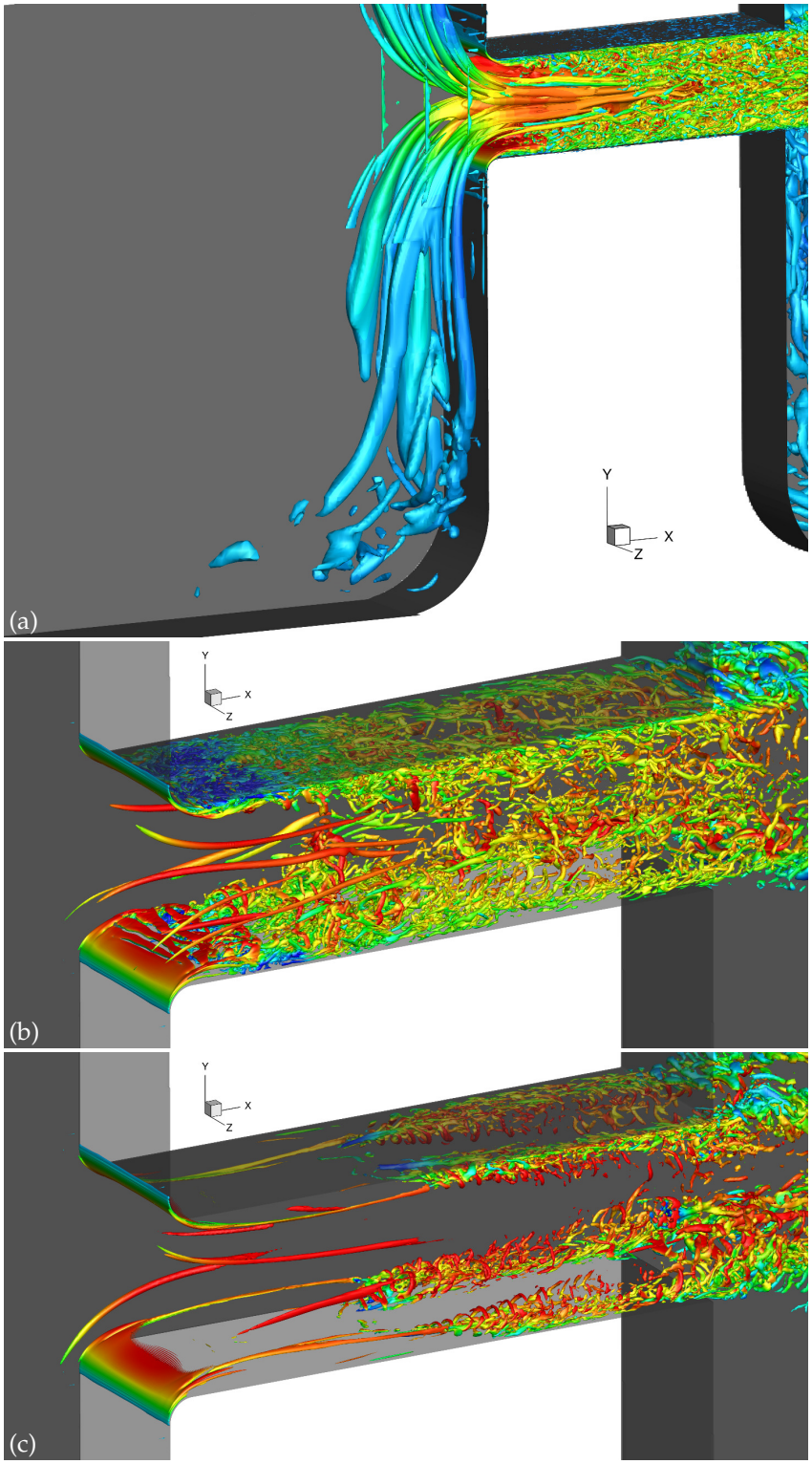

Figure 27: Coherent vortical structures in the generic throttle identified by the λ_2 criterion and colored by the instantaneous streamwise velocity (identical color scale as in Fig. 30): (a) 3-D view of the throttle pre-chamber and the throttle with $\lambda_2/(u_B/l)^2 = -12.5$. 3-D view of the throttle only with $\lambda_2/(u_B/l)^2 = -187.5$: (b) OPA, and (c) OPB. *Reprinted with permission from Egerer et al. [29]. Copyright 2014, AIP Publishing LLC.*

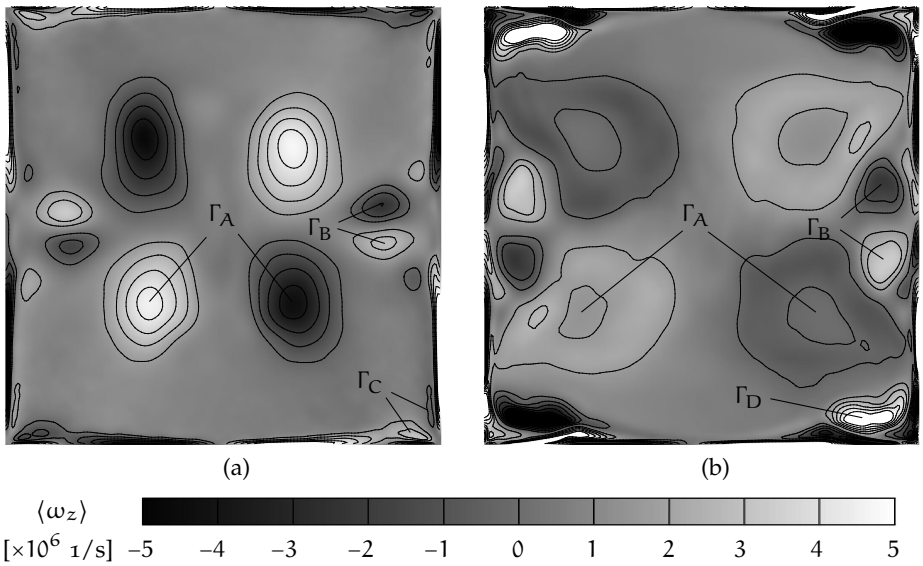

Figure 28: Comparison of streamwise mean vorticity $\langle\omega_x\rangle$ in a cross-section at $x/l = 0.6$ between (a) OPA and (b) OPB for the generic throttle. *Reprinted with permission from Egerer et al. [29]. Copyright 2014, AIP Publishing LLC.*

already discussed in Fig. 27. For OPA, Fig. 28a, we additionally observe the classical pair of counter-rotating corner vortices, Γ_C, in each quadrant of the cross-section. Their extent is reduced significantly by the existence of the primary vortices Γ_A. For OPB, Fig. 28b, only one dominant vortex, denoted with Γ_D, is located in each corner of the throttle cross-section. The vortices Γ_D break up at about 50 % of the throttle length developing secondary hairpin-like coherent structures as can be seen in Fig. 27c.

The global mean vapor volume fraction based on the full computational domain is 2.31×10^{-5} with a standard deviation of 1.02×10^{-5}. The time signal of the global vapor volume fraction at OPA exhibits a periodic signal, cf. Fig. 29a. We provide a frequency analysis of the global vapor volume fraction time signal in Fig. 29b. We compute the PSD by means of Fast Fourier Transforms (FFTs) of sub-intervals of length Δt_{FFT} with an overlap of $0.1\Delta t_{FFT}$ between sub-intervals. The sampling frequency was approx. 694 MHz. The PSD is then obtained by averaging over all sub-intervals. The sub-intervals are windowed by means of the Hanning function. Fig. 29b shows the frequency content for three different interval sizes, i.e., $\Delta t_{FFT} = \{0.1, 0.05, 0.025\}$ ms. For all interval sizes the first dominant frequency is approx $f_1 \approx 300$ kHz, Fig. 29b. For the largest Δt_{FFT} another dominant frequency $f_1' \approx 250$ kHz but with a smaller amplitude is identified. A plateau in the PSD is found at frequencies close to the first harmonic of the dominant shedding frequency $f_2 \approx 600$ kHz. The recurring cavitation process at the intake of the throttle is closely related to the unsteady recirculation zone at the throttle intake.

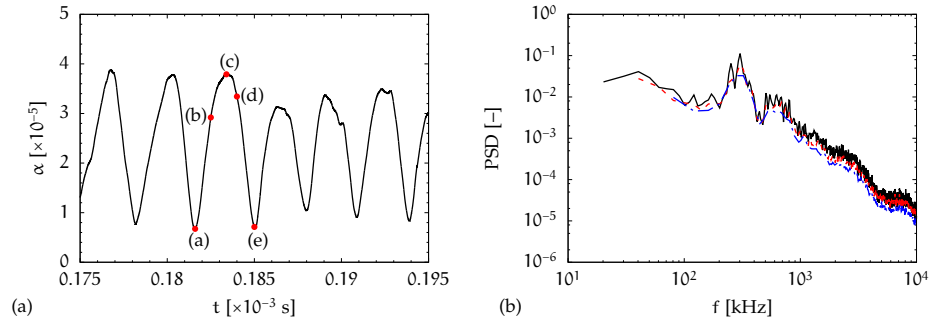

Figure 29: Global vapor volume fraction α for OPA of the generic throttle: (a) detail of time evolution and (b) frequency spectrum. PSD based on sub-intervals with —— $\Delta t_{FFT} = 0.1 \times 10^{-3}$ s, - - - - $\Delta t_{FFT} = 0.05 \times 10^{-3}$ s and – · – $\Delta t_{FFT} = 0.025 \times 10^{-3}$ s. *Reprinted with permission from Egerer et al. [29]. Copyright 2014, AIP Publishing LLC.*

One representative vapor shedding cycle is visualized in Fig. 30 by setting coherent vortical and vapor structures side by side: at the first time instant, Fig. 30a, at vapor-volume-fraction minimum the vortex sheet at the throttle intake starts to develop spanwise vortices. In the low pressure cores of these vortices evaporation occurs, increasing the global vapor volume fraction, Fig. 30b. Additionally, cavitation occurs in the cores of streamwise vortices originating from the secondary instability of the spanwise vortices. At the time instant with maximum global vapor volume fraction, Fig. 30c, the vapor regions inside of the spanwise and streamwise vortices have coalesced forming a sheet-like cavitation region. In agreement with the light transmission images, cf. Section 6.2.1, a spanwise oriented vortex cavity detaches. Subsequently, re-condensation of vapor occurs and the streamwise extent of the cavity decreases, Fig. 30d. This process is accompanied by a strong back flow at the throttle walls resulting in the reformation of the vortex sheet at the intake lip, thus initiating another shedding cycle, Fig. 30e.

Compared to OPA, the global vapor volume fraction is two orders of magnitude larger for OPB, see Fig. 31. The global mean vapor volume fraction is 1.39×10^{-3} with a standard deviation of 0.25×10^{-3}. For OPB, the time variation of the global vapor volume fraction has a smaller amplitude and frequency than at OPA. This variation is primarily related to the periodic formation of vapor in the shear layers of the jet exiting the throttle. Due to the larger pressure gradient across the throttle and the accompanied acceleration of the liquid at the throttle intake, the inertia of the liquid is large enough so that the liquid ruptures and a stable sheet cavity is created at the lower and upper throttle wall, see Fig. 32. These inertia-driven sheet cavities range from the intake to approx 50 % of the throttle length. Streamwise oriented cavitation regions in the cores of vortices Γ_D emerge out of the sheet cavities. Evaporation also occurs in their hairpin-like secondary instabilities. The pressure in the cores of the primary and secondary vortex pairs, Γ_A and Γ_B, drops below vapor pressure

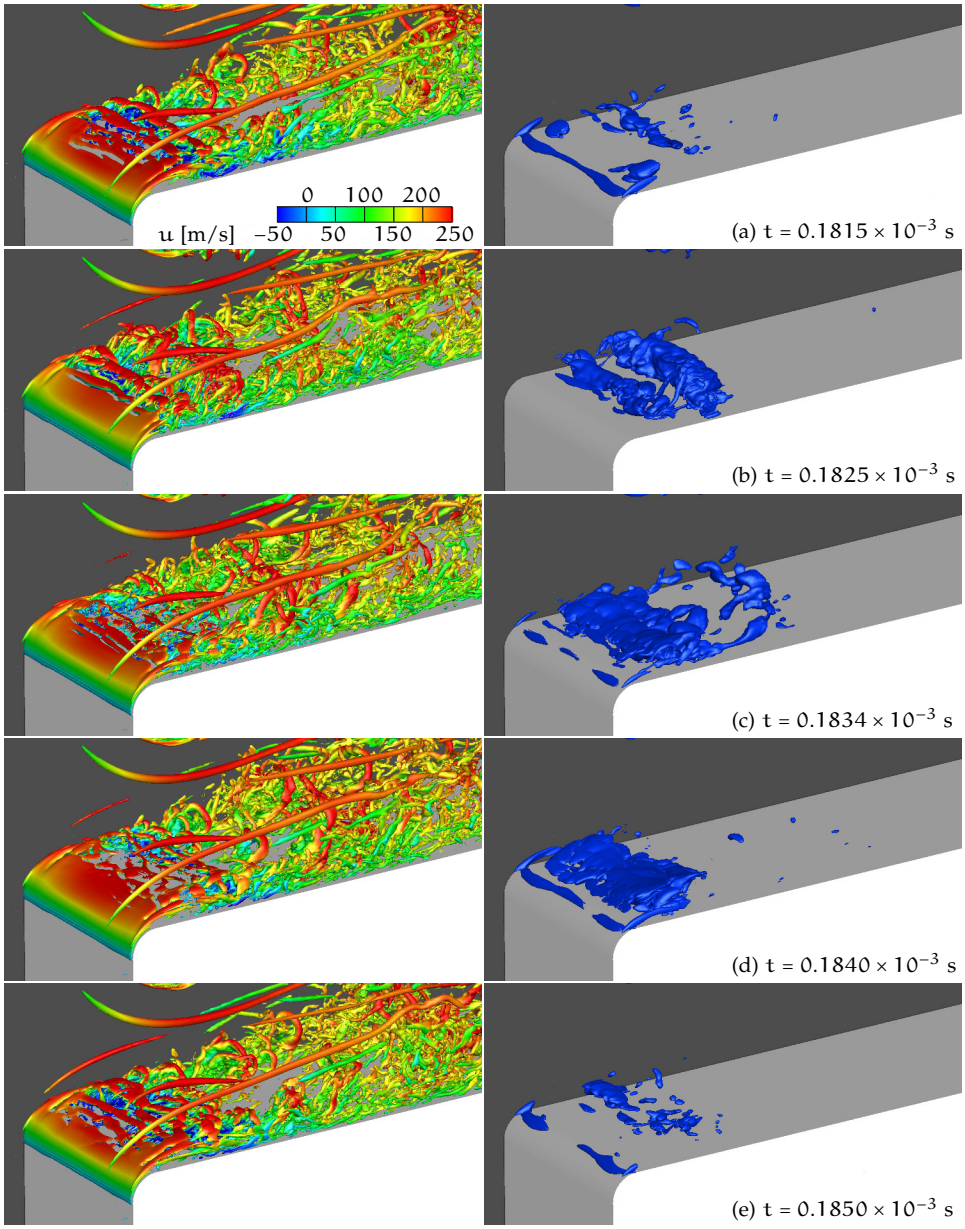

Figure 30: 3-D visualization of a representative vapor shedding cycle of OPA of the generic throttle. Time instants as marked in the global vapor volume fraction in Fig. 29a. Snapshots at same time instants of iso-contours with $\lambda_2/(U_B/l)^2 = -187.5$ colored by instantaneous streamwise velocity $\overline{u}$ (left column) and iso-contours with $\alpha = 0.1$ (right column). *Reprinted with permission from Egerer et al. [29]. Copyright 2014, AIP Publishing LLC.*

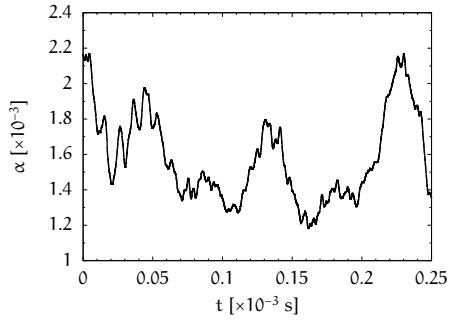

Figure 31: Time evolution of global vapor volume fraction α for OPB of the generic throttle. *Reprinted with permission from Egerer et al. [29]. Copyright 2014, AIP Publishing LLC.*

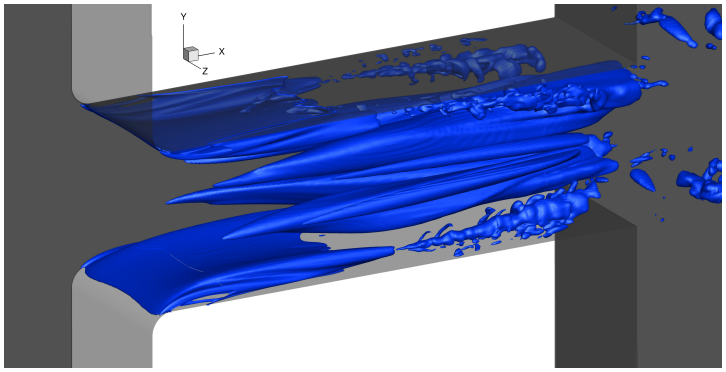

Figure 32: 3-D visualization of instantaneous iso-contours with vapor volume fraction $\alpha = 0.1$ at OPB of the generic throttle. *Reprinted with permission from Egerer et al. [29]. Copyright 2014, AIP Publishing LLC.*

leading to cavitation. Due to cavitation Γ_A and Γ_B have larger diameters for OPB than for OPA as already stated in the discussion of Fig. 28.

From visualizations of the vapor shedding cycle, Fig. 30, we conclude that the involved cavitation processes are dominated by boundary-layer flow separation and vortex dynamics for OPA. Inertia-driven cavitation processes govern the first half of the throttle flow, while vortex dynamics are important in the second half in case of OPB, see Figs. 27c and 32. The impact on boundary layer dynamics in the generic throttle is discussed in the next Section 6.2.3.

6.2.3 *Characterization of the Duct Flow*

Fig. 33 shows the spatial evolution of the skin friction coefficient $c_f = 2\langle\tau_W\rangle/\langle\rho_W\rangle U_0^2$ and the friction Reynolds number $Re_\tau = \langle\rho_W\rangle u_\tau h/2\langle\mu_W\rangle$ in streamwise direction at the lower and upper throttle walls, $(y,z) = (\pm h/2, 0)$, for both operating points. We find that the average recirculation zone for OPA extends to $x/l = 0.23$ based on the sign of the skin friction coefficient. Further downstream, skin friction coefficient as well as friction Reynolds number increase and form a plateau with $c_f \approx 0.009$ and

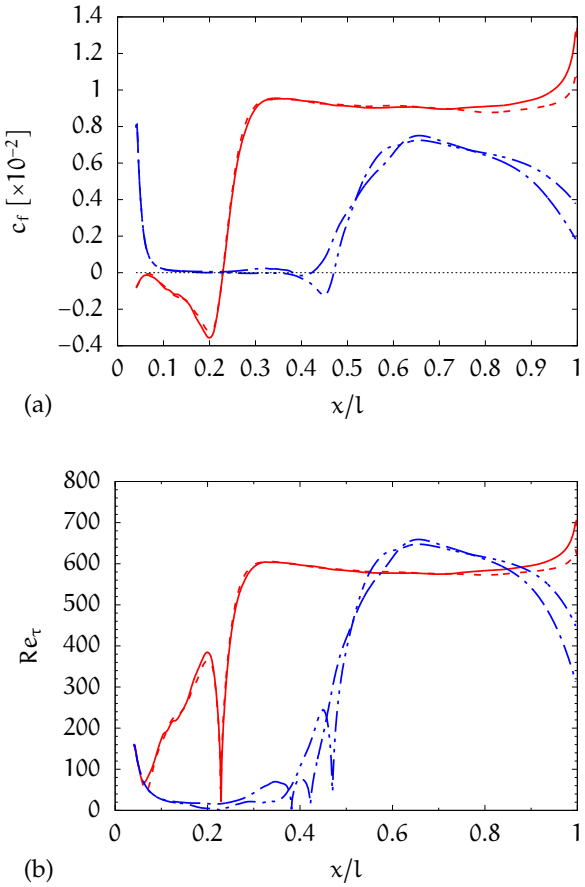

Figure 33: Comparison of streamwise evolution of (a) friction coefficient and (b) friction Reynolds number along the lower and upper wall ($y = \pm h/2$) at $z = 0$ of the generic throttle. OPA: —— $y = -h/2$, - - - - $y = +h/2$; OPB: – · – $y = -h/2$, – · · – $y = +h/2$.

$Re_\tau \approx 600$. OPB exhibits a skin friction coefficient close to zero within the sheet cavity. At the trailing edge of the sheet cavity, $x/l \approx 0.4$, we find a small recirculation zone with a slight asymmetry between upper and lower wall. Compared to OPA, c_f and Re_τ begin to rise further downstream for OPB. The skin friction coefficient remains smaller and decreases again towards the throttle exit indicating a still laminar state of the boundary layer compared to OPA.

Single-phase, fully-developed turbulent flow in *square ducts* differs from fully-developed turbulent *plane* channel flow due to secondary mean cross-flow, which interacts with the streamwise mean flow and turbulence [20, 37, 38, 50, 66]. Although typical secondary-flow velocities are of the order of a few percent of the maximum streamwise mean-flow velocity only, the secondary or mean cross-flow strongly affects average flow properties such as mean streamwise velocity and Reynolds stresses.

Fig. 34 shows wall-normal profiles of mean density and mean velocities at different streamwise and spanwise stations for OPA. The profiles have been additionally averaged across the half channel. Classical Reynolds

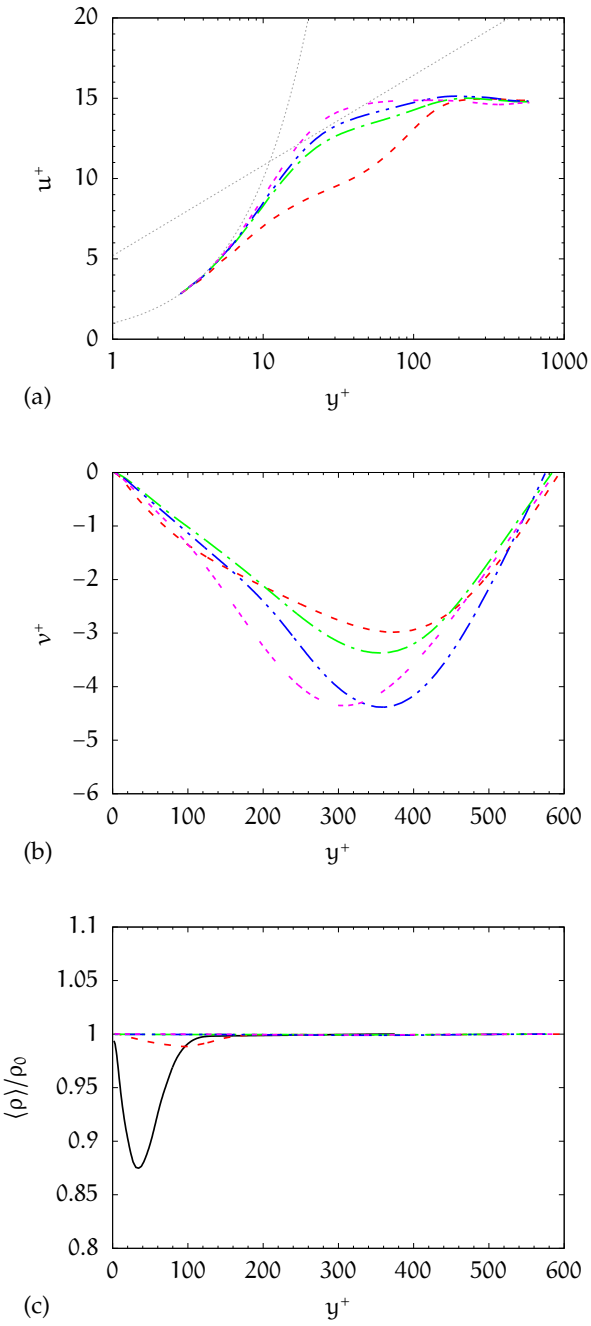

Figure 34: Streamwise variation of wall-normal profiles of (a) mean density, (b) mean streamwise velocity and (c) mean transverse velocity at $z = 0$ for OPA of the generic throttle. Mean velocities and wall distance are scaled by the local friction velocity u_τ and the local viscous lengthscale δ_μ, respectively; for the logarithmic law of the wall. The mean density is normalized by the mean density ρ_0 at the considered streamwise position on the throttle centerline. Streamwise positions are —— $x/l = 0.2$, - - - - $x/l = 0.3$, -·-·- $x/l = 0.5$, -··-··- $x/l = 0.7$, and --- --- $x/l = 0.9$. ····· viscous sublayer, $u^+ = y^+$, and logarithmic law of the wall with von Kármán constant $\kappa = 0.41$ and $B = 5.2$, $u^+ = \ln(y^+)/\kappa + B$. *Reprinted with permission from Egerer et al. [29]. Copyright 2014, AIP Publishing LLC.*

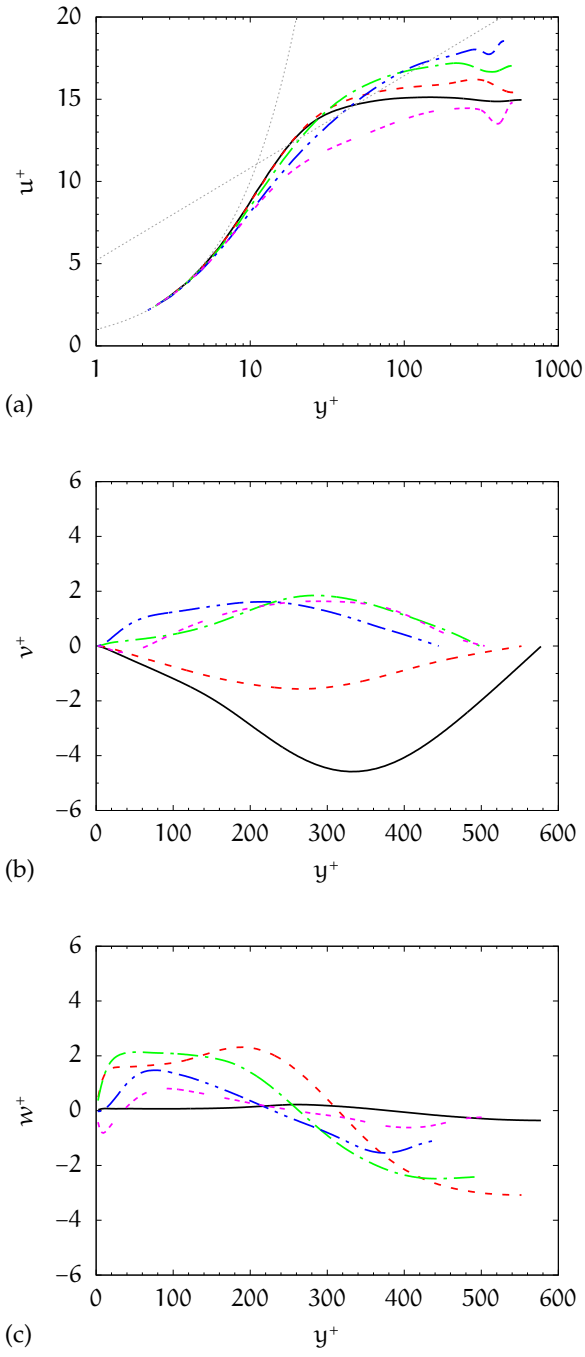

Figure 35: Spanwise variation of (a) mean streamwise velocity, (b) mean transverse velocity, and (c) mean spanwise velocity at $x/l = 0.8$ for OPA of the generic throttle. Mean velocities and wall distance are scaled by the local friction velocity u_τ and the local viscous lengthscale δ_μ, respectively; von Kármán constant $\kappa = 0.41$, $B = 5.2$ for the logarithmic law of the wall. Spanwise positions are —— $2z/W = 0$, - - - - $2z/W = 0.25$, — · — $2z/W = 0.5$, — · · — $2z/W = 0.75$, and - - - - $2z/W = 0.9$. ····· viscous sublayer, $u^+ = y^+$, and logarithmic law of the wall with von Kármán constant $\kappa = 0.41$ and $B = 5.2$, $u^+ = \ln(y^+)/\kappa + B$. *Reprinted with permission from Egerer et al. [29]. Copyright 2014, AIP Publishing LLC.*

averages have been chosen instead of Favre averages as the mean density variation is small. Even in the recirculation zone at $x/l \lesssim 0.3$ where the mean density is reduced due to cavitation it is larger than 80 % of the initial liquid density. The mean streamwise velocity deficit for $x/l \lesssim 0.3$ is caused by the recirculation zone at the throttle intake, see Fig. 34a. Further downstream, $x/l = 0.3 \ldots 0.5$, this deficit vanishes and a logarithmic layer develops but with a different slope than for an equilibrium turbulent boundary layer. Fig. 34b shows that mean cross-flow velocities have magnitudes of 10 to 30 % of the maximum mean streamwise velocity, and thus are one order of magnitude larger than observed for developed incompressible turbulent flow through square ducts [50]. The origin of mean cross-flow in developed turbulent flow through square ducts is due to different transverse and spanwise normal Reynolds stresses, $\langle v'^2 \rangle$ and $\langle w'^2 \rangle$, and the shear stress $\langle v'w' \rangle$ [20]. Mean cross-flow in the present configuration, however, is caused by vortices Γ_A and Γ_B, which have their origin in the boundary layer of the throttle pre-chamber. Moreover, mean transverse flow at the wall bisector is directed towards the lower (and upper) wall, contrary to developed turbulent flow in square ducts, and transports fluid with high streamwise momentum towards the wall. This mechanism is responsible for the lack of a logarithmic layer and for streamwise mean velocities larger than the centerline values at $y^+ \approx 60$ for sections $x/l > 0.7$, cf. Fig. 34b. This observation is similar to developed turbulent flow in square ducts [37] with the difference that the spanwise impact of the induced mean cross-flow by vortices Γ_A is reversed due to their opposite sense of rotation. This is detailed in Fig. 35a which shows mean streamwise velocity profiles at different spanwise locations at $x/l = 0.8$. A logarithmic layer, with parameters deviating from an equilibrium boundary layer, develops when moving closer to the sidewall. Mean streamwise velocity deficits in the outer layer are caused by mean cross-flow due to vortices Γ_B, see Figs. 35b and 35c.

In case of OPB, the mean density in the vapor sheet, $x/l < 0.5$, is reduced by about one order of magnitude with respect to the liquid core flow, Fig. 36c. Cavitation occurring in the vortex pair Γ_A leads to the variation in the mean density profiles for $x/l \gtrsim 0.7$. The mean streamwise velocity is close to zero with a zero wall-normal gradient in the vapor sheet, Fig. 36a, thus reducing the effective cross-section of the throttle resulting in overshoots with respect to the centerline value. Downstream of the vapor sheet, the boundary layer has to redevelop. The mean streamwise velocity shows block-shaped wall-normal profiles. The mean transverse velocity, Fig. 36b, exhibits maximum magnitudes of 10 to 20 % of the mean streamwise velocity at the centerline. We expect a similar impact on the mean streamwise velocity. Inspecting wall-normal profiles of the streamwise mean velocity for $x/l > 0.5$, we observe that the centerline value is reached close to the wall and that the overshoot disappears. Fig. 37a shows the spanwise variation of the mean streamwise velocity at $x/l = 0.8$. The cavitating vortices Γ_D transport fluid with low streamwise

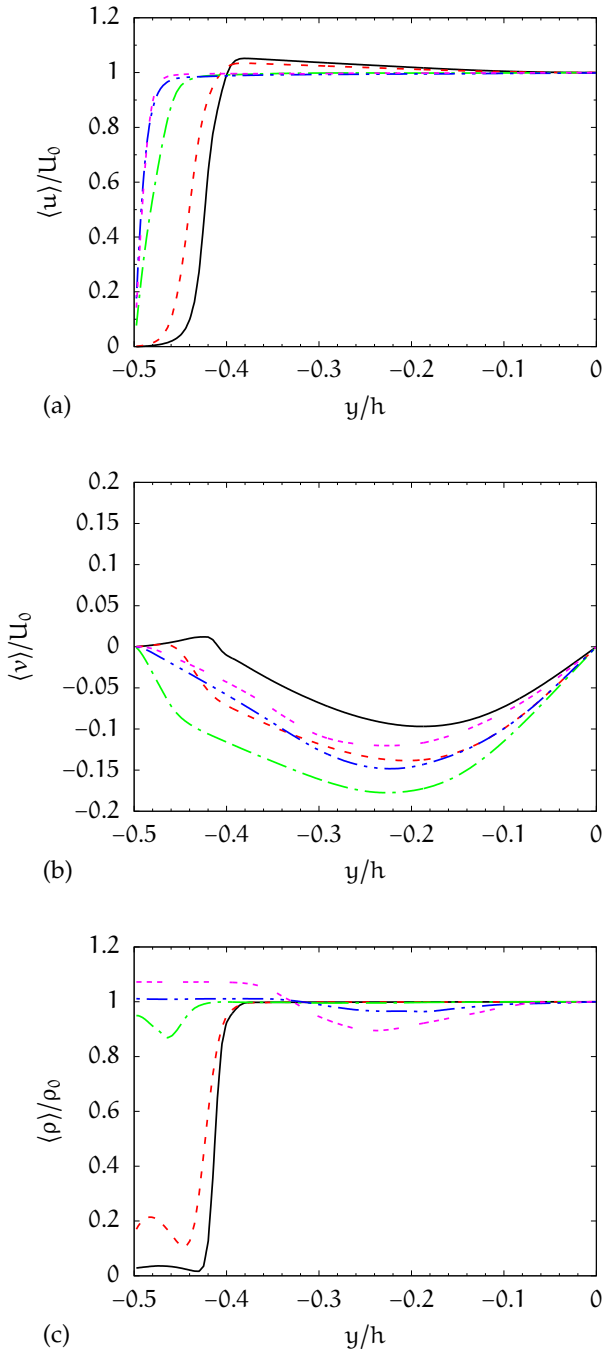

Figure 36: Wall-normal profiles of (a) mean density, (b) mean streamwise velocity and (c) mean transverse velocity at different streamwise stations at $z = 0$ for OPB of the generic throttle. Mean velocities and mean density normalized by mean streamwise velocity U_0 and mean density ρ_0 at the considered streamwise position on the throttle centerline. Wall distance normalized by throttle height h. Streamwise positions are —— $x/l = 0.2$, - - - - $x/l = 0.3$, — · — $x/l = 0.5$, – · · – $x/l = 0.7$, and - - - - - - $x/l = 0.9$. *Reprinted with permission from Egerer et al. [29]. Copyright 2014, AIP Publishing LLC.*

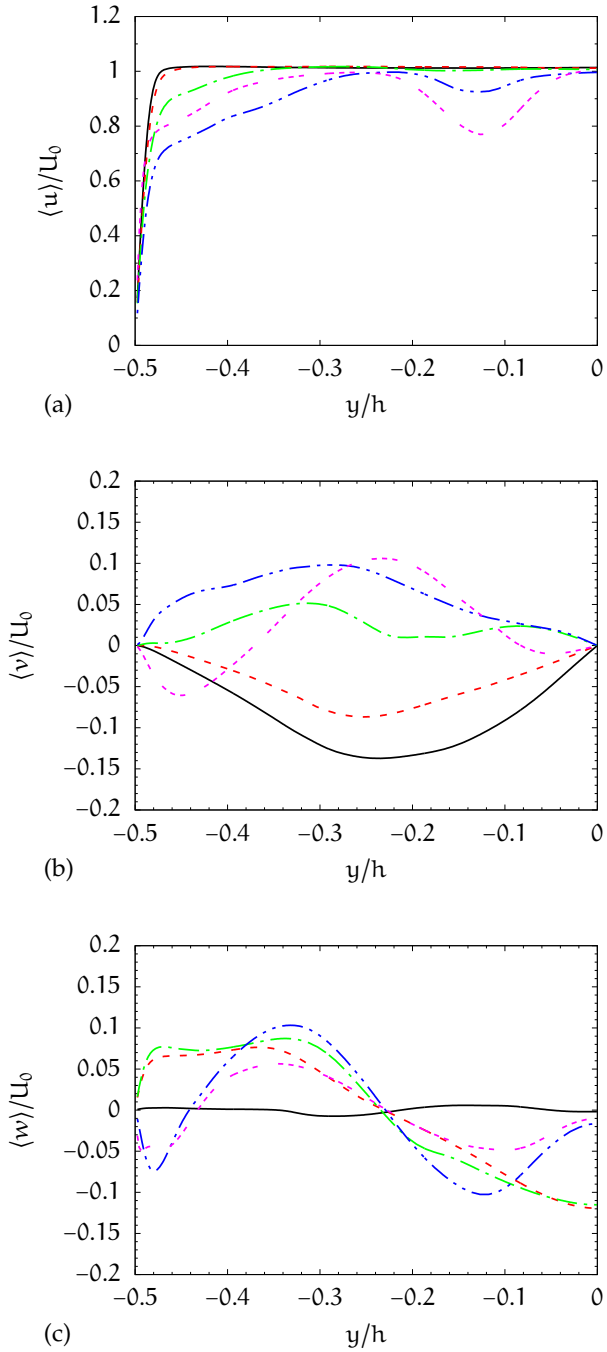

Figure 37: Spanwise variation of (a) mean streamwise velocity, (b) mean transverse velocity and (c) mean spanwise velocity profiles at $x/l = 0.8$ for OPB of the generic throttle. Mean velocities and mean density normalized by mean streamwise velocity U_0 at the considered spanwise position. Wall distance normalized by throttle height h. Spanwise positions are —— $2z/W = 0$, - - - - $2z/W = 0.25$, -·-· $2z/W = 0.5$, – ·· – $2z/W = 0.75$, and - - - - $2z/W = 0.9$. *Reprinted with permission from Egerer et al. [29]. Copyright 2014, AIP Publishing LLC.*

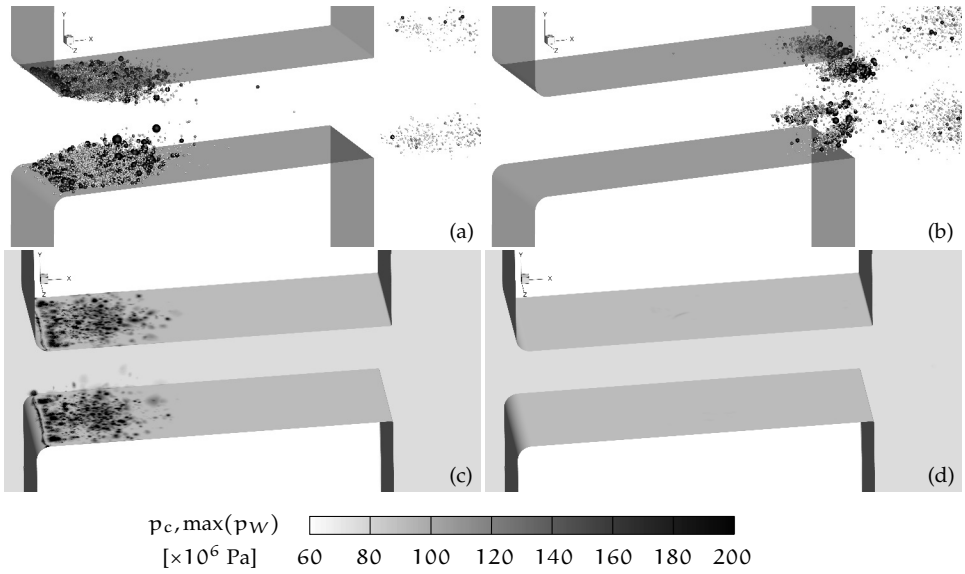

Figure 38: Prediction of cavitation erosion. Spatial distribution of isolated collapses detected during the analysis interval for (a) OPA and (b) OPB for the generic throttle. Each sphere represents a single collapse. The size and gray scale of the sphere indicates the strength of the collapse based on the normalized collapse pressure p_c. Collapses with $p_c < 60$ MPa are not shown. Maximum wall pressures p_W recorded at the throttle walls for (c) OPA and (d) OPB. *Reprinted with permission from Egerer et al. [29]. Copyright 2014, AIP Publishing LLC.*

momentum from the walls towards the center of the throttle leading to larger velocity deficits at spanwise stations closer to the sidewalls. The impact of vortex Γ_D in the cross-stream and spanwise mean velocities lead to a different behavior for OPB than for OPA close to the sidewalls at $2z/W = 0.75$ and $2z/W = 0.9$, see Figs. 37b and 37c.

6.2.4 *Cavitation Erosion*

The identification of erosion sensitive areas during the design process of fuel injectors is a key factor for optimization and safe operation. For this purpose we employ an algorithm developed by Mihatsch et al. [74], which detects isolated vapor-structure collapses (collapse detector). The collapse-detector algorithm is derived from the physics associated with the collapse of a vapor pattern: first, we mark finite-volume cells as *candidates* where the vapor volume content condenses completely during the last computed time step; second, we compute the velocity divergence for each candidate cell; during a collapse phase the divergence is negative; once it changes sign, maximum pressure of this particular collapse event is reached; third, time, location, and maximum pressure of the collapse event is recorded. Figs. 38a and 38b show the results of the collapse detector for OPA and OPB, respectively. Each sphere represents an isolated vapor collapse. Size

and gray scale of the sphere describe the strength of the detected collapse. Schmidt et al. [92] have shown that the maximum pressure of the collapse of a vapor bubble cloud depends on the grid resolution, wherefore we scale the recorded collapse pressure p_r by

$$p_c = p_r \frac{V_\Omega^{1/3}}{l_{ref}}, \tag{58}$$

where l_{ref} is a reference length scale chosen as $l_{ref} = 3.75 \times 10^{-6}$ m.

We find that the majority of collapses occur in the first half of the throttle at OPA. Strongest events are located near the intake lip and at the end of the cavitating shear layer. This observation coincides with the maximum pressures $\max(p_W)$ recorded at the throttle walls, see Fig. 38d. At OPB collapses occur only at the tails of the cavitating corner vortices close to the exit of the throttle, since other vapor structures (sheet cavity, cavitating center vortices) are stationary. Moreover, no impact of the detected collapses is measurable on the throttle walls, see Fig. 38d. Thus, based on the combined information of the collapse detector and the distribution of maximum wall pressures, we predict a significantly higher risk of cavitation erosion for OPA than for OPB.

Part III

EXTENSION OF CATUM FOR LARGE-EDDY SIMULATION OF CAVITATING FLOWS

Major parts are based on the author's journal article [30] and are reprinted with permission from Egerer et al. (2016) "Efficient implicit LES method for the simulation of turbulent cavitating flows", *Journal of Computational Phyiscs* 316: 453-469.

7 EXTENSION OF CATUM FOR LARGE-EDDY SIMULATION

7.1 CONCEPTUAL CONSIDERATIONS

ALDM relies on a six-cell stencil on Cartesian meshes, whereas CATUM operates on a four-cell stencil on structured grids, and thus is computationally cheaper. In Section 7.2.4 we will demonstrate that the spectral numerical viscosity of CATUM [97] is by one order of magnitude larger than turbulence theory requires. CATUM thus is ill-suited for LES and shares this property with nearly all classical shock-capturing schemes which are typically applied to cavitating turbulent flows. It is desirable to design a method which combines the following three favorable properties:

(1) computational efficiency,

(2) robustness for the simulation of cavitating flows, and

(3) physically consistent implicit SGS modeling properties for LES.

For this purpose, we will propose a new discretization on a four-cell stencil (property (1)). We follow the general concept of hybrid schemes [5, 63, 79], employing a switch between low-dissipation/-dispersion schemes and shock-capturing schemes based on flow sensors that detect discontinuities, e.g., shock waves, in the flow field. Thus, we confine numerical dissipation to such regions and exclude smooth parts of the flow field from excessive numerical dissipation (property (2)). Property (3) is achieved by invoking a regularization term of similar structure as proposed by ALDM [47].

7.2 DESIGN OF THE EXTENDED CATUM DISCRETIZATION SCHEME

In the following, we develop a narrow-stencil finite-volume scheme suitable for LES of compressible cavitating liquid flows. A sensor functional, see Section 7.2.3, will be introduced to switch between an upwind-biased reconstruction, which is capable of capturing discontinuities such as shock waves or pseudo phase-boundaries due to cavitation, and a formally non-dissipative central reconstruction suitable for LES of turbulent flows. A regularization term is added to the inviscid flux in order to account for the effect of unresolved SGS dynamics on the resolved scales, see Section 7.2.4.

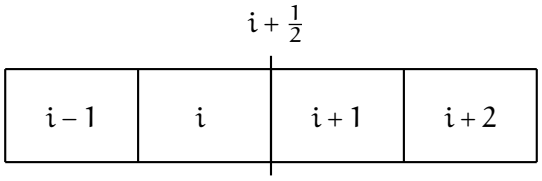

Figure 39: Nomenclature for reconstruction of cell-face values $\breve{\varphi}$ from cell-average values $\overline{\varphi}$. *Reprinted with permission from Egerer et al. [30]. Copyright 2016, Elsevier.*

7.2.1 *Baseline finite-volume scheme*

The baseline finite volume method (CATUM) solves the inviscid Euler equations, i.e., Eq. (21) with $\mathbf{D} = 0$. Considering cell face $i + 1/2$ in x-direction of an equidistant Cartesian grid, see Fig. 39, the inviscid flux of CATUM reads

$$\breve{\mathbf{C}}_{i+\frac{1}{2}} = \breve{u}^{*}_{i+\frac{1}{2}} \breve{\mathbf{Q}}^{U}_{i+\frac{1}{2}} + \breve{p}^{*}_{i+\frac{1}{2}} \begin{bmatrix} 0 \\ \mathbf{n} \\ 0 \end{bmatrix}_{i+\frac{1}{2}}, \tag{59}$$

where the vector of transported variables $\mathbf{Q}$

$$\breve{\mathbf{Q}}^{U}_{i+\frac{1}{2}} = \begin{bmatrix} \breve{\rho} \\ \breve{\rho}\breve{\mathbf{u}} \\ \breve{\rho}e + \frac{1}{2}\breve{\rho}\breve{\mathbf{u}}^2 + \breve{p} \end{bmatrix}^{U}_{i+\frac{1}{2}} \tag{60}$$

is assembled by upwind-biased reconstructions of variables ρ, $\mathbf{u}$, ρe, and p as indicated by the superscript "U". In Eq. (59), $\breve{u}^*$ denotes the transport velocity, and $\breve{p}^*$ the interface pressure.

For each quantity $\varphi = [\rho, \mathbf{u}, \rho e, p]$ we compute a left-, "−", and right-hand, "+", reconstructed cell-face value

$$\breve{\varphi}^{-}_{i+\frac{1}{2}} = \overline{\varphi}_i + \frac{1}{2}\phi\left(r^{-}_{i+\frac{1}{2}}\right)(\overline{\varphi}_i - \overline{\varphi}_{i-1}) \tag{61a}$$

and

$$\breve{\varphi}^{+}_{i+\frac{1}{2}} = \overline{\varphi}_{i+1} - \frac{1}{2}\phi\left(r^{+}_{i+\frac{1}{2}}\right)(\overline{\varphi}_{i+2} - \overline{\varphi}_{i+1}), \tag{61b}$$

where $\phi(r)$ denotes a slope limiter function that operates on the ratio of upwind to central differences

$$r^{-}_{i+\frac{1}{2}} = \frac{\overline{\varphi}_i - \overline{\varphi}_{i-1}}{\overline{\varphi}_{i+1} - \overline{\varphi}_i}, \quad \text{and} \quad r^{+}_{i+\frac{1}{2}} = \frac{\overline{\varphi}_{i+2} - \overline{\varphi}_{i+1}}{\overline{\varphi}_{i+1} - \overline{\varphi}_i}. \tag{62}$$

We employ Roe's minmod [84] slope limiter for density, internal energy and pressure

$$\phi(r) = \max\left[0, \min\left(1, r\right)\right]. \tag{63}$$

The TVD slope limiter of Koren [60], which is third-order accurate for sufficiently smooth data,

$$\phi(r) = \max\left\{0, \min\left[2r, \min\left(\frac{1}{3} + \frac{2}{3}r, 2\right)\right]\right\}, \tag{64}$$

is applied to the velocities. Based on the sign of the transport velocity, we use the left- or right-sided reconstruction, i.e.,

$$\breve{\varphi}^{U}_{i+\frac{1}{2}} = \frac{1}{2}\left[1 + \operatorname{sgn}(\breve{u}^{*}_{i+\frac{1}{2}})\right]\breve{\varphi}^{-}_{i+\frac{1}{2}} + \frac{1}{2}\left[1 - \operatorname{sgn}(\breve{u}^{*}_{i+\frac{1}{2}})\right]\breve{\varphi}^{+}_{i+\frac{1}{2}}, \tag{65}$$

in order to obtain an upwind-biased discretization.

A centered approximation of the interface pressure

$$\breve{p}^{*}_{i+\frac{1}{2}} = \frac{1}{2}\left(\breve{p}^{-}_{i+\frac{1}{2}} + \breve{p}^{+}_{i+\frac{1}{2}}\right) \tag{66}$$

ensures low-Mach-number-consistency [94].

The transport velocity is defined according to the locally linearized compatibility relations [108] and reads

$$\breve{u}^{*}_{i+\frac{1}{2}} = \frac{I^{-}\breve{u}^{-}_{i+\frac{1}{2}} + I^{+}\breve{u}^{+}_{i+\frac{1}{2}} + \breve{p}^{-}_{i+\frac{1}{2}} - \breve{p}^{+}_{i+\frac{1}{2}}}{I^{-} + I^{+}}, \tag{67}$$

where the acoustic impedances $I^{\pm}$ are defined as

$$I^{-} = \frac{1}{4}\left(3\overline{\rho}_{i} + \overline{\rho}_{i+1}\right)c_{l,\max}, \quad \text{and} \quad I^{+} = \frac{1}{4}\left(\overline{\rho}_{i} + 3\overline{\rho}_{i+1}\right)c_{l,\max}, \tag{68}$$

with $c_{l,\max} = \max(c_{l,i}, c_{l,i+1})$ being the maximum liquid speed of sound at the considered cell face.

7.2.2 *Modification of the Baseline Scheme*

Due to the intrinsic numerical dissipation of the baseline upwind-biased scheme, it is not suitable for LES, see Section 7.2.4. Therefore, we modify the reconstruction procedure for quantities $\varphi = [\rho, \mathbf{u}, \rho e, p]$ at the considered cell face

$$\breve{\varphi}_{i+\frac{1}{2}} = [1 - f(\beta)]\breve{\varphi}^{C}_{i+\frac{1}{2}} + f(\beta)\breve{\varphi}^{U}_{i+\frac{1}{2}}, \tag{69}$$

where $f(\beta) \in [0;1]$ is a sensor functional, see Section 7.2.3, and the superscript "C" indicates a central reconstruction. For assembling the vector of transported quantities $\mathbf{Q}$ we reconstruct the velocities and static pressure by a linear fourth-order central scheme

$$\breve{\varphi}^{C}_{i+\frac{1}{2}} = [\breve{u}, \breve{v}, \breve{w}, \breve{p}]^{C}_{i+\frac{1}{2}} = \frac{1}{12}\left[7(\overline{\varphi}_{i} + \overline{\varphi}_{i+1}) - \overline{\varphi}_{i-1} - \overline{\varphi}_{i+2}\right]. \tag{70}$$

In case of density and internal energy density we choose the arithmetic mean

$$\breve{\varphi}^{C}_{i+\frac{1}{2}} = [\breve{\rho}, \rho\breve{e}]^{C}_{i+\frac{1}{2}} = \frac{1}{2}\left(\breve{\varphi}^{-}_{i+\frac{1}{2}} + \breve{\varphi}^{+}_{i+\frac{1}{2}}\right) \tag{71}$$

of the left- and right-hand limited reconstructed values according to Eq. (61).

We also use the sensor functional to redefine the transport velocity

$$\begin{aligned}\breve{u}^{*}_{i+\frac{1}{2}} = [1 - f(\beta)]&\left(\breve{u}^{C}_{i+\frac{1}{2}} - \frac{\breve{\Delta^3}p_{i+\frac{1}{2}}}{I^{-} + I^{+}}\right)\\ &+ f(\beta)\left(\frac{I^{-}\breve{u}^{-}_{i+\frac{1}{2}} + I^{+}\breve{u}^{+}_{i+\frac{1}{2}} + \breve{p}^{-}_{i+\frac{1}{2}} - \breve{p}^{+}_{i+\frac{1}{2}}}{I^{-} + I^{+}}\right),\end{aligned} \tag{72}$$

where $\widetilde{\Delta^3 p}$ is a third-order accurate approximation of the pressure gradient [47], and the interface pressure

$$\breve{p}^{*}_{i+\frac{1}{2}} = [1 - f(\beta)]\,\breve{p}^{C}_{i+\frac{1}{2}} + f(\beta)\frac{1}{2}\left(\breve{p}^{-}_{i+\frac{1}{2}} + \breve{p}^{+}_{i+\frac{1}{2}}\right). \tag{73}$$

Implicit SGS modeling capability is integrated into the numerical approximation of the inviscid flux by adding a regularization term resulting in the final formulation of the inviscid flux as

$$\breve{\mathbf{C}}_{i+\frac{1}{2}} = \widetilde{u}^{*}_{i+\frac{1}{2}}\breve{\mathbf{Q}}_{i+\frac{1}{2}} + \breve{p}^{*}_{i+\frac{1}{2}}\begin{bmatrix}0\\ \mathbf{n}\\ 0\end{bmatrix}_{i+\frac{1}{2}} - [1 - f(\beta)]\,\breve{\mathbf{R}}_{i+\frac{1}{2}}, \tag{74}$$

where the vector of transported variables, $\breve{\mathbf{Q}}_{i+1/2}$, is now assembled with quantities obtained through Eqs. (69) to (71). The regularization term $\breve{\mathbf{R}}$ will be defined in Section 7.2.4.

7.2.3 *Sensor Functional*

Switching between an upwind-biased and a centered reconstruction procedure as presented in the previous section is based on a suitable sensor functional $f(\beta)$. For high-speed gas flows, Ducros' vorticity-dilatation sensor [23]

$$\beta^{\text{Ducros}} = \frac{(\nabla\cdot\overline{\mathbf{u}})^2}{(\nabla\cdot\overline{\mathbf{u}})^2 + (\nabla\times\overline{\mathbf{u}})^2 + \varepsilon} \tag{75}$$

has proven to be a simple and generally applicable way to detect shock (and expansion) waves. For cavitating flows, large density gradients at phase boundaries (material interfaces) need to be identified additionally. For predictor-corrector schemes, e.g., a sensor based on the difference of the vapor volume fraction α between grid cells was used to control characteristics-based filtering stabilization [40]. Stability for central-upwind

schemes in cavitating flows is achieved by switching to a first-order scheme as soon as $\alpha > 0$ [112]. We relax this condition and restrict the upwind-biased reconstruction to pseudo phase-boundaries by introducing a sensor based on the 3-D variation of the vapor volume fraction

$$\beta^{\alpha} = \mathrm{var}_i(\alpha) + \mathrm{var}_j(\alpha) + \mathrm{var}_k(\alpha), \tag{76}$$

where the variation in i-direction, e.g., is

$$\mathrm{var}_x = \sum_{r=0}^{1} \|\alpha_{i+r} - \alpha_{i-1+r}\|. \tag{77}$$

We do not blend continuously between reconstruction procedures, but switch from central to upwind-biased reconstruction if the Ducros shock sensor (75) or the vapor volume sensor (76) exceed a certain threshold β_{th} for at least one cell that contributes to the considered stencil, i.e.,

$$f(\beta^{\mathrm{Ducros}}, \beta^{\alpha}) = \begin{cases} 1, \text{ if } \beta^{\mathrm{Ducros}} > \beta^{\mathrm{Ducros}}_{th} \,\|\, \beta^{\alpha} > \beta^{\alpha}_{th} \\ 0, \text{ otherwise} \end{cases}. \tag{78}$$

Note that for $f = 1$ the baseline scheme as described in Section 7.2.1 is recovered. In the following, we choose $\beta^{\mathrm{Ducros}}_{th} = 0.95$ for the Ducros shock sensor and $\beta^{\alpha}_{th} = 0.25$ for the vapor volume sensor.

7.2.4 *Subgrid-scale Model*

We adopt the structure of the ALDM regularization term [47] for modelling the effect of SGS turbulence:

$$\check{\mathbf{R}} = \begin{bmatrix} \check{R}^{\rho} \\ \check{\mathbf{R}}^{\mathbf{u}} \\ \check{R}^{\rho e} \end{bmatrix} = \begin{bmatrix} \omega^{\rho} \|\Delta(\check{\mathbf{n}} \cdot \mathbf{u})\| \check{\Delta}\rho \\ \omega^{u} \check{\rho}^{C} \|\check{\Delta}u\| \check{\Delta}u \\ \omega^{v} \check{\rho}^{C} \|\check{\Delta}v\| \check{\Delta}v \\ \omega^{w} \check{\rho}^{C} \|\check{\Delta}w\| \check{\Delta}w \\ \omega^{\rho e} \|\Delta(\check{\mathbf{n}} \cdot \mathbf{u})\| \Delta(\check{\rho} e) \end{bmatrix} + \begin{bmatrix} 0 \\ \check{R}^{\rho} \check{\mathbf{u}}^{C} \\ \check{\mathbf{R}}^{\mathbf{u}} \cdot \check{\mathbf{u}}^{C} - \check{R}^{\rho} (\check{\mathbf{u}}^{C} \cdot \check{\mathbf{u}}^{C})/2 \end{bmatrix}, \tag{79}$$

where $\omega^{[\rho,\mathbf{u},\rho e]}$ are free parameters. $\check{\Delta}\varphi = \omega^{\Delta}\check{\Delta}^{1}\varphi + (1 - \omega^{\Delta})\check{\Delta}^{3}\varphi$ is a blend between a first- and a third-order approximation of the gradient of quantity φ at the cell face. Calibration of the free parameters $\omega^{[\rho,\mathbf{u},\rho e]}$ and ω^{Δ} is performed by targeting the spectral eddy viscosity for isotropic turbulence, obtained by the EDQNM [68], similarly as in [46].

Fig. 40 compares the spectral eddy viscosity of EDQNM theory with the measured spectral numerical viscosity of the original CATUM scheme, see Section 7.2.1, and the new scheme with $f(\beta) = 0$, see Section 7.2.2. Calibrated values for the free parameters of the regularization term (79) are given in Table 9. While the new scheme matches the shape and values of the spectral viscosity of EDQNM theory, see Fig. 40a, the baseline scheme exhibits a numerical dissipation which is approximately one order of magnitude larger, see Fig. 40b, rendering it unsuitable for LES.

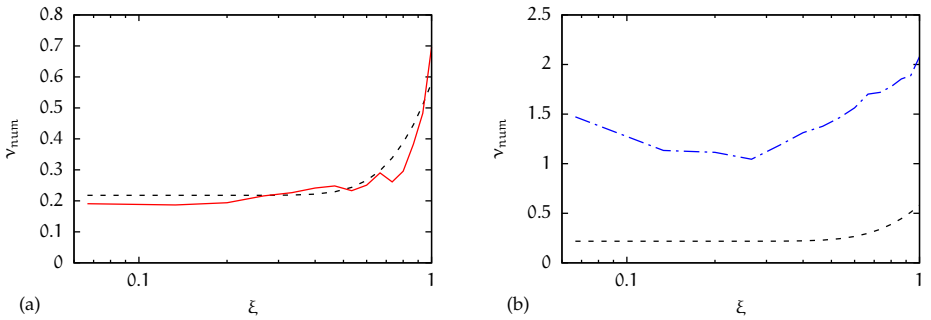

Figure 40: Comparison between measured spectral numerical viscosity of (a) the present scheme with $f(\beta) = 0$ and (b) the baseline scheme with EDQNM theory. - - - - EDQNM theory, —— present scheme, – · – baseline scheme. *Reprinted with permission from Egerer et al. [30]. Copyright 2016, Elsevier.*

Table 9: Parameters for the regularization term $\check{\mathbf{R}}$ of the proposed extension to CATUM. *Reprinted with permission from Egerer et al. [30]. Copyright 2016, Elsevier.*

ω^{ρ}, $\omega^{\rho e}$	ω^{u}, ω^{v}, ω^{w}	ω^{Δ}
0.615	0.125	0.3

8 VALIDATION OF CATUM

8.1 SHOCK TUBE PROBLEMS (IDEAL GAS)

8.1.1 *Test 1 of Toro*

As first validation test case, we consider a 1-D shock tube problem with ideal gas thermodynamics equal to Test 1 from Toro's textbook [108]. The non-dimensional initial left and right states are

$$\begin{bmatrix} \rho_L \\ u_L \\ p_L \end{bmatrix} = \begin{bmatrix} 1 \\ 0.75 \\ 1 \end{bmatrix}, \text{ and } \begin{bmatrix} \rho_R \\ u_R \\ p_R \end{bmatrix} = \begin{bmatrix} 0.125 \\ 0 \\ 0.1 \end{bmatrix}. \tag{80}$$

The grid has $N = 200$ equidistantly spaced cells and the initial interface is located at $x = 0.3$ in the domain $[0, 1]$. We use the RK2S4 scheme with CFL = 0.6 for time integration. Fig. 41 compares the solution for density, velocity, pressure, and internal energy at $t = 0.2$ obtained with the proposed scheme with the solution of a fifth-order Weighted Essentially Non-Oscillatory (WENO5) scheme [102], applied to primitive variables with Harten-Lax-van Leer-Contact (HLLC) flux function [108] (WENO5-HLLC), and with the exact solution obtained with an iterative Riemann solver. Note that WENO5-HLLC operates on a less compact six-cell stencil. The new method performs equally well as WENO5-HLLC. Numerical diffusion of the new method is slightly larger at the contact and left-going rarefaction. However, WENO5-HLLC exhibits spurious oscillations in the internal energy at the contact wave, whereas the proposed scheme is free of such oscillations. For the 1-D problem vorticity is always zero and the Ducros shock sensor marks most parts of the domain so that essentially the baseline scheme is recovered.

8.1.2 *Test 3 of Toro*

Next, we consider the more severe test case 3 of Toro's textbook [108], where the initial non-dimensional left and right states with initial interface at $x = 0.5$ in the domain $[0, 1]$ are

$$\begin{bmatrix} \rho_L \\ u_L \\ p_L \end{bmatrix} = \begin{bmatrix} 1 \\ 0 \\ 1000 \end{bmatrix}, \text{ and } \begin{bmatrix} \rho_R \\ u_R \\ p_R \end{bmatrix} = \begin{bmatrix} 1 \\ 0 \\ 0.01 \end{bmatrix}. \tag{81}$$

We compare solutions of the proposed scheme and WENO5-HLLC on a grid with $N = 200$ equidistantly spaced cells at $t = 0.012$ to the exact solution

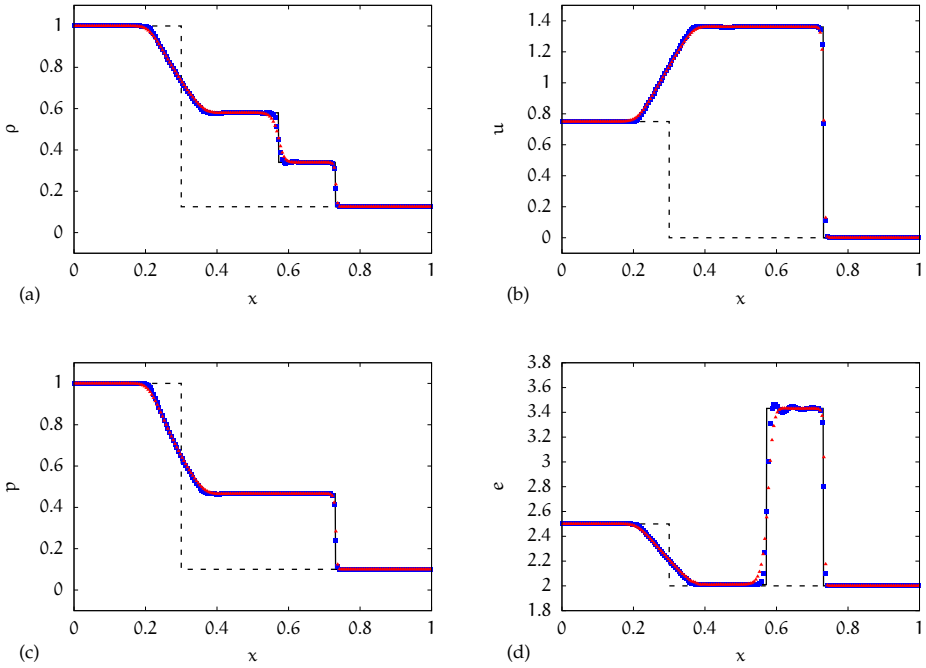

Figure 41: 1-D shock tube problem: test 1 of Toro's textbook with N = 200 cells at t = 0.2. - - - - initial condition, —— exact solution, ■ WENO5-HLLC, ▲ present scheme. *Reprinted with permission from Egerer et al. [30]. Copyright 2016, Elsevier.*

in Fig. 42. Time integration is again performed by the RK2S4 scheme with CFL = 0.6. The right-going shock wave and the left-going expansion is predicted equally well by the proposed scheme compared to WENO5-HLLC. At the beginning of the rarefaction, $x \approx 0.3$, both methods exhibit an overshoot in the velocity. As already observed for shock tube problem 1, WENO5-HLLC produces an overshoot in density at the contact wave, whereas the proposed scheme is free of spurious oscillations in this region.

8.1.3 *Double expansion in water*

A 1-D symmetric double expansion in water with initial left and right states

$$\begin{bmatrix} T_L \\ u_L \\ p_L \end{bmatrix} = \begin{bmatrix} 293.15\ \text{K} \\ -10\ \text{m/s} \\ 1\ \text{bar} \end{bmatrix}, \text{ and } \begin{bmatrix} T_R \\ u_R \\ p_R \end{bmatrix} = \begin{bmatrix} 293.15\ \text{K} \\ +10\ \text{m/s} \\ 1\ \text{bar} \end{bmatrix}, \tag{82}$$

and initial interface location at $x = 0.5$ m in the domain [0, 1m] is considered as a first test case involving cavitation. The grid consists of N = 200 equidistantly spaced cells and the solution is advanced in time with the RK2S4 method and CFL = 0.6. Fig. 43 shows density, velocity, pressure, and vapor volume fraction at $t = 0.15 \times 10^{-3}$ s. At this time instant, the left- and

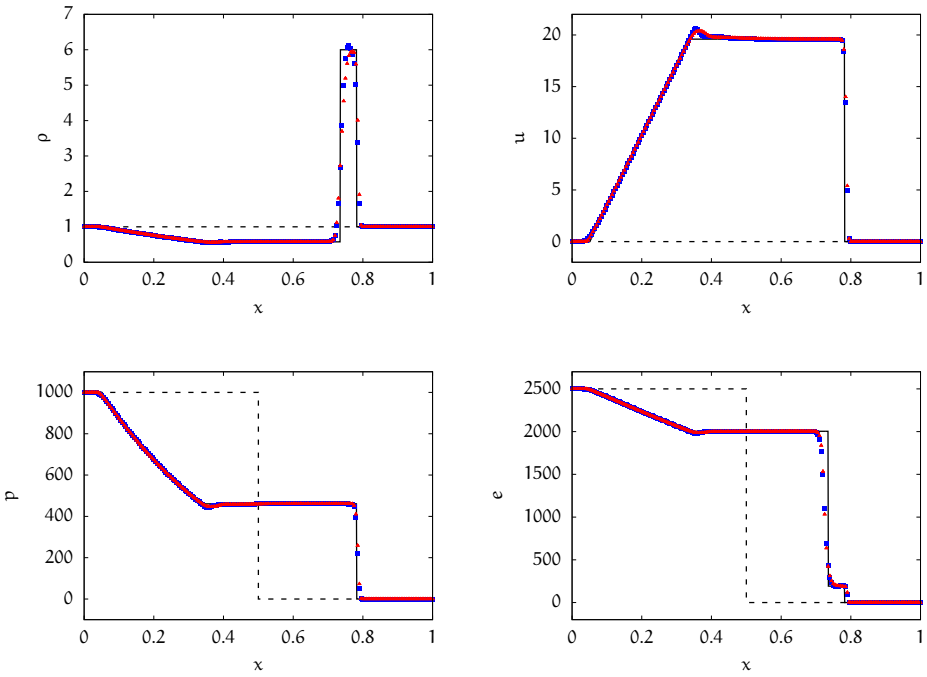

Figure 42: 1-D shock tube problem: test 3 of Toro's textbook with N = 200 cells at t = 0.012. - - - - initial condition, —— exact solution, ■ WENO5-HLLC, ▲ present scheme. *Reprinted with permission from Egerer et al. [30]. Copyright 2016, Elsevier.*

right-going expansion waves are located at $x \approx 0.25$ m and $x \approx 0.75$ m. At $x \approx 0.5$ m the pressure drops to vapor pressure p_{sat} initiating evaporation of liquid water and leading to a decrease of the mixture density. Latent heat of evaporation results in sub-cooling of the fluid at $x = 0.5$ m, see Fig. 43f. The proposed scheme reproduces the correct physical process, unlike WENO5-HLLC which exhibits a physically incorrect strong heating, see Figs. 43e and 43f.

8.2 TAYLOR-GREEN VORTEX (IDEAL GAS)

The non-dimensional initial conditions for the 3-D compressible Taylor-Green vortex are

$$\begin{aligned} \rho(\mathbf{x}, t=0) &= 1, \\ u(\mathbf{x}, t=0) &= 0, \\ v(\mathbf{x}, t=0) &= -\cos(x)\sin(y)\cos(z), \\ w(\mathbf{x}, t=0) &= \cos(x)\cos(y)\sin(z), \\ p(\mathbf{x}, t=0) &= \frac{1}{\gamma Ma^2} + \frac{1}{16}\left((\cos(2x)+2)(\cos(2y)+\cos(2z))-2\right), \end{aligned} \tag{83}$$

where $Ma = 0.1$ is chosen for all cases. The cubic, 2π-periodic domain is discretized by N^3 equally sized cells. Time integration is performed with the RK3S3 method and CFL = 0.5.

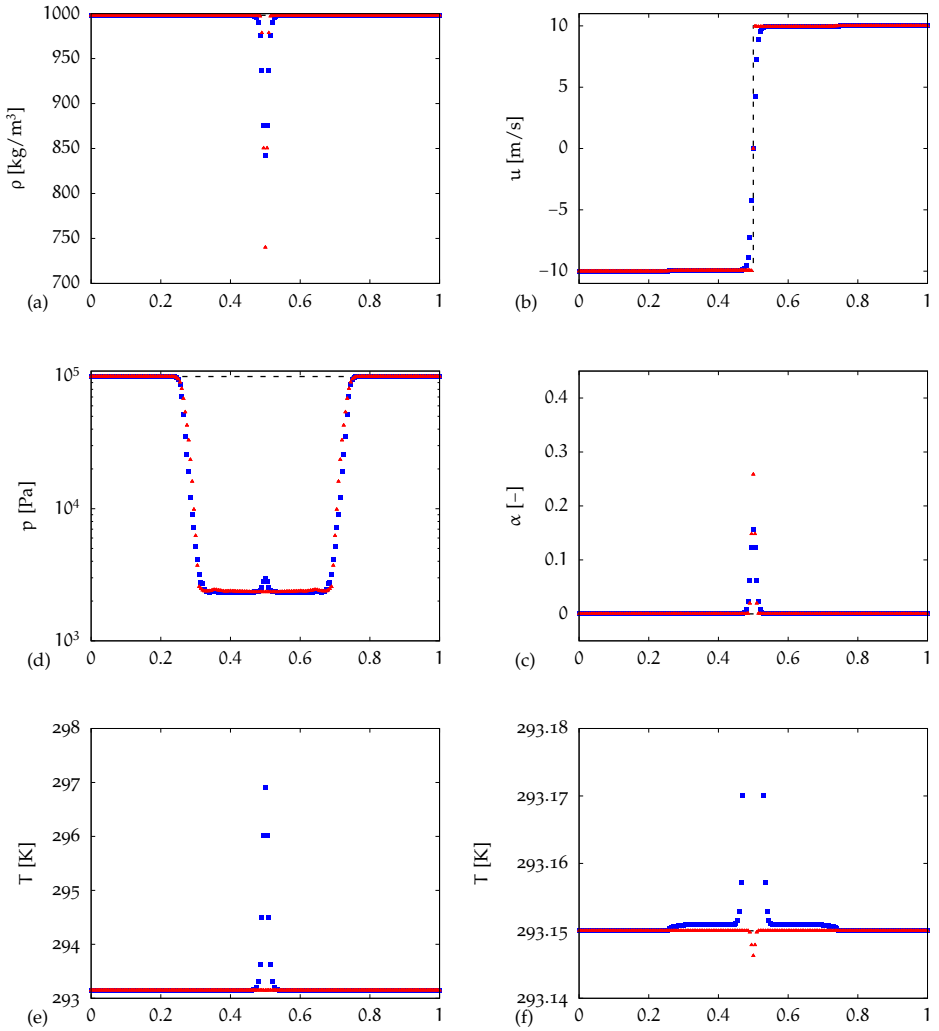

Figure 43: Cavitating double expansion test problem in water with N = 200 cells at $t = 0.15 \times 10^{-3}$ s. (f) is a zoom of (e) showing the sub-cooling of the fluid due to cavitation. - - - - initial condition, ■ WENO5-HLLC, ▲ present scheme. *Reprinted with permission from Egerer et al. [30]. Copyright 2016, Elsevier.*

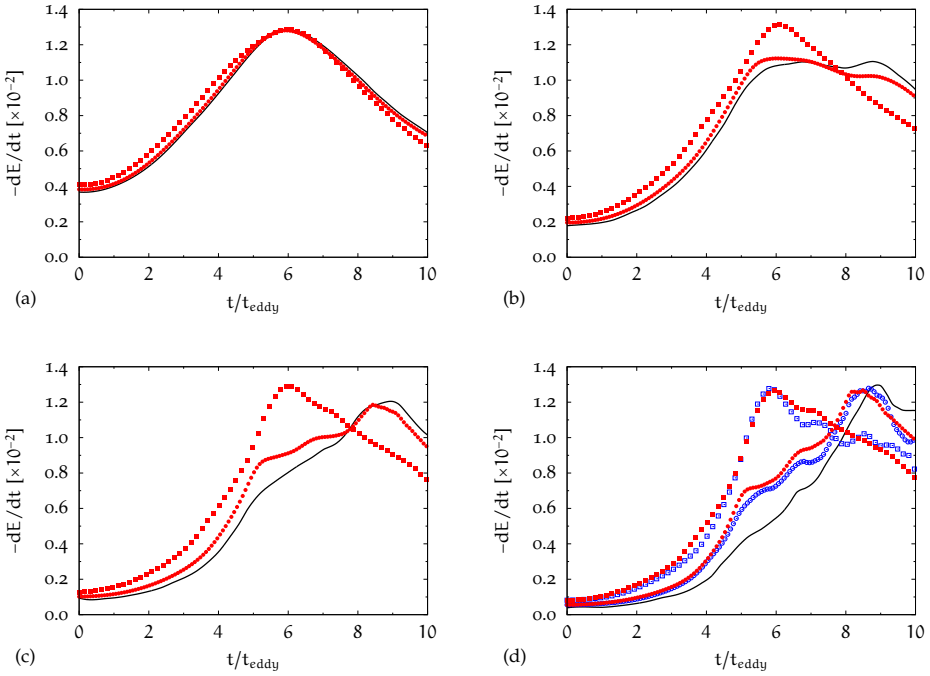

Figure 44: Comparison of energy decay rates between implicit LES with the proposed scheme and reference DNS of the compressible Taylor-Green vortex at different Reynolds numbers: (a) Re = 200, (b) Re = 400, (c) Re = 800, and (d) Re = 1600. For Re = 1600 a comparison with ALDM is provided additionally. —— reference DNS, ▪ proposed scheme with N = 32, • proposed scheme with N = 64, ▫ ALDM with N = 32, ○ ALDM with N = 64. *Reprinted with permission from Egerer et al. [30]. Copyright 2016, Elsevier.*

Fig. 44 compares the energy decay rates of implicit LES with the present scheme at two resolutions (N = 32 and N = 64) to a reference DNS of the compressible Taylor-Green vortex at different Reynolds numbers for 10 large-eddy turnover times. We note that with increasing resolution the solution of the proposed scheme approaches the DNS result. For Re = 1600, Fig. 44(d), we additionally compare our results with a state-of-the-art implicit LES method ALDM [47]. We observe a similar evolution for both schemes. The energy decay rate is slightly larger at times $4 < t < 7$ for the proposed scheme than for ALDM. Overall the proposed scheme is similarly effective as ALDM, which has been shown to be clearly superior to the dynamic Smagorinsky model [46].

8.3 DECAYING COMPRESSIBLE ISOTROPIC TURBULENCE (IDEAL GAS)

Suitability of the present method for turbulent flows is validated with canonical decaying compressible isotropic turbulence in a 2π-periodic box.

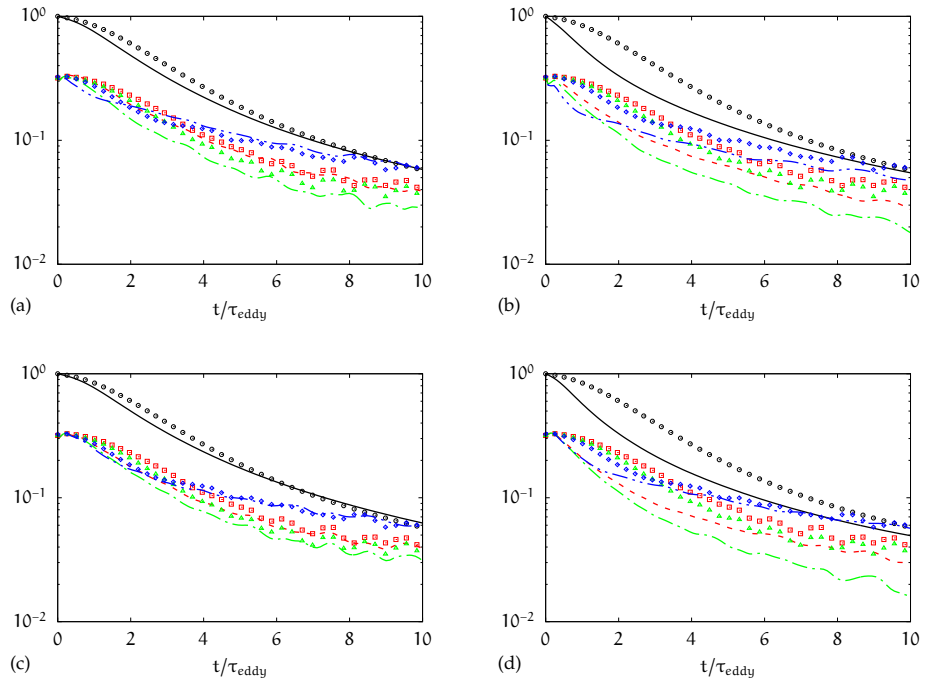

Figure 45: Global statistics over ten large-eddy turnover times for decaying compressible isotropic turbulence with $Re_\lambda = 100$ and $Ma_t = 0.3$. Comparison between LESs (lines) on a grid with $N^3 = 32^3$ cells and DNS data [47] (symbols): (a) proposed method, (b) baseline scheme, (c) ALDM, and (d) WENO5-HLLC without explicit SGS model. Quantities: —— , ∘ $\langle u_i'^2\rangle/2$, - - - - ▫ $\langle \rho'^2\rangle$, —·— △ $\langle p'^2\rangle$, and —·— ◇ $\langle p'^2\rangle$. *Reprinted with permission from Egerer et al. [30]. Copyright 2016, Elsevier.*

The initial random velocity field is characterized by the following prescribed spectrum for turbulence kinetic energy

$$\hat{k}(\xi) = \xi^4 \exp(-2\xi^2/\xi_0^2) \tag{84}$$

with peak-energy wavenumber $\xi_0 = 4$. The initial Taylor length-scale is $\lambda = 2/\xi_0$ resulting in an initial Reynolds number based on the Taylor length-scale of $Re_\lambda = \langle\rho\rangle u_{ref}\lambda/\langle\mu\rangle = 100$. The reference velocity is $u_{ref} = \sqrt{\langle \mathbf{u}'^2\rangle/3}$ based on initial velocity fluctuations. The initial turbulent Mach number is $Ma_t = \sqrt{\langle \mathbf{u}'^2\rangle}/\langle c\rangle = 0.3$. Note that angled brackets mark Reynolds averages in the following. Consistent initial data for density, velocity dilatation, and total energy are obtained by the method of Ristorcelli and Blaisdell [83]. The cubic computational domain is discretized with $N^3 = 32^3$ cells. The time step is controlled by choosing CFL = 0.5 for the RK3S3 time integration scheme.

Fig. 45 shows the time evolution of turbulence kinetic energy and thermodynamic variances over ten large-eddy turnover times $\tau_{eddy} = 2/(\xi_0 u_{ref}^2)$. The decay rates for the baseline scheme, Fig. 45b, are too large compared to DNS data [47] especially at early times. The new method shows significantly better results for all quantities, Fig. 45a. Comparison of spectra at

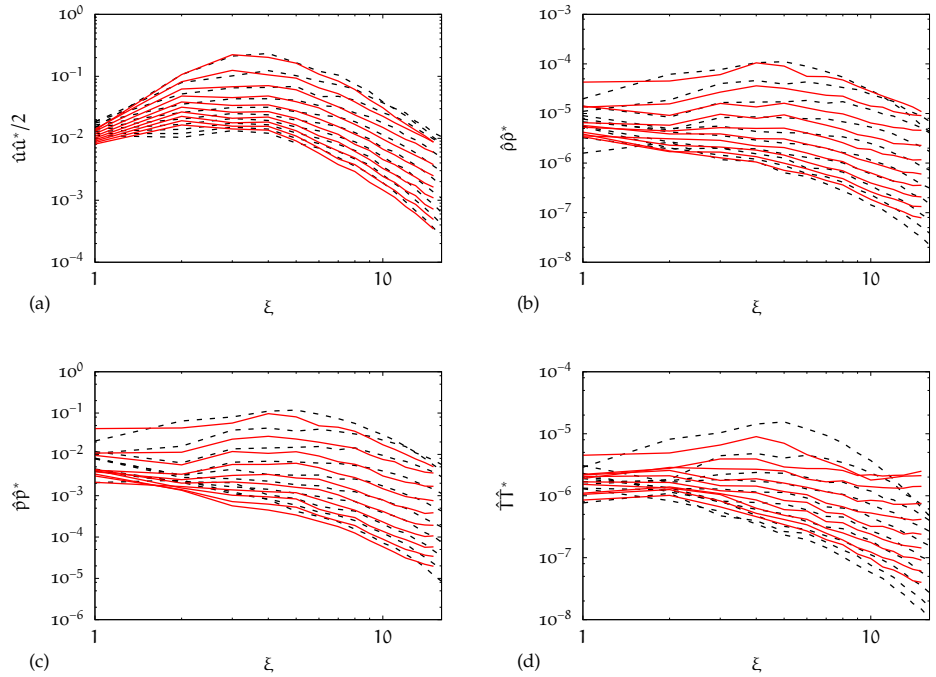

Figure 46: Decaying compressible isotropic turbulence with $Re_\lambda = 100$ and $Ma_t = 0.3$ on a grid with $N^3 = 32^3$ cells. Comparison of spectra at different time instants between implicit LES with the proposed scheme (——) and DNS data [47] (- - - -). *Reprinted with permission from Egerer et al. [30]. Copyright 2016, Elsevier.*

different time instants between implicit LES with the new method and DNS is presented in Fig. 46. We observe an accurate evolution of turbulence kinetic energy spectra, Fig. 46a, and spectra of thermodynamic quantities, Figs. 46b to 46d. Aliasing errors are small for large wave numbers and only significant for the temperature variance at early times. Additional means of stabilization, such as explicit filters, are not needed.

9 APPLICATION OF CATUM TO CAVITATING FLOWS

9.1 SINGLE BUBBLE COLLAPSE

Neglecting viscous effects, non-condensable gas, and surface tension, the evolution of a spherical vapor bubble is described by a simplified form of the Rayleigh-Plesset equation [33]

$$R\ddot{R} + \frac{3}{2}\dot{R}^2 = \frac{p_v - p_\infty}{\rho_l}, \tag{85}$$

where R denotes the radius of the vapor bubble, $\dot{R}$ the velocity of the bubble surface, $\ddot{R}$ its acceleration, ρ_l the liquid density, p_∞ the ambient pressure in the liquid, and p_v the pressure of the liquid at the bubble surface. For analysis one assumes that the pressure at the surface is constant and equal to the saturation pressure of vapor, i.e., $p_v = p_{sat}$. Rayleigh [81] was the first to integrate Eq. (85) in order to obtain a characteristic collapse time

$$t_{Rayleigh} \approx 0.915 R_0 \sqrt{\frac{\rho_l}{p_\infty - p_{sat}}}. \tag{86}$$

For comparison with Rayleigh's analytical solution, we consider the collapse of a 3-D spherical saturated water vapor bubble surrounded by liquid water at a reference temperature $T_{ref} = 293.15$ K.

Fig. 47a shows a sketch of the setup. A vapor bubble with an initial radius of $R_0 = 0.4 \times 10^{-3}$ m and a vapor-volume fraction of $\alpha = 0.99$ is placed within a cubic domain with an edge length of 0.1 m. Since the problem is symmetric, we consider only one-eighth of the vapor bubble. An equidistant grid is employed within a cubic subdomain with an edge length of 0.5×10^{-3} m, which encloses the vapor bubble. Grid stretching is applied in the far-field. We have performed simulations on three different grids with 22, 44 and 88 computational cells spanning the initial bubble radius, which we will denote as *coarse*, *medium* and *fine* in the following. The ambient pressure is $p_\infty = 1 \times 10^5$ bar and the initial velocity is zero everywhere. Time integration is performed by the RK2S4 scheme with CFL = 1.0.

Fig. 47b shows a comparison between the analytical and numerical evolution of the normalized bubble radius R/R_0 over normalized time $t/t_{Rayleigh}$. The bubble radius is calculated from the global vapor volume fraction in the numerical simulations. Samples are recorded at identical time instants for the three grid resolutions. The numerically predicted collapse times are almost independent of the grid resolution and in excellent agreement with the Rayleigh time $t_{Rayleigh}$. The vapor bubble collapses slightly faster on the coarse and medium grids.

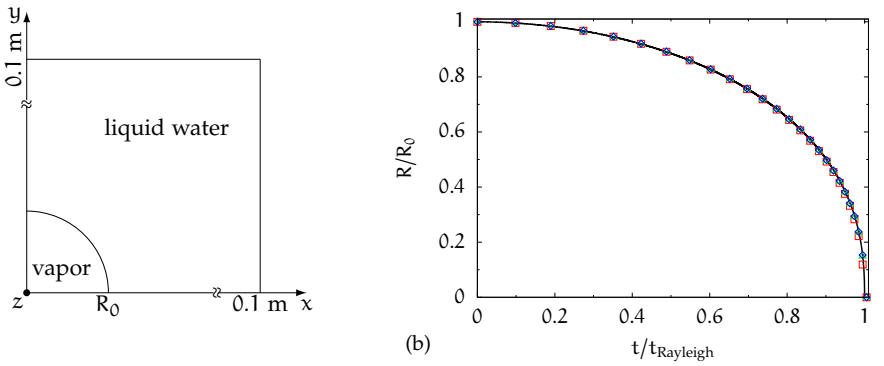

Figure 47: Collapse of a 3-D isolated vapor bubble: (a) sketch of the problem setup, (b) evolution of the normalized bubble radius R/R_0 with respect to normalized time $t/t_{Rayleigh}$. —— Rayleigh-Plesset solution, ▫ coarse grid, △ medium grid, ◇ fine grid. *Reprinted with permission from Egerer et al. [30]. Copyright 2016, Elsevier.*

9.2 BUBBLE CLOUD COLLAPSE

As a second cavitating test-case for evaluating the robustness of the present scheme, we choose the collapse of a bubble cloud above a solid wall [92]. The bubble cloud consists of 125 spherical vapor bubbles with initial radii $0.7 \leq R_{b,0} \leq 1.65$ mm and average radius $\overline{R}_{b,0} = 0.95$ mm, see Fig. 48a. The bubbles do not intersect with a minimum distance of 0.2 mm between two bubbles. Furthermore, we assume that bubbles become larger towards the center of the cloud and are spaced more densely. The vapor bubble cloud is located within a liquid-filled *inner* domain of size $20 \times 20 \times 20$ mm^3. The inner domain is embedded in a larger *outer* domain of size $4 \times 4 \times 2$ m^3. The inner domain is discretized by 220^3 cubic cells, while the grid in the outer domain consists of hexahedral cells that are stretched towards the boundaries. The initial pressure in the liquid satisfies a Laplace equation, $\Delta p = 0$, with boundary conditions $p_\infty = 40 \times 10^5$ Pa at the far-field boundaries and $p = p_{sat} = 2340$ Pa at the vapor bubble surfaces. Thereby, we ensure that the initial pressure field is free of spurious acoustics. The velocity field is zero initially and the initial temperature is $T = 293$ K. Viscous effects and non-condensable gas are neglected. For time integration we use the RK2S4 scheme with CFL = 1.0. Fig. 48b shows active regions of the proposed vapor volume sensor on three cut planes at initial time. It is observed that the active regions of the vapor volume sensor coincide with the vapor-bubble surfaces demonstrating the correct behavior of the proposed flow sensor. The time of the initial collapse of the bubble cloud is nearly identical between CATUM and the new method, see Fig. 49a. The rebounds also follow a similar evolution with the exception that the predicted vapor volume fraction for the first and second rebound is slightly larger for the new method. Thus, we conclude that the global dynamics of the bubble cloud is not altered by the new hybrid formulation. The same result holds for

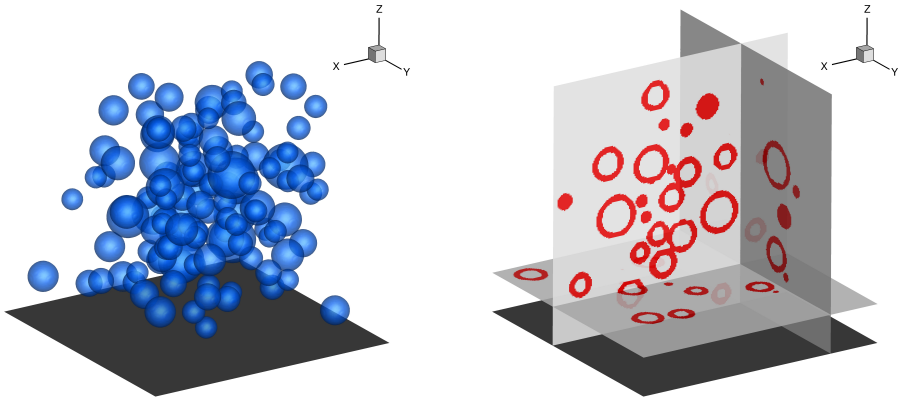

(a) (b)

Figure 48: Vapor bubble cloud collapse above a solid wall: (a) initial distribution of vapor bubbles visualized by iso-surfaces of vapor volume fraction $\alpha = 0.1$, and (b) initial active regions of the flow sensor on three cut planes. *Reprinted with permission from Egerer et al. [30]. Copyright 2016, Elsevier.*

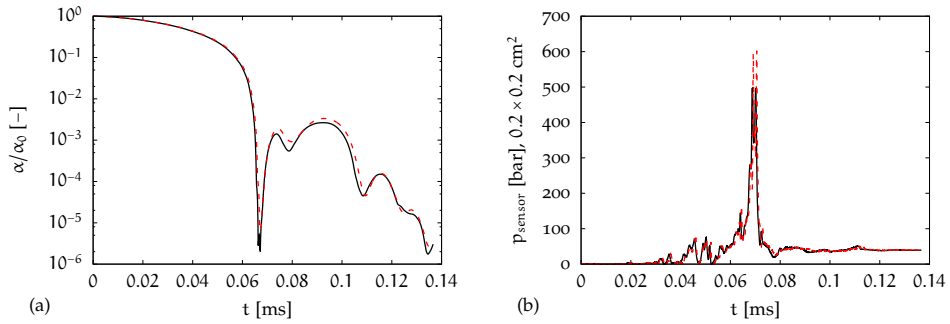

Figure 49: Comparison between baseline (——) and proposed scheme (- - - -) of the evolution of (a) the vapor volume fraction of the bubble cloud and (b) the integral value of the static pressure as measured on a numerical pressure sensor of size 0.2×0.2 cm^2. *Reprinted with permission from Egerer et al. [30]. Copyright 2016, Elsevier.*

Table 10: Initial conditions of temporally evolving cavitating mixing layers matching cavitation and Reynolds number of the experiment by Aeschlimann et al. [6, 7]. *Reprinted with permission from Egerer et al. [30]. Copyright 2016, Elsevier.*

σ_c	ΔU	ρ_∞	p_∞	T_∞	$\delta_{\omega,0}$
–	m/s	kg/m^3	$\times 10^5$ Pa	K	$\times 10^{-3}$ m
1.0	40.0	998.52	8.012	293.15	0.4
0.167	40.0	998.22	1.357	293.15	0.4
0.1	40.0	998.19	0.822	293.15	0.4

the static pressure recorded on a numerical sensor on the bottom wall of size 0.2×0.2 cm^2. We observe that the maximum pressure recorded on the wall is larger for the new method while the overall time evolution of the pressure signal is similar, cf. Fig. 49b. Finally, we conclude that restricting an upwind-biased reconstruction to regions where the vapor volume fraction rapidly changes is sufficient for stable time integration.

9.3 CAVITATING TURBULENT MIXING LAYER

As final test case, we perform LES of a temporally evolving turbulent mixing layer in water with the new method and use results obtained with ALDM adopted for cavitating flows [29] as reference. We consider three cases, one without cavitation ($\sigma_c = 1.0$) and two with cavitation ($\sigma_c = 0.167$ and $\sigma_c = 0.1$). The cavitation numbers are taken from the experiment by Aeschlimann et al. [6, 7]. The initial conditions are provided in Table 10. The initial streamwise velocity profile is $u = (\Delta U/2)\tanh(4y/\delta_{\omega,0})$. We choose the initial vorticity thickness in the simulations, $\delta_{\omega,0}$, so that we match the Reynolds number of the experiment, $Re \approx 1.5 \times 10^5$, at the beginning of the self-similar region. Solenoidal 3-D velocity fluctuations, which are restricted to the initial shear layer by an exponential damping function, $\exp(-y^2/(2\delta_{\omega,0}))$, are super-imposed onto the mean velocity in order to trigger transition. Their maximum amplitude is $0.1\Delta U$. We use the RK3S3 scheme for time integration with CFL = 0.5.

The computational domain is a rectangular box of size $L_x \times L_y \times L_z = 300 \times 100 \times 60\delta_{\omega,0}$ in streamwise, cross-stream and spanwise direction, see Fig. 50. Periodic boundary conditions are applied in streamwise and spanwise directions, while we set the static pressure according to Table 10 at the cross-stream boundaries. The domain is discretized by $N_x \times N_y \times N_z = 768 \times 192 \times 192$ cells. The grid spacing is homogeneous in streamwise and spanwise direction, while a hyperbolic tangent function is employed in cross-stream direction to refine the grid towards the mixing layer interface. Statistical quantities are computed by averaging in streamwise and spanwise directions.

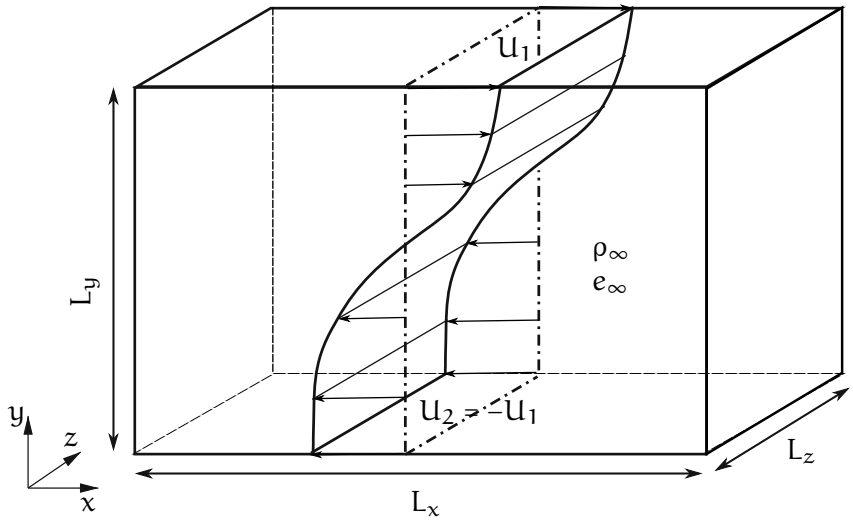

Figure 50: Computational domain for the temporally evolving cavitating mixing layer. *Reprinted with permission from Egerer et al. [30]. Copyright 2016, Elsevier.*

Fig. 51a compares the predicted temporal growth of the vorticity thickness. We find that it is independent of the cavitation number, which is in agreement with the experiments by Aeschlimann et al. [6]. Furthermore, the new method performs equally well as ALDM. The normalized growth-rate, $r_\omega = \dot{\delta}_\omega/\Delta U$, is approximately 0.08 for all simulations in the self-similar region, see dashed line in Fig. 51a, and agrees well with the experiment where the growth-rates are within the range $r_\omega = [0.09 - 0.11]$. Incompressible or low-Mach-number (quasi-incompressible) DNS [78, 85] and LES [32] of single-phase mixing layers give growth rates of $r_\omega = [0.07 - 0.08]$.

Fig. 51b shows the temporal evolution of the mean maximum vapor volume fraction. The LES with the new method agrees well with ALDM data and reproduces the experimental values within experimental-data uncertainty [7]. Note that the streamwise coordinate of the experiment was transformed to a time coordinate according to $t = x(U_c/\Delta U)_{exp}$, where $(U_c/\Delta U)_{exp}$ is the ratio of mean convection velocity U_c to velocity difference ΔU in the experiment.

Finally, we present a comparison of the mean streamwise velocity and normalized mean vapor volume profiles at $t^* = t\Delta U/\delta_{\omega,0} = 250$ between the new method, ALDM and experiment, Fig. 52. The mean streamwise velocity profiles of the new method are in excellent agreement with the ALDM reference LES and with experimental data, see Fig. 52a. The shapes of the mean vapor volume fraction profiles also agree well with ALDM and experimental data for both cavitation numbers, see Fig. 52b.

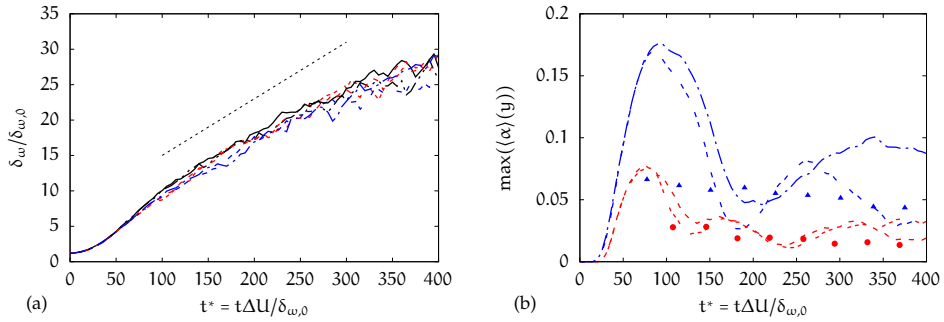

Figure 51: Comparison of (a) the growth of the vorticity thickness δ_ω and (b) the mean maximum vapor volume fraction α_{max}. $\sigma_c = 1.0$: – · · – ALDM, —— present scheme; $\sigma_c = 0.167$: ● Aeschlimann et al. [7], - - - - - - ALDM, - - - - present scheme; $\sigma_c = 0.1$: ▲ Aeschlimann et al. [7], – – – – ALDM, – · – present scheme. *Reprinted with permission from Egerer et al. [30]. Copyright 2016, Elsevier.*

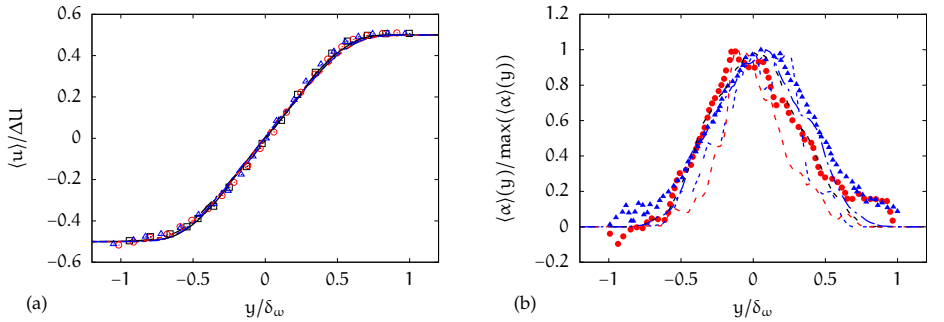

Figure 52: Mean profiles at time $t^* = t\Delta U/\delta_{omega,0} = 250$ of (a) the mean streamwise velocity $\langle u\rangle$ and (b) the mean vapor volume fraction α. $\sigma_c = 0.167$: ● Aeschlimann et al. [7], - - - - - - ALDM, - - - - present scheme; $\sigma_c = 0.1$: ▲ Aeschlimann et al. [7], – – – – ALDM, – · – present scheme. *Reprinted with permission from Egerer et al. [30]. Copyright 2016, Elsevier.*

Part IV

FINAL REMARKS

10 SUMMARY AND CONCLUSIONS ON ALDM

We have demonstrated that a thermodynamic equilibrium cavitation model coupled with a state-of-the-art implicit LES model is a feasible approach to the simulation of cavitating turbulent flow in open and confined shear flows.

Quantitative comparison with experimental data of a cavitating turbulent mixing layer shows that mean velocity and vapor volume fraction are reproduced within the limits of experimental uncertainties, see Chapter 5.

Detailed and comprehensive experimental analyses of cavitating flows in sub-millimeter geometries, such as the generic throttle considered in Chapter 6, are extremely challenging. LES, where the full unsteady and three-dimensional flow field information is available, significantly enhance the understanding of the flow in such devices.

For the very complex flow through a generic throttle geometry LES results reproduce the essential cavitation and flow dynamics that are representative also for fuel injectors. For example, the change in cavitation and flow dynamics associated with the transition from a non-chocked to a chocked flow were predicted properly. At a non-chocked operating point, high-frequency recurring vortex cavitation, associated with boundary-layer separation and shear-layer instabilities at the throttle intake, is the predominant cavitation mechanism. On the other hand, the cavitation process is driven by inertia effects in the first part of the throttle at a chocked operating point. The analysis of the mean flow field revealed a system of streamwise vortices that was not anticipated and could not be directly inferred from the experimental results illustrating the importance of LES investigations complementing the experiment. Their origin was traced back to the boundary layer upstream of the contraction. Compared to developed turbulent flow in a square duct, that is discussed extensively in the literature, the cavitating flow is characterized by quite different secondary mean-flow structures. Significant effects also on mean velocity profiles and resolved Reynolds stress profiles are visible.

The fully compressible treatment of the liquid and the liquid-vapor mixture, i.e., resolving dynamics of shock waves that are emitted during the final stages of the collapse of vapor structures and that play an essential role for the prediction of cavitation erosion, allows for the detection of erosion-relevant events. It is confirmed that the absolute amount of vapor is no indicator for cavitation erosion, but rather that dominant unsteady flow features, such as cavitating shear layers, need to be captured for erosion prediction.

11 SUMMARY AND CONCLUSIONS ON CATUM

We have proposed a modification of a previously established finite-volume method for inviscid simulation of cavitating flows (baseline scheme/CATUM [93, 97, 98]). The proposed modification enables LES of turbulent cavitating flow within the existing modeling framework. In previous work [29] we have demonstrated that turbulent cavitating flow can be accurately predicted by the state-of-the-art implicit LES method ALDM [46, 47] in combination with a thermodynamic equilibrium cavitation model. Part III demonstrates that we are able to improve computational efficiency by retaining the four-cell stencil of the baseline scheme CATUM while achieving comparable SGS modeling quality as ALDM, which relies on a six-cell stencil. This is achieved by switching between a central discretization with physically consistent turbulence regularization and the existing upwind-biased baseline scheme CATUM dependent on a flow sensor. Numerical dissipation is localized to regions where it is necessary for capturing large flow gradients, e.g., phase boundaries in cavitating flows. Thus, an efficient integrated approach with problem-independent discretization-scheme parameters is obtained.

Since many popular discretization schemes operate on four-cell stencils, e.g., the Jameson-Schmidt-Turkel (JST) scheme [55] or Monotonic Upstream-Centered Scheme for Conservation Laws (MUSCL), the proposed method can be easily implemented into existing codes. Moreover, the numerical dissipation introduced by the regularization of the proposed method is physically consistent with turbulence theory contrary to artificial dissipation of the JST scheme or of MUSCL schemes. Although only structured grids were considered in this thesis, the complexity for porting the proposed method to unstructured grids is comparable to that of the JST or MUSCL schemes.

12 OUTLOOK

Wall-resolved Large-Eddy Simulations as performed in Chapter 6 entail high computational cost due to DNS-like resolution requirements close to walls. Wall models might alleviate these resolution requirements. Considering operating point A of the micro throttle study, cf. Section 6.2.2, where cavitation originates in the shear layer created by the detached boundary layer, it is questionable if such boundary layer dynamics relevant for the correct prediction of cavitation dynamics are retained by standard wall function approaches [100, 101].

For the simulation of the injection process, it is necessary to include free gas as a third phase. Building on the Adaptive Local Deconvolution Method for cavitating flows, see Chapter 4, Örley et al. [77] already develop a thermodynamic closure to include free gas and investigate the flow through a rectangular injector [105] and the subsequent liquid jet break-up.

The inclusion of surface tension forces and their effect is another possible option for future research. Nevertheless, since most phase interfaces cannot be resolved in many applications, a rigorous investigation of subgrid scale terms originating from surface tension forces for cavitating flows, cf. Eqs. (20b) and (20c), is necessary.

In the present thesis, we have not considered the effect of non-condensable gas, although experimental evidence exists that it may have a significant impact on cavitation dynamics and chararcteristics of vapor collapses. For the reference experiments, non-condensable gas has been removed from the test liquid. The analysis of the influence of solved non-condensable gas on cavitation dynamics and collapse characteristics is subject of current research.

Part v

APPENDIX

AUXILIARY DATA FOR LES OF CAVITATING MIXING LAYERS

A

A.1 REYNOLDS STRESS TRANSPORT EQUATION

The transport equation for the resolved Reynolds stresses reads

$$\begin{aligned} \partial_t \overline{\rho} \widetilde{u_i'' u_j''} + \frac{\partial}{\partial x_k} \left(\overline{\rho} \widetilde{u}_k \widetilde{u_i'' u_j''} \right) = \\ \overline{\rho} \left(P_{ij} - \varepsilon_{ij} - \varepsilon_{ij}^{SGS} \right) - \frac{\partial}{\partial x_k} \left(T_{ijk}^t + T_{ijk}^p + T_{ijk}^\tau \right) + \Phi_{ij} + \Pi_{ij}, \end{aligned} \tag{87}$$

where

$$P_{ij} = - \left(\widetilde{u_i'' u_k''} \frac{\partial \widetilde{u}_j}{\partial x_k} + \widetilde{u_j'' u_k''} \frac{\partial \widetilde{u}_i}{\partial x_k} \right) \tag{88a}$$

is turbulent production,

$$T_{ijk}^t = \overline{\rho u_i'' u_j'' u_k''}, \tag{88b}$$

$$T_{ijk}^p = \overline{p' u_i'} \delta_{jk} + \overline{p' u_j'} \delta_{ik}, \tag{88c}$$

$$T_{ijk}^\tau = - \left(\overline{\tau_{jk}' u_i''} + \overline{\tau_{ik}' u_j''} \right), \tag{88d}$$

are turbulent, pressure and viscous transport

$$\Phi_{ij} = \overline{u_i''} \left(\frac{\partial \overline{\tau}_{jk}}{\partial x_k} - \frac{\partial \overline{p}}{\partial x_j} \right) + \overline{u_j''} \left(\frac{\partial \overline{\tau}_{ik}}{\partial x_k} - \frac{\partial \overline{p}}{\partial x_i} \right), \tag{88e}$$

represents exchange due to variable inertia,

$$\Pi_{ij} = \overline{p' \left(\frac{\partial u_i''}{\partial x_j} + \frac{\partial u_j''}{\partial x_i} \right)}, \tag{88f}$$

is pressure dilatation, and

$$\varepsilon_{ij} = \overline{\frac{1}{\overline{\rho}} \tau_{jk}' \frac{\partial u_i''}{\partial x_k} + \tau_{ik}' \frac{\partial u_j''}{\partial x_k}}, \tag{88g}$$

$$\tag{88h}$$

is resolved dissipation. Contributions from subgrid scales are lumped together in ε_{ij}^{SGS}. Figs. 53 to 56 show a comparison of budgets of the Reynolds stress transport equation terms for the non-zero components of the Reynolds stress tensor, $\widetilde{u_i'' u_j''}$, for different cavitation numbers.

For the streamwise Reynolds stress production is balanced by the pressure dilatation and dissipation which is completely provided by the SGS model. The pressure dilatation redistributes energy contained in the streamwise fluctuations to fluctuations in the other spatial dimensions. The cavitation number has no significant effect on the budget terms.

For the Reynolds shear stress we observe an effect of the cavitation number on the production and pressure dilatation, cf. Fig. 54a. For decreasing cavitation number both terms decrease in their magnitude. Production is balanced by contribution of the pressure dilatation.

For the cross-stream Reynolds stress pressure dilatation is the main source, cf. Fig. 55a. The pressure dilatation term slightly decreases for decreasing cavitation numbers.

Similar effects can be observed for the spanwise Reynolds stress, cf. Fig. 56a.

We would like to note, however, that there is the possibility of model-related uncertainties in the presented data of the Reynolds stress transport equations. Especially effects of non-resolved phase interfaces and their interaction with turbulence is unclear. In order to investigate such phenomena, fully resolved simulations are required, i.e., DNS of turbulence as well as phase interfaces. Such simulations are, however, not feasible with currently available computing power.

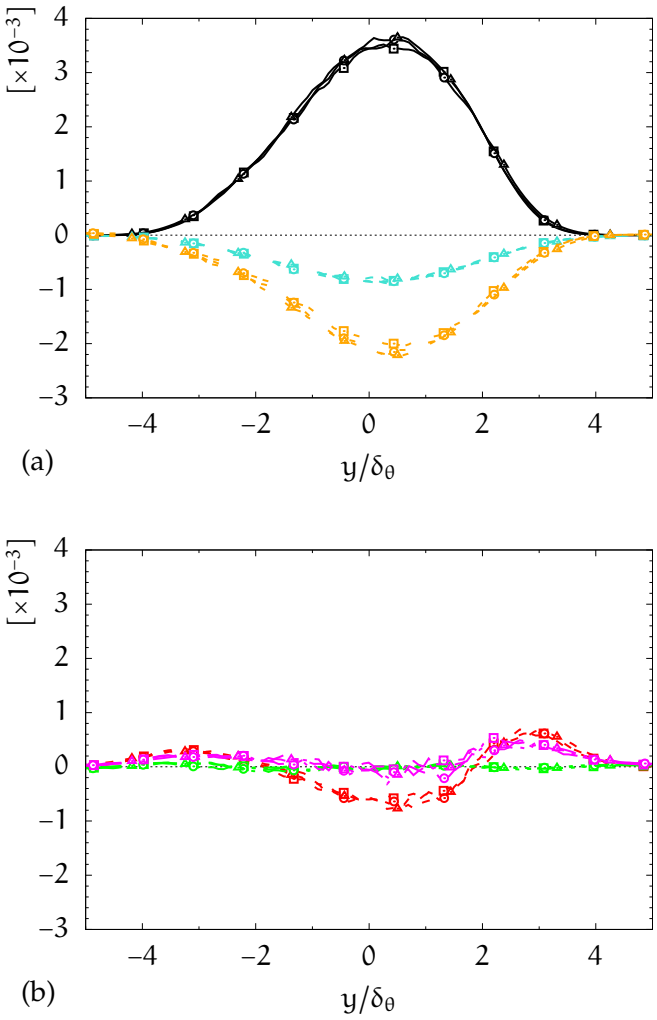

Figure 53: Budgets of streamwise Reynolds stress transport equation in cavitating mixing layers: comparison between mixing layer LES at different cavitation numbers. Profiles are normalized by $(\Delta U)^3/\delta_\theta$. Symbols indicate different cavitation numbers: ▫ $\sigma_c = \infty$; ○ $\sigma_c = 0.167$; ▵ $\sigma_c = 0.1$. Line styles/colors indicate the various terms of the Reynolds stress transport equation (87): —— P_{11}; - - - - $-\partial_k T^t_{11k}/\bar{\rho}$; — · · — $-\partial_k T^p_{11k}/\bar{\rho}$; - - - - $-\varepsilon^{SGS}_{11}$. — · — $\partial_k(\bar{\rho}\widetilde{u}_k\widetilde{u''_1u''_1})/\bar{\rho}$; --- --- $\Pi_{11}/\bar{\rho}$. Note that Φ_{11} and ε_{11} are zero and not shown.

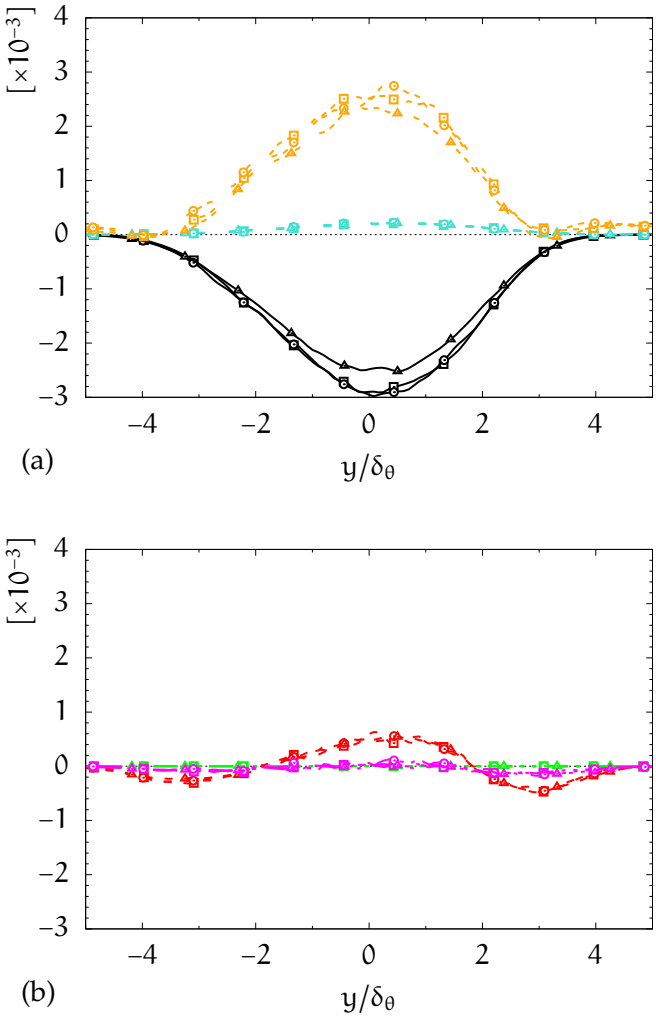

Figure 54: Budgets of Reynolds shear-stress transport equation in cavitating mixing layers: comparison between mixing layer LES at different cavitation numbers. Profiles are normalized by $(\Delta U)^3/\delta_\theta$. Symbols indicate different cavitation numbers: ▫ $\sigma_c = \infty$; ○ $\sigma_c = 0.167$; ▵ $\sigma_c = 0.1$. Line styles/colors indicate the various terms of the TKE transport equation (55): —— P_{12}; - - - - $-\partial_k T^t_{12k}/\bar{\rho}$; — · · — $-\partial_k T^p_{12k}/\bar{\rho}$; -- -- $-\varepsilon^{SGS}_{12}$. — · — $\partial_k(\bar{\rho}\widetilde{u}_k\widetilde{u''_1u''_2})/\bar{\rho}$; --- --- $\Pi_{12}/\bar{\rho}$. Note that Φ_{12} and ε_{12} are zero and not shown.

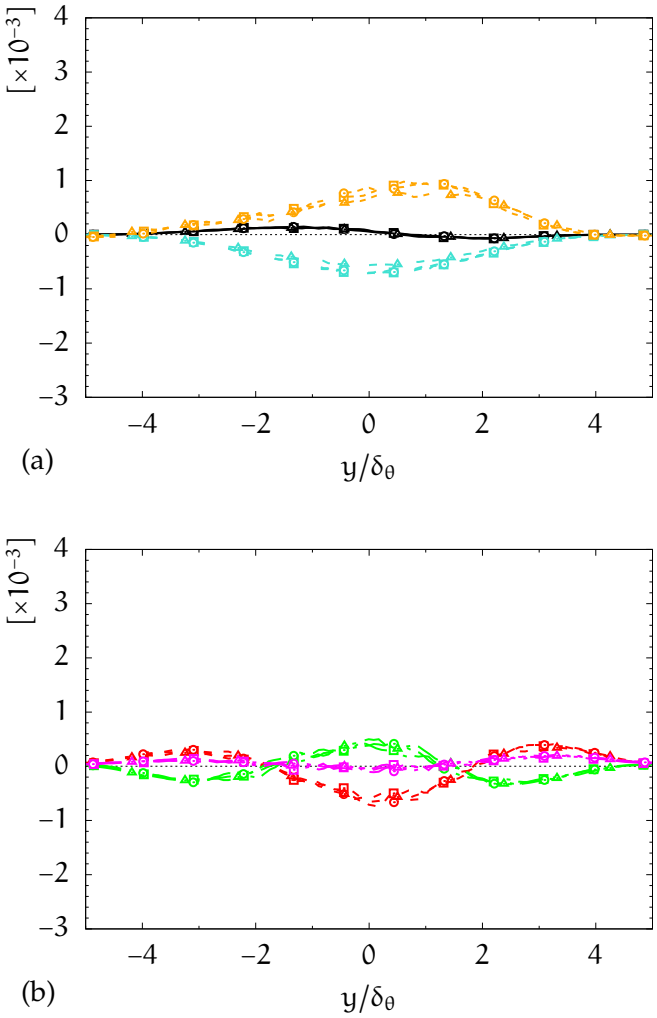

Figure 55: Budgets of cross-stream Reynolds stress transport equation in cavitating mixing layers: comparison between mixing layer LES at different cavitation numbers. Profiles are normalized by $(\Delta U)^3/\delta_\theta$. Symbols indicate different cavitation numbers: ▫ $\sigma_c = \infty$; ○ $\sigma_c = 0.167$; ▵ $\sigma_c = 0.1$. Line styles/colors indicate the various terms of the TKE transport equation (55): —— P_{22}; - - - - $-\partial_k T^t_{22k}/\bar{\rho}$; — · · — $-\partial_k T^p_{22k}/\bar{\rho}$; - - - - $-\varepsilon^{SGS}_{22}$. — · — $\partial_k(\bar{\rho}\widetilde{u}_k\widetilde{u''_2u''_2})/\bar{\rho}$; - - - - $\Pi_{22}/\bar{\rho}$. Note that Φ_{22} and ε_{22} are zero and not shown.

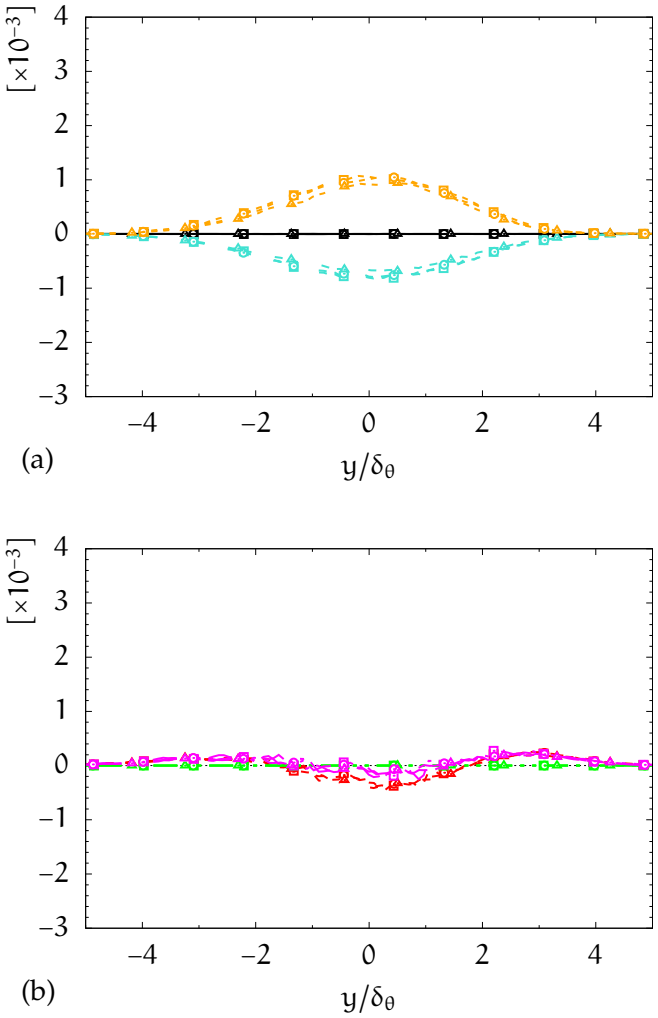

Figure 56: Budgets of spanwise Reynolds stress transport equation in cavitating mixing layers: comparison between mixing layer LES at different cavitation numbers. Profiles are normalized by $(\Delta U)^3/\delta_\theta$. Symbols indicate different cavitation numbers: ▫ $\sigma_c = \infty$; ○ $\sigma_c = 0.167$; ▵ $\sigma_c = 0.1$. Line styles/colors indicate the various terms of the TKE transport equation (55): —— P_{TKE}; - - - - $-\partial_k T^t_{k,TKE}/\bar{\rho}$; — · · — $-\partial_k T^p_{k,TKE}/\bar{\rho}$; - - - $-\varepsilon^{SGS}_{TKE}$. — · — $\partial_k(\overline{\rho}\widetilde{u}_k k)/\bar{\rho}$; --- --- $\Pi_{TKE}/\bar{\rho}$. Note that Φ_{TKE} and ε_{TKE} are zero and not shown.

B AUXILIARY DATA FOR LES OF MICRO CHANNEL FLOW

B.1 REYNOLDS STRESS TENSOR PROFILES

The Reynolds stress components for OPA show larger values compared to developed plain channel flow data due to the recirculation zone at $x/l \approx 0.3$ and due to collapsing vapor structures in this region, see Fig. 57. Further downstream the turbulent boundary layer redevelops and values comparable to developed turbulent boundary layers are found. Towards the center of the throttle the influence of the vortices γ_A can be observed which results in larger Reynolds stresses. Fluctuations u' and v' exhibit the same sign resulting in positive Reynolds shear stresses, see Fig. 57b. We find similar trends for the spanwise variation of Reynolds stresses at streamwise position $x/l = 0.8$, see Fig. 58.

For OPB the stable vapor sheet prevents the development of a turbulent boundary layer. Consequently, Reynolds stresses are small at the wall, see Fig. 59. The streamwise Reynolds stress and Reynolds shear stress exhibit large values at the boundary of the vapor sheet, see streamwise positions at $x/l = 0.3$ and $x/l = 0.5$ in Figs. 59a and 59b. The spanwise variation of the Reynolds stresses is dominated by the system of vortices, see Fig. 60.

B.2 QUALITATIVE COMPARISON WITH INVISCID SOLUTION

In Fig. 61 we qualitatively compare cavitation structures between the LES and inviscid solutions at two time instants for the generic throttle flow.

For OPA the inviscid solutions exhibits a larger maximum extent of the cavitation region, compare Fig. 61a with Figs. 61c and 61e. The cavitation structures predicted by the inviscid solution resemble better the third state observed in the experimental light transmission images, see Fig. 22c.

For OPB the center vortices Γ_A and Γ_B are missing in the inviscid solutions due to missing velocity gradient in the boundary layers, compare Fig. 61b with Figs. 61d and 61f. Moreover, the sheet cavity completely detached in the inviscid case and has to redevelop subsequently, compare Fig. 61d with Fig. 61f, which is not observed in the experiment.

Nevertheless, solutions obtained with a compressible but inviscid framework can help in the design process since main features of the cavitation dynamics are still retained (shedding in case of OPA, sheet cavity in case of OPB) and the time to solution is smaller by orders of magnitude.

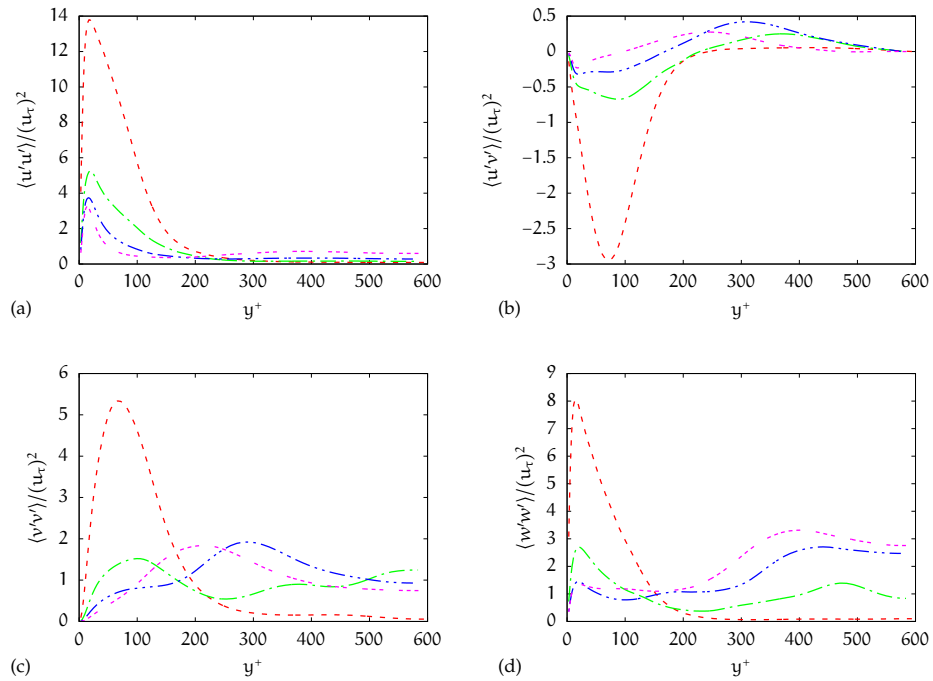

Figure 57: Streamwise variation of wall-normal profiles of (a) streamwise Reynolds stress, (b) Reynolds shear stress, (c) transverse Reynolds stress, and (d) spanwise Reynolds stress at $z = 0$ for OPA of the generic throttle. Reynolds stresses and wall distance are scaled by the local friction velocity u_τ and the local viscous lengthscale δ_μ, respectively. Streamwise positions are - - - - $x/l = 0.3$, — · — $x/l = 0.5$, — ·· — $x/l = 0.7$, and --- --- $x/l = 0.9$. *Reprinted with permission from Egerer et al. [29]. Copyright 2014, AIP Publishing LLC.*

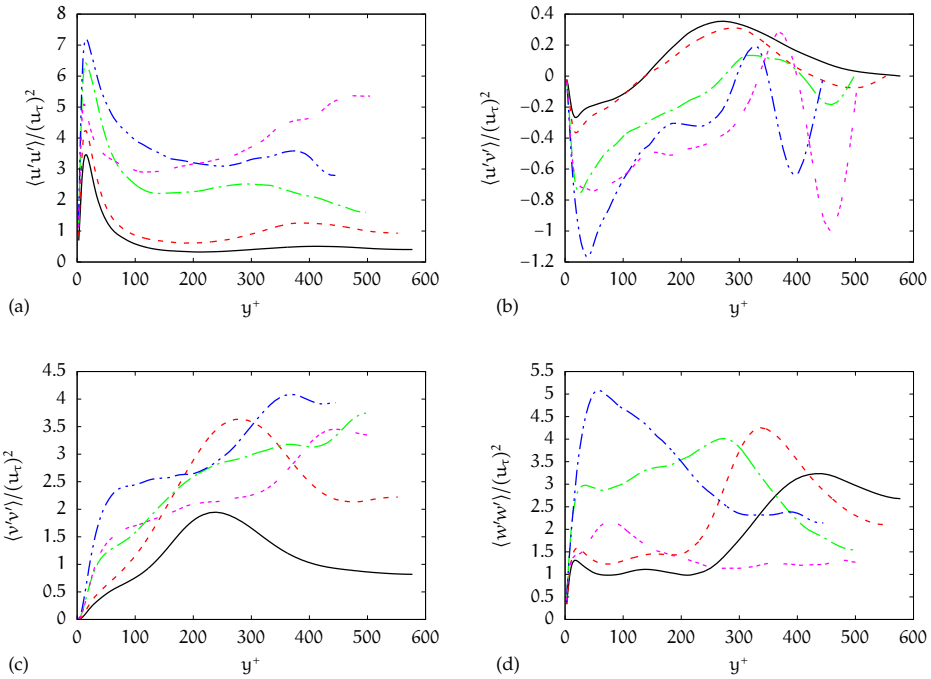

Figure 58: Spanwise variation of wall-normal profiles of (a) streamwise Reynolds stress, (b) Reynolds shear stress, (c) transverse Reynolds stress, and (d) spanwise Reynolds stress at $x/l = 0.8$ for OPA of the generic throttle. Reynolds stresses and wall distance are scaled by the local friction velocity u_τ and the local viscous lengthscale δ_μ, respectively. Spanwise positions are —— $2z/W = 0$, - - - - $2z/W = 0.25$, -·-· $2z/W = 0.5$, -··-·· $2z/W = 0.75$, and --- --- $2z/W = 0.9$. *Reprinted with permission from Egerer et al. [29]. Copyright 2014, AIP Publishing LLC.*

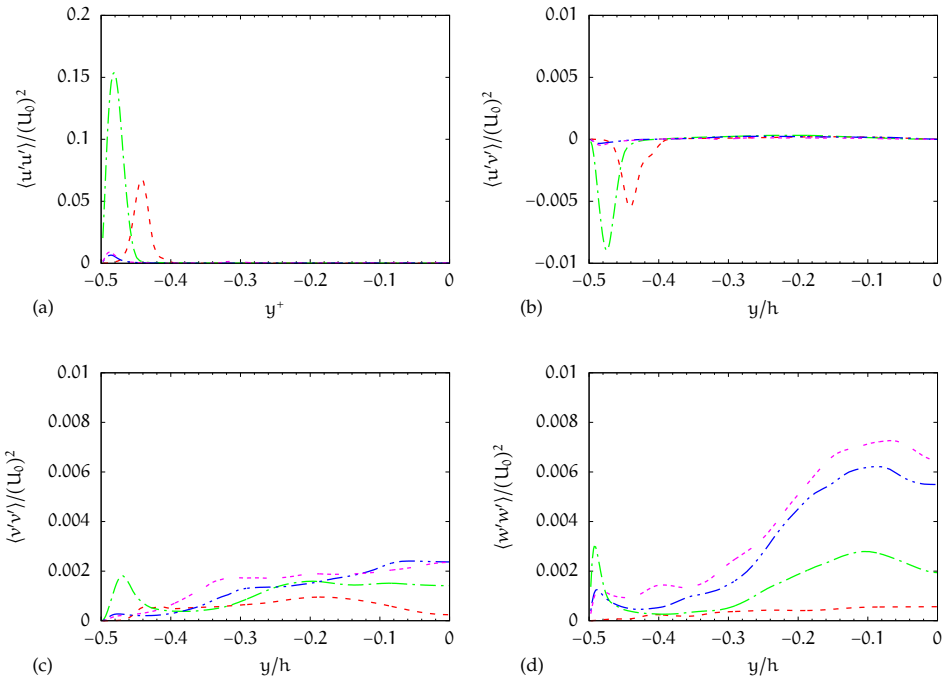

Figure 59: Streamwise variation of wall-normal profiles of (a) streamwise Reynolds stress, (b) Reynolds shear stress, (c) transverse Reynolds stress, and (d) spanwise Reynolds stress at $z = 0$ for OPB of the generic throttle. Reynolds stresses normalized by mean streamwise velocity at the centerline U_0 at the considered spanwise position. Wall distance normalized by throttle height h. Streamwise positions are - - - - $x/l = 0.3$, — · — $x/l = 0.5$, — ·· — $x/l = 0.7$, and --- --- $x/l = 0.9$. *Reprinted with permission from Egerer et al. [29]. Copyright 2014, AIP Publishing LLC.*

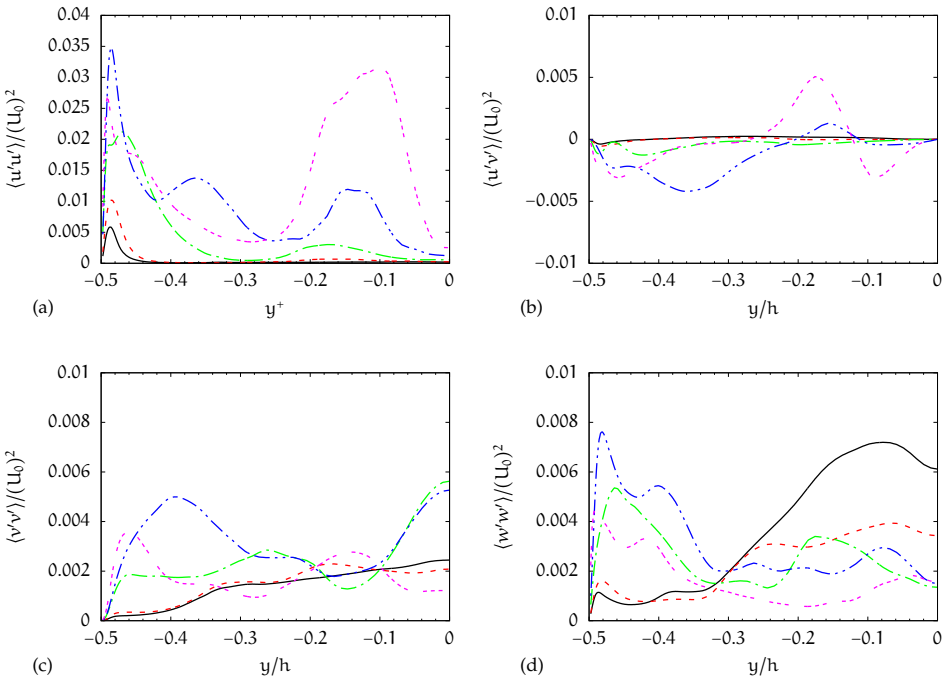

Figure 60: Spanwise variation of wall-normal profiles of (a) streamwise Reynolds stress, (b) Reynolds shear stress, (c) transverse Reynolds stress, and (d) spanwise Reynolds stress at $x/l = 0.8$ for OPB of the generic throttle. Reynolds stresses normalized by mean streamwise velocity at the centerline U_0 at the considered spanwise position. Wall distance normalized by throttle height h. Spanwise positions are —— $2z/W = 0$, - - - - $2z/W = 0.25$, — · — $2z/W = 0.5$, — · · — $2z/W = 0.75$, and - - - - - - $2z/W = 0.9$. *Reprinted with permission from Egerer et al. [29]. Copyright 2014, AIP Publishing LLC.*

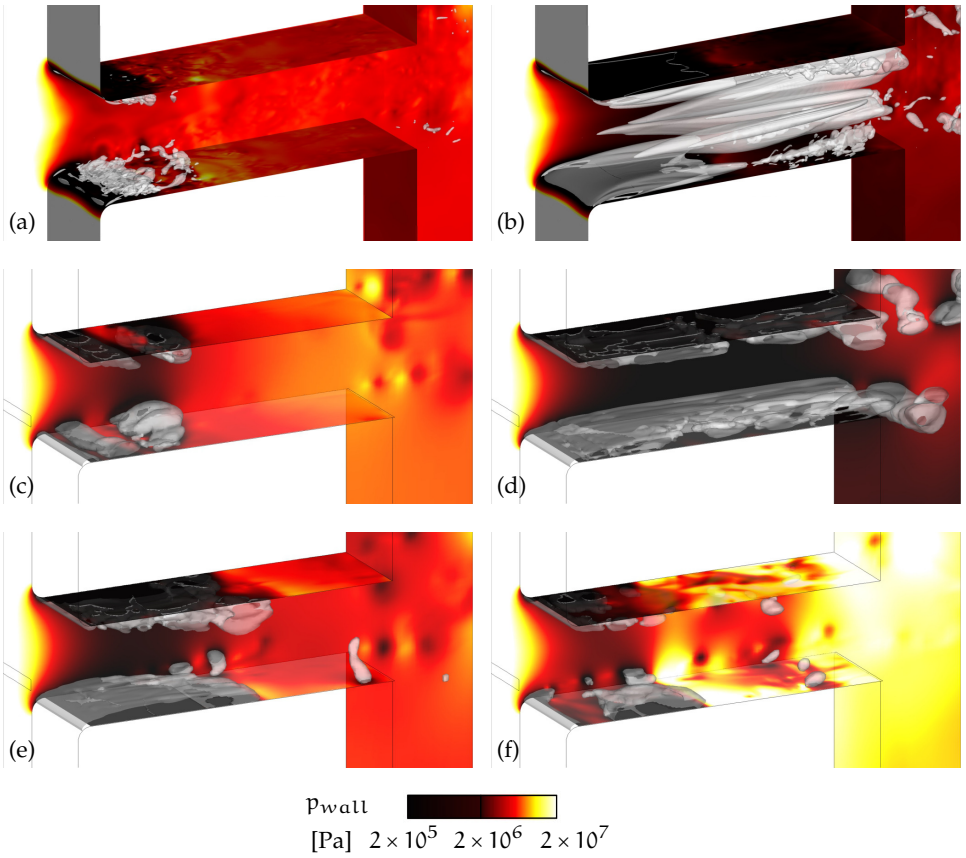

Figure 61: Qualitative comparison of instantaneous vapor structures between LES (a,b) and inviscid solution at two time instants (c,d,e,f): (a,c,e) OPA, (b,d,f) OPB of the generic throttle. Additionally, the instantaneous wall pressure is shown.

BIBLIOGRAPHY

[1] *Experimental and CFD technology for* PREV*entive reduction of Diesel engine emissions caused by cavitation* ERO*sion (*PREVERO*)*. Final Technical Report NNE5-2001-00451, AVL List GmbH - AVL, 2006. URL http://cordis.europa.eu/projects/rcn/67547_en.html.

[2] *Release on the IAPWS Formulation 2008 for the Viscosity of Ordinary Water Substance*. Technical report, The International Association for the Properties of Water and Steam, 2008. URL http://www.iapws.org.

[3] *Release on the IAPWS Formulation 2011 for the Thermal Conductivity of Ordinary Water Substance*. Technical report, The International Association for the Properties of Water and Steam, 2011. URL http://www.iapws.org.

[4] N. A. Adams and S. J. Schmidt: *Shocks in Cavitating Flows*, volume 8 of *Shock Wave Science and Technology Reference Library*, chapter 8, pp. 235–256. Springer Berlin Heidelberg, 2013, ISBN 978-3-642-34296-7. URL http://dx.doi.org/10.1007/978-3-642-34297-4_8.

[5] N. A. Adams and K. Shariff: A high-resolution hybrid compact-eno scheme for shock-turbulence interaction problems. *Journal of Computational Physics*, **127**(1):27–51, 1996. URL http://dx.doi.org/10.1006/Jcph.1996.0156.

[6] V. Aeschlimann, S. Barre, and H. Djeridi: Velocity field analysis in an experimental cavitating mixing layer. *Physics of Fluids*, **23**(5):055105, 2011. URL http://dx.doi.org/10.1063/1.3592327.

[7] V. Aeschlimann, S. Barre, and S. Legoupil: X-ray attenuation measurements in a cavitating mixing layer for instantaneous two-dimensional void ratio determination. *Physics of Fluids*, **23**(5):055101, 2011. URL http://dx.doi.org/10.1063/1.3586801.

[8] V. Aeschlimann, S. Prothin, S. Barre, and H. Djeridi: High speed visualizations of the cavitating vortices of 2D mixing layer. *European Journal of Mechanics B-Fluids*, **31**:171–180, 2012. URL http://dx.doi.org/10.1016/J.Euromechflu.2011.07.004.

[9] A. Andriotis, M. Gavaises, and C. Arcoumanis: Vortex flow and cavitation in Diesel injector nozzles. *Journal of Fluid Mechanics*, **610**:195–215, 2008. URL http://dx.doi.org/10.1017/S0022112008002668.

[10] W. Aniszewski, A. Boguslawski, M. Marek, and A. Tyliszczak: A new approach to sub-grid surface tension for LES of two-phase

flows. *Journal of Computational Physics*, **231**(21):7368–7397, 2012. URL http://dx.doi.org/10.1016/J.Jcp.2012.07.016.

[11] R. E. A. Arndt: Cavitation in vortical flows. *Annual Review of Fluid Mechanics*, **34**:143–175, 2002. URL http://dx.doi.org/10.1146/Annurev.Fluid.34.082301.114957.

[12] O. Asi: Failure of a Diesel engine injector nozzle by cavitation damage. *Engineering Failure Analysis*, **13**(7):1126–1133, 2006. URL http://dx.doi.org/10.1016/J.Engfailanal.2005.07.021.

[13] D. R. H. Beattie and P. B. Whalley: A simple two-phase frictional pressure drop calculation method. *International Journal of Multiphase Flow*, **8**(1):83–87, 1982. URL http://dx.doi.org/10.1016/0301-9322(82)90009-X.

[14] R. E. Bensow and G. Bark: Implicit LES predictions of the cavitating flow on a propeller. *Journal of Fluids Engineering-Transactions of the Asme*, **132**(4):041302, 2010. URL http://dx.doi.org/10.1115/1.4001342.

[15] W. Bergwerk: Flow pattern in Diesel nozzle spray holes. *Proceedings of the Institution of Mechanical Engineers*, **173**(1):655–660, 1959. URL http://dx.doi.org/10.1243/pime_proc_1959_173_054_02.

[16] J. U. Brackbill, D. B. Kothe, and C. Zemach: A continuum method for modeling surface-tension. *Journal of Computational Physics*, **100**(2):335–354, 1992. URL http://dx.doi.org/10.1016/0021-9991(92)90240-Y.

[17] C. E. Brennen: *Cavitation and Bubble Dynamics*. Oxford University Press, New York, 1995, ISBN 0-19-509409-3. URL http://resolver.caltech.edu/CaltechBOOK:1995.001.

[18] R. Courant, K. Friedrichs, and H. Lewy: Über die partiellen Differenzengleichungen der mathematischen Physik. *Mathematische Annalen*, **100**(1):32–74, 1928. URL http://dx.doi.org/10.1007/BF01448839.

[19] J. M. Delhaye: Jump conditions and entropy sources in two-phase systems. Local instant formulation. *International Journal of Multiphase Flow*, **1**(3):395–409, 1974. URL http://dx.doi.org/10.1016/0301-9322(74)90012-3.

[20] A. O. Demuren and W. Rodi: Calculation of turbulence-driven secondary motion in non-circular ducts. *Journal of Fluid Mechanics*, **140**(Mar):189–222, 1984. URL http://dx.doi.org/Doi10.1017/S0022112084000574.

[21] N. Dittakavi, A. Chunekar, and S. Frankel: Large eddy simulation of turbulent-cavitation interactions in a Venturi nozzle. *Journal of Fluids Engineering*, **132**(12):121301, 2010. URL http://dx.doi.org/10.1115/1.4001971.

[22] H. H. Dixon: Note on the tensile strength of water. *Scientific Proceedings of the Royal Dublin Society*, **12**(60), 1909.

[23] F. Ducros, V. Ferrand, F. Nicoud, C. Weber, D. Darracq, C. Gacherieu, and T. Poinsot: Large-eddy simulation of the shock/turbulence interaction. *Journal of Computational Physics*, **152**(2):517–549, 1999. URL http://dx.doi.org/10.1006/Jcph.1999.6238.

[24] D. J. Duke, D. P. Schmidt, K. Neroorkar, A. L. Kastengren, and C. F. Powell: High-resolution large eddy simulations of cavitating gasoline-ethanol blends. *International Journal of Engine Research*, **14**(6):578–589, 2013. URL http://dx.doi.org/10.1177/1468087413501824.

[25] M. Dumbser, U. Iben, and C.-D. Munz: Efficient implementation of high order unstructured WENO schemes for cavitating flows. *Computers & Fluids*, **86**(0):141–168, 2013. URL http://dx.doi.org/10.1016/j.compfluid.2013.07.011.

[26] J. Dumond, F. Magagnato, and A. Class: Stochastic-field cavitation model. *Physics of Fluids*, **25**:073302, 2013. URL http://dx.doi.org/10.1063/1.4813813.

[27] C. P. Egerer, S. Hickel, S. J. Schmidt, and N. A. Adams: Implicit large-eddy simulation of cavitation in a turbulent shear layer. In *Eighth International Symposium on Cavitation (CAV 2012)*, edited by C.-D. Ohl, E. Klaseboer, S. W. Ohl, S. W. Gong, and B. C. Khoo, Research Publishing Services, Singapore, 2012. URL http://dx.doi.org/10.3850/978-981-07-2826-7.

[28] C. P. Egerer, S. Hickel, S. J. Schmidt, and N. A. Adams: Turbulence modulation by phase change in a cavitating shear layer. In *9th International ERCOFTAC Symposium on Engineering Turbulence Modelling and Measurements*, Thessaloniki, Greece, 2012.

[29] C. P. Egerer, S. Hickel, S. J. Schmidt, and N. A. Adams: Large-eddy simulation of turbulent cavitating flow in a micro channel. *Physics of Fluids*, **26**(8):085102, 2014. URL http://dx.doi.org/10.1063/1.4891325.

[30] C. P. Egerer, S. J. Schmidt, S. Hickel, and N. A. Adam: Efficient implicit LES method for the simulation of turbulent cavitating flows. *Journal of Computational Physics*, **316**:453–469, 2016. URL http://dx.doi.org/10.1016/j.jcp.2016.04.021.

[31] A. Einstein: Eine neue Bestimmung der Moleküldimensionen. § 2. Berechnung des Reibungskoeffizienten einer Flüssigkeit, in welcher sehr viele kleine Kugeln in regelloser Verteilung suspendiert sind. *Annalen der Physik*, **4**(19):297–301, 1906. URL http://dx.doi.org/10.1002/andp.19063240204.

[32] H. Foysi and S. Sarkar: The compressible mixing layer: an LES study. *Theroretical and Computational Fluid Dynamics*, **24**(6):565–588, 2010. URL http://dx.doi.org/10.1007/S00162.009.0176-8.

[33] J.-P. Franc and J.-M. Michel: *Fundamentals of Cavitation*, volume 76 of *Fluid Mechanics and Its Application*. Springer Netherlands, 2004, ISBN 978-1-4020-2233-3. URL http://dx.doi.org/10.1007/1-4020-2233-6.

[34] J. Frenkel: *Kinetic Theory of Liquids*. Dover, New York, 1955.

[35] E. Garnier, N. Adams, and P. Sagaut: *Large Eddy Simulation for Compressible Flows*. Springer, Netherlands, 2009, ISBN 978-90-481-2818-1. URL http://dx.doi.org/10.1007/978-90-481-2819-8.

[36] M. Gavaises, A. Andriotis, D. Papoulias, N. Mitroglou, and A. Theodorakakos: Characterization of string cavitation in large-scale Diesel nozzles with tapered holes. *Physics of Fluids*, **21**(052107), 2009. URL http://dx.doi.org/10.1063/1.3140940.

[37] S. Gavrilakis: Numerical-simulation of low-Reynolds-number turbulent-flow through a straight square duct. *Journal of Fluid Mechanics*, **244**:101–129, 1992. URL http://dx.doi.org/10.1017/S0022112092002982.

[38] F. B. Gessner and J. B. Jones: On some aspects of fully-developed turbulent flow in rectangular channels. *Journal of Fluid Mechanics*, **23**:689–713, 1965. URL http://dx.doi.org/10.1017/S0022112065001635.

[39] E. Giannadakis, M. Gavaises, and C. Arcoumanis: Modelling of cavitation in diesel injector nozzles. *Journal of Fluid Mechanics*, **616**:153–193, 2008. URL http://dx.doi.org/10.1017/S0022112008003777.

[40] A. Gnanaskandan and K. Mahesh: A numerical method to simulate turbulent cavitating flows. *International Journal of Multiphase Flow*, **70**(0):22–34, 2015. URL http://dx.doi.org/10.1016/j.ijmultiphaseflow.2014.11.009.

[41] E. Goncalves and R. Fortes Patella: Numerical simulation of cavitating flows with homogeneous models. *Computers & Fluids*, **38**(9):1682–1696, 2009. URL http://dx.doi.org/10.1016/J.Compfluid.2009.03.001.

[42] S. Gottlieb and C.-W. Shu: Total variation diminishing Runge-Kutta schemes. *Mathematics of Computation*, **67**(221):73–85, 1998. URL http://dx.doi.org/10.1090/S0025-5718-98-00913-2.

[43] M. Grilli, S. Hickel, X. Y. Hu, and N. A. Adams: *Conservative immersed boundary method for compressible flows*. KNAW, Amsterdam, The Netherlands, 2009, ISBN 978-90-6984-590-6. URL

http://dutw1479.wbmt.tudelft.nl/~wim/academy/presentations/a3/pres_grilli.pdf.

[44] F. F. Grinstein, L. G. Margolin, and W. J. Rider: *Implicit Large Eddy Simulation: Computing Turbulent Fluid Dynamics*. Cambridge University Press, 2011, ISBN 978-0-521-86982-9. URL http://dx.doi.org/10.1017/CBO9780511618604.

[45] A. Harten, P. D. Lax, and B. van Leer: On upstream differencing and Godunov-type schemes for hyperbolic conservation laws. *SIAM Review*, **25**(1):35–61, 1983. URL http://dx.doi.org/10.1137/1025002.

[46] S. Hickel, N. A. Adams, and J. A. Domaradzki: An adaptive local deconvolution method for implicit LES. *Journal of Computational Physics*, **213**(1):413–436, 2006. URL http://dx.doi.org/10.1016/J.Jcp.2005.08.017.

[47] S. Hickel, C. P. Egerer, and J. Larsson: Subgrid-scale modeling for implicit large eddy simulation of compressible flows and shock-turbulence interaction. *Physics of Fluids*, **26**(10):106101, 2014. URL http://dx.doi.org/10.1063/1.4898641.

[48] S. Hickel, M. Mihatsch, and S. J. Schmidt: Implicit large eddy simulation of cavitation in micro channel flows. In *WIMRC 3rd International Cavitation Forum*, edited by S. C. Li, University of Warwick, UK, 2011. URL https://files.warwick.ac.uk/shengcaili/files/Proceedings+2011/5.+Bio+Medical+Applications+of+Cavitation/5.2.BioMedical-B.pdf.

[49] C. W. Hirt and B. D. Nichols: Volume of fluid (VOF) method for the dynamics of free boundaries. *Journal of Computational Physics*, **39**(1):201–225, 1981. URL http://dx.doi.org/10.1016/0021-9991(81)90145-5.

[50] A. Huser and S. Biringen: Direct numerical simulation of turbulent flow in a square duct. *Journal of Fluid Mechanics*, **257**:65–95, 1993. URL http://dx.doi.org/10.1017/S002211209300299x.

[51] U. Iben, A. Morozov, E. Winklhofer, and F. Wolf: Laser-pulse interferometry applied to high-pressure fluid flow in micro channels. *Experiments in Fluids*, **50**(3):597–611, 2011. URL http://dx.doi.org/10.1007/S00348-010-0950-9.

[52] M. Ishii and T. Hibiki: *Thermo-Fluid Dynamics of Two-Phase Flow*. Springer, New York, 2011, ISBN 978-1-4419-7984-1. URL http://dx.doi.org/10.1007/978-1-4419-7985-8.

[53] C. O. Iyer and S. L. Ceccio: The influence of developed cavitation on the flow of a turbulent shear layer. *Physics of Fluids*, **14**(10):3414–3431, 2002. URL http://dx.doi.org/10.1063/1.1501541.

[54] F. Jaegle and U. Iben: Light transmission images of micro channel flow, 2013. Private communication.

[55] A. Jameson, W. Schmidt, and E. Turkel: Numerical solution of the euler equations by finite volume methods using Runge-Kutta time-stepping schemes. *AIAA Paper*, (1981-1259), 1981. URL http://dx.doi.org/10.2514/6.1981-1259.

[56] J. Jeong and F. Hussain: On the identification of a vortex. *Journal of Fluid Mechanics*, **285**:69–94, 1995. URL http://dx.doi.org/10.1017/S0022112095000462.

[57] E. Johnsen and T. Colonius: Implementation of WENO schemes in compressible multicomponent flow problems. *Journal of Computational Physics*, **219**(2):715–732, 2006. URL http://dx.doi.org/10.1016/J.Jcp.2006.04.018.

[58] E. Johnsen and T. Colonius: Numerical simulations of non-spherical bubble collapse. *Journal of Fluid Mechanics*, **629**:231–262, 2009. URL http://dx.doi.org/10.1017/S0022112009006351.

[59] D. Juric and G. Tryggvason: Computations of boiling flows. *International Journal of Multiphase Flow*, **24**(3):387–410, 1998. URL http://dx.doi.org/10.1016/S0301-9322(97)00050-5.

[60] B. Koren: A robust upwind discretisation method for advection, diffusion and source terms. In *Numerical Methods for Advection-Diffusion Problems*, edited by C. B. Vreugdenhil and B. Koren, chapter 5, pp. 117–138, Vieweg, Braunschweig, 1993, ISBN 3528076453.

[61] A. G. Kravchenko and P. Moin: On the effect of numerical errors in large-eddy simulations of turbulent flows. *Journal of Computational Physics*, **131**(2):310–322, 1997. URL http://dx.doi.org/10.1006/Jcph.1996.5597.

[62] E. Labourasse, D. Lacanette, A. Toutant, P. Lubin, S. Vincent, O. Lebaigue, J. P. Caltagirone, and P. Sagaut: Towards large eddy simulation of isothermal two-phase flows: Governing equations and a priori tests. *International Journal of Multiphase Flow*, **33**(1):1–39, 2007. URL http://dx.doi.org/10.1016/J.Ijmultiphaseflow.2006.05.010.

[63] J. Larsson, S. K. Lele, and P. Moin: *Effect of numerical dissipation on the predicted spectra for compressible turbulence*. Annual research briefs, Center for Turbulence Research, 2007. URL https://web.stanford.edu/group/ctr/ResBriefs07/5_larsson1_pp47_58.pdf.

[64] E. Lauer, X. Y. Hu, S. Hickel, and N. A. Adams: Numerical investigation of collapsing cavity arrays. *Physics of Fluids*, **24**(052104), 2012. URL http://dx.doi.org/10.1063/1.4719142.

[65] E. Lauer, X. Y. Hu, S. Hickel, and N. A. Adams: Numerical modelling and investigation of symmetric and asymmetric cavitation bubble dynamics. *Computers & Fluids*, **69**:1–19, 2012. URL http://dx.doi.org/10.1016/J.Compfluid.2012.07.020.

[66] B. E. Launder and W. M. Ying: Secondary flows in ducts of square cross-section. *Journal of Fluid Mechanics*, **54**(2):289–295, 1972. URL http://dx.doi.org/10.1017/S0022112072000680.

[67] S. K. Lele: Compressibility effects on turbulence. *Annual Review of Fluid Mechanics*, **26**:211–254, 1994. URL http://dx.doi.org/10.1146/Annurev.Fluid.26.1.211.

[68] M. Lesieur: *Turbulence in Fluids*. Fluid Mechanics and Its Applications, 4th edition, Springer Netherlands, Dordrecht, The Netherlands, 2008, ISBN 978-1-4020-6434-0. URL http://dx.doi.org/10.1007/978-1-4020-6435-7.

[69] N. X. Lu, R. E. Bensow, and G. Bark: Large eddy simulation of cavitation development on highly skewed propellers. *J Mar Sci Tech-Japan*, **19**(2):197–214, 2014. URL http://dx.doi.org/10.1007/s00773-013-0240-3.

[70] C. Mauger, L. Méès, M. Michard, A. Azouzi, and S. Valette: Shadowgraph, schlieren and interferometry in a 2D cavitating channel flow. *Experiments in Fluids*, **53**(6):1895–1913, 2012. URL http://dx.doi.org/10.1007/s00348-012-1404-3.

[71] M. Medrano, C. Pellone, P. J. Zermatten, and F. Ayela: Hydrodynamic cavitation in microsystems. II. Simulations and optical observations. *Physics of Fluids*, **24**(4), 2012. URL http://dx.doi.org/10.1063/1.3699067.

[72] M. Medrano, P. J. Zermatten, C. Pellone, J. P. Franc, and F. Ayela: Hydrodynamic cavitation in microsystems. I. Experiments with deionized water and nanofluids. *Physics of Fluids*, **23**(12), 2011. URL http://dx.doi.org/10.1063/1.3671682.

[73] M. Meyer, A. Devesa, S. Hickel, X. Y. Hu, and N. A. Adams: A conservative immersed interface method for large-eddy simulation of incompressible flows. *Journal of Computational Physics*, **229**(18):6300–6317, 2010. URL http://dx.doi.org/10.1016/J.Jcp.2010.04.040.

[74] M. S. Mihatsch, S. J. Schmidt, M. Thalhamer, and N. A. Adams: *Numerical Prediction of Erosive Collapse Events in Unsteady Compressible Cavitating Flows*, pp. 499–510. International Center for Numerical Methods in Engineering (CIMNE), Lisbon, Portugal, 2011, ISBN 978-84-89925-79-3. URL http://congress.cimne.com/marine2011/frontal/doc/MARINE_11_ebook.pdf.

[75] T. J. O'Hern: An experimental investigation of turbulent shear flow cavitation. *Journal of Fluid Mechanics*, **215**:365–391, 1990. URL http://journals.cambridge.org/download.php?file=%2FFLM%2FFLM215%2FS0022112090002683a.pdf&code=ac169acd33103a15ad870197ef071dd8.

[76] K. Okabayashi and T. Kajishima: Investigation of turbulent modulation by cavitation for subgrid-scale modelling in LES. In *Proceedings of the 7th International Symposium on Cavitation*, Ann Arbor, Michigan, USA, 2009.

[77] F. Örley, T. Trummler, S. Hickel, M. S. Mihatsch, S. J. Schmidt, and N. A. Adams: Large-eddy simulation of cavitating nozzle flow and primary jet break-up. *Physics of Fluids*, **27**(8):086101, 2015. URL http://dx.doi.org/10.1063/1.4928701.

[78] C. Pantano and S. Sarkar: A study of compressibility effects in the high-speed turbulent shear layer using direct simulation. *Journal of Fluid Mechanics*, **451**:329–371, 2002. URL http://dx.doi.org/10.1017/S0022112001006978.

[79] S. Pirozzoli: Numerical methods for high-speed flows. *Annual Review of Fluid Mechanics*, **43**:163–194, 2011. URL http://dx.doi.org/10.1146/Annurev-Fluid-122109-160718.

[80] M. S. Plesset and A. Prosperetti: Bubble dynamics and cavitation. *Annual Review of Fluid Mechanics*, **9**:145–85, 1977. URL http://dx.doi.org/10.1146/Annurev.Fl.09.010177.001045.

[81] L. Rayleigh: VIII. On the pressure developed in a liquid during the collapse of a spherical cavity. *Philosophical Magazine Series 6*, **34**(200):94–98, 1917. URL http://dx.doi.org/10.1080/14786440808635681.

[82] R. D. Reitz and F. V. Bracco: Mechanism of atomization of a liquid jet. *Physics of Fluids*, **25**(10):1730–1742, 1982. URL http://dx.doi.org/10.1063/1.863650.

[83] J. R. Ristorcelli and G. A. Blaisdell: Consistent initial conditions for the DNS of compressible turbulence. *Physics of Fluids*, **9**(1):4–6, 1997. URL http://dx.doi.org/10.1063/1.869152.

[84] P. L. Roe: Characteristic-based schemes for the Euler equations. *Annual Review of Fluid Mechanics*, **18**:337–365, 1986. URL http://dx.doi.org/10.1146/Annurev.Fl.18.010186.002005.

[85] M. M. Rogers and R. D. Moser: Direct simulation of a selfsimilar turbulent mixing layer. *Physics of Fluids*, **6**:903–923, 1994. URL http://dx.doi.org/10.1063/1.868325.

[86] D. Rossinelli, B. Hejazialhosseini, P. Hadjidoukas, C. Bekas, A. Curioni, A. Bertsch, S. Futral, S. J. Schmidt, N. A. Adams, and P. Koumoutsakos: 11 PFLOP/s simulations of cloud cavitation collapse. In *Proceedings of the International Conference on High Performance Computing, Networking, Storage and Analysis*, pp. 1–13, ACM, Denver, Colorado, 2013. URL http://dx.doi.org/10.1145/2503210.2504565.

[87] P. Sagaut: *Large Eddy Simulation for Incompressible Flows*. 3rd edition, Springer, 2001, ISBN 978-3-662-04697-5. URL http://dx.doi.org/10.1007/978-3-662-04695-1.

[88] F. J. Salvador, J. Martinez-Lopez, J. V. Romero, and M. D. Rosello: Computational study of the cavitation phenomenon and its interaction with the turbulence developed in Diesel injector nozzles by large eddy simulation (LES). *Math Comput Model*, **57**(7-8):1656–1662, 2013. URL http://dx.doi.org/10.1016/J.Mcm.2011.10.050.

[89] W. S. Saric: Görtler vortices. *Annual Review of Fluid Mechanics*, **26**(1):379–409, 1994. URL http://dx.doi.org/10.1146/annurev.fl.26.010194.002115.

[90] R. Saurel, J. P. Cocchi, and P. B. Butler: Numerical study of cavitation in the wake of a hypervelocity underwater projectile. *Journal of Propulsion and Power*, **15**(4):513–522, 1999. URL http://dx.doi.org/10.2514/2.5473.

[91] E. Schmidt and U. Grigull: *Properties of water and steam in SI-units*. 4th edition, Springer Oldenbourg, Berlin [u.a.] München, 1989, ISBN 3-540-09601-9 0-387-09601-9.

[92] S. J. Schmidt, M. Mihatsch, M. Thalhamer, and N. A. Adams: Assessment of the prediction capability of a thermodynamic cavitation model for the collapse characteristics of a vapor-bubble cloud. In *WIMRC 3rd International Cavitation Forum*, edited by S. C. Li, University of Warwick, UK, 2011. URL https://files.warwick.ac.uk/shengcaili/files/Proceedings+2011/3.+Fundamentals+of+Cavitation/Session+1D/3.4.Fundamental-D.pdf.

[93] S. J. Schmidt, I. H. Sezal, and G. H. Schnerr: Compressible simulation of high-speed hydrodynamics with phase change. In *European Conference on Computational Fluid Dynamics*, edited by P. Wesseling, E. Onate, and J. Periaux, TU Delft, The Netherlands, 2006.

[94] S. J. Schmidt, I. H. Sezal, G. H. Schnerr, and M. Thalhamer: Riemann techniques for the simulation of compressible liquid flows with phase-transition at all Mach numbers - shock and wave dynamics in cavitating 3-d micro and macro systems. *AIAA Paper*, (2008-1238), 2008.

[95] S. J. Schmidt, M. Thalhamer, and G. H. Schnerr: Inertia controlled instability and small scale structures of sheet and cloud cavitation. In *Proceedings of the 7th International Symposium on Cavitation*, Ann Arbor, Michigan, USA, 2009.

[96] G. H. Schnerr and J. Sauer: Physical and numerical modeling of unsteady cavitation dynamics. In *Fourth International Conference on Multiphase Flows*, New Orleans, LA USA, 2001.

[97] G. H. Schnerr, I. H. Sezal, and S. J. Schmidt: Numerical investigation of three-dimensional cloud cavitation with special emphasis on collapse induced shock dynamics. *Physics of Fluids*, **20**(040703), 2008. URL http://dx.doi.org/10.1063/1.2911039.

[98] I. H. Sezal, S. J. Schmidt, G. H. Schnerr, M. Thalhamer, and M. Förster: Shock and wave dynamics in cavitating compressible liquid flows in injection nozzles. *Shock Waves*, **19**(1):49–58, 2009. URL http://dx.doi.org/10.1007/S00193-008-0185-3.

[99] E. Shams, J. Finn, and S. V. Apte: A numerical scheme for Euler-Lagrange simulation of bubbly flows in complex systems. *International Journal for Numerical Methods in Fluids*, **67**(12):1865–1898, 2011. URL http://dx.doi.org/10.1002/Fld.2452.

[100] T.-H. Shih, L. A. Povinelli, and N.-S. Liu: Application of generalized wall function for complex turbulent flows. *Journal of Turbulence*, **4**, 2003. URL http://dx.doi.org/10.1088/1468-5248/4/1/015.

[101] T.-H. Shih, L. A. Povinelli, and J. L. Lumley: *A generalized wall function*. Technical report, NASA, 1999. URL http://ntrs.nasa.gov/archive/nasa/casi.ntrs.nasa.gov/19990081113.pdf.

[102] C.-W. Shu: *Essentially non-oscillatory and weighted essentially non-oscillatory schemes for hyperbolic conservation laws*, volume 1697 of *Lecture Notes in Mathematics*, chapter 4, pp. 325–432. Springer Berlin Heidelberg, 1998, ISBN 978-3-540-64977-9. URL http://dx.doi.org/10.1007/BFb0096355.

[103] A. K. Singhal, M. M. Athavale, H. Y. Li, and Y. Jiang: Mathematical basis and validation of the full cavitation model. *Journal of Fluids Engineering - Transactions of the ASME*, **124**(3):617–624, 2002. URL http://dx.doi.org/10.1115/1.1486223.

[104] A. Sou, B. Bicer, and A. Tomiyama: Numerical simulation of incipient cavitation flow in a nozzle of fuel injector. *Computers & Fluids*, **103**:42–48, 2014. URL http://dx.doi.org/10.1016/j.compfluid.2014.07.011.

[105] A. Sou, S. Hosokawa, and A. Tomiyama: Effects of cavitation in a nozzle on liquid jet atomization. *International Journal of Heat and*

Mass Transfer, **50**(17-18):3575–3582, 2007. URL http://dx.doi.org/10.1016/J.Ijheatmasstransfer.2006.12.033.

[106] S. Stolz and N. A. Adams: An approximate deconvolution procedure for large-eddy simulation. *Physics of Fluids*, **11**(7):1699–1701, 1999. URL http://dx.doi.org/10.1063/1.869867.

[107] B. Stutz and S. Legoupil: X-ray measurements within unsteady cavitation. *Experiments in Fluids*, **35**(2):130–138, 2003. URL http://dx.doi.org/10.1007/S00348-003-0622-0.

[108] E. F. Toro: *Riemann Solvers and Numerical Methods for Fluid Dynamics – A Practical Introduction*. 3rd edition, Springer, 2009, ISBN 978-3-540-25202-3. URL http://dx.doi.org/10.1007/b79761.

[109] C. C. Tseng and L. J. Wang: Investigations of empirical coefficients of cavitation and turbulence model through steady and unsteady turbulent cavitating flows. *Computers & Fluids*, **103**:262–274, 2014. URL http://dx.doi.org/10.1016/j.compfluid.2014.07.026.

[110] S. O. Unverdi and G. Tryggvason: A front-tracking method for viscous, incompressible, multi-fluid flows. *Journal of Computational Physics*, **100**(1):25–37, 1992. URL http://dx.doi.org/10.1016/0021-9991(92)90307-K.

[111] S. Vincent, J. Larocque, D. Lacanette, A. Toutant, P. Lubin, and P. Sagaut: Numerical simulation of phase separation and a priori two-phase LES filtering. *Computers & Fluids*, **37**(7):898–906, 2008. URL http://dx.doi.org/10.1016/J.Compfluid.2007.02.017.

[112] R. Zamansky and F. Ham: *Modelization of cavitation in shear flows*. Annual research briefs, Center for Turbulence Research, 2013. URL https://web.stanford.edu/group/ctr/ResBriefs/2013/04_zamansky.pdf.